SAPIENZA
UNIVERSITÀ DI ROMA

Dynamics and control of robotic systems for on-orbit objects manipulation

Dipartimento di Ingegneria Meccanica e Aerospaziale

Dottorato di Ricerca in Aeronautical and Space Engineering – XXXII Ciclo

Candidate

Angelo Stolfi

ID number 1193396

Thesis Advisor

Prof. Paolo Gasbarri

Co-Advisor

Prof. Fabio Celani

February 27, 2020

Dynamics and control of robotic systems for on-orbit objects manipulation
Ph.D. thesis. Sapienza – University of Rome

This thesis has been typeset by LaTeX and the Sapthesis class.

Author's email: angelo.stolfi@uniroma1.it

Contents

List of Figures

List of Tables

Introduction

Multi-body systems (MSs) are assemblies composed of multiple bodies (either rigid or structurally flexible) connected among each other by means of mechanical joints. In many engineering fields (such as aerospace, aeronautics, robotics, machinery, military weapons and bio-mechanics) a large number of systems (e.g. space robots, aircraft, terrestrial vehicles, industrial machinery, launching systems) can be included in this category. The dynamic characteristics and performance of such complex systems need to be accurately and rapidly analyzed and predicted. Taking this engineering background into consideration, a new branch of study, named as Multi-body Systems Dynamics (MSD), emerged in the 1960s and has become an important research and development area in modern mechanics; it mainly addresses the theoretical modeling, numerical analysis, design optimization and control for complex MSs. The research on dynamics modeling and numerical solving techniques for rigid multi-body systems has relatively matured and perfected through the developments over the past half century. However, for many engineering problems, the rigid multi-body system model cannot meet the requirements in terms of precision. It is then necessary to consider the coupling between the large rigid motions of the MS components and their elastic displacements; thus the study of the dynamics of flexible MSs has gained increasing relevance [1]-[14]. The flexible MSD involves many theories and methods, such as continuum mechanics, computational mechanics and nonlinear dynamics, thus implying a higher requirement on the theoretical basis. Robotic on-orbit operations for servicing, repairing or de-orbiting existing satellites are among space mission concepts expected to have a relevant role in a close future [15]. In particular, many studies have been focused on removing significant debris objects from their orbit [16, 17]. While mission designs involving tethers [18, 19], nets, harpoons or glues are among options studied and analyzed by the scientific and industrial community, the debris removal by means of robotic manipulators seems to be the solution with the longest space experience. In fact, robotic manipulators are now a well-established technology in space applications as they are routinely used for

handling and assembling large space modules and for reducing human extravehicular activities on the International Space Station [20, 21, 22]. The operations are generally performed in a tele-operated approach, where the slow motion of the robotic manipulator is controlled by specialized operators on board of the space station or at the ground control center. Grasped objects are usually cooperative, meaning they are capable to re-orient themselves or have appropriate mechanisms for engagement with the end-effectors of the manipulator (i.e. its terminal parts). On the other hand, debris removal missions would target objects which are often non-controlled and lacking specific hooking points. Moreover, there would be a distinctive advantage in terms of cost and reliability to conduct this type of mission profile in a fully autonomous manner, as issues like obstacle avoidance could be more easily managed locally than from a far away control center. Space Manipulator Systems (SMSs) are satellites made of a base platform equipped with one or more robotic arms. A SMS is a floating system because its base is not fixed to the ground like in terrestrial manipulators; therefore, the motion of the robotic arms affects the attitude and position of the base platform and vice versa. This reciprocal influence is denoted as "dynamic coupling" and makes the dynamics modeling and motion planning of a space robot much more complicated than those of fixed-base manipulators [23]. Indeed, SMSs are complex systems whose dynamics modeling requires appropriate theoretical and mathematical tools. The growing importance SMSs are acquiring is due to their operational ductility as they are able to perform complicated tasks such as repairing, refueling, re-orbiting spacecraft, assembling articulated space structures and cleaning up the increasing amount of space debris [15, 16]. SMSs have also been employed in several rendezvous and docking missions. They have also been the object of many studies which verified the possibility to extend the operational life of commercial and scientific satellites by using an automated servicing spacecraft dedicated to repair, refuel and/or manage their failures (e.g. DARPA's Orbital Express and JAXA's ETS VII). Furthermore, Active Debris Removal (ADR) via robotic systems is one of the main concerns governments and space agencies have been facing in the last years. As a result, the grasping and post-grasping operations on non-cooperative objects are still open research areas facing many technical challenges [15]: the target object identification by means of passive [24] or active [25] optical techniques, the estimation of its kinematic state [26], the design of dexterous robotic manipulators [27, 28] and end-effectors [29, 30], the multi-body dynamics analysis [31], the selection of approaching and grasping maneuvers [32] and the post-grasping mission planning [33, 34] are the main open research challenges in this field.

The missions involving the use of SMSs are usually characterized by the following typical phases:

1. Orbital approach;
2. Rendez-vous;
3. Robotic arm(s) deployment;
4. Pre-grasping;
5. Grasping and post-grasping operations.

This thesis project will focus on the last three. The manuscript is structured as follows: Chapter 1 presents the derivation of a multi-body system dynamics equations further developing them to reach their Kane's formulation; Chapter 2 investigates two different approaches (Particle Swarm Optimization and Machine Learning) dealing with a space manipulator deployment maneuver; Chapter 3 addresses the design of a combined Impedance+PD controller capable of accomplishing the pre-grasping phase goals and Chapter 4 is dedicated to the dynamic modeling of the closed-loop kinematic chain formed by the manipulator and the grasped target object and to the synthesis of a Jacobian Transpose+PD controller for a post-grasping docking maneuver. Finally, the concluding remarks summarize the overall thesis contribution.

Chapter 1

Space Manipulator Systems modeling

The dynamics equations of a SMS and a target object can be obtained by means of a multibody formulation [8]. It is well known that the choice of the parameters that describe the kinematics of a multibody system leads to different sets of dynamics equations. In fact, by using the so called Eulerian approach, the motion of each individual member is described through kinematic parameters: (a) position of its center of mass with respect to an inertial reference frame, (b) attitude variables with respect to an inertial reference frame. It should be noted, however, that the above-described motion parameters are redundant. For this reason, the following must be introduced: (a) reactions between members, (b) equations of compatibility of the same number of reactions. In summary, (i) the set of unknowns is: motion parameters, reactions, control actions, (ii) the equations are those of equilibrium, compatibility and control. Control is introduced by prescribing the motion of some members and enforced by control forces and/or torques (of course, since the target object is non-cooperative, control regards only the SMS). In the Lagrangian approach the selected motion parameters are already consistent with the compatibility conditions. In this case, the expressions of kinetic, potential and elastic energy and the work of non-conservative forces are written and the application of Lagrangian techniques directly provides the solving system. No reactions and compatibility equations appear here; however, for control purposes, prescribed motion laws must again be introduced [35]. In this work the procedure to obtain the governing equations of the SMS and the target object is based on Kane's formulation [36]. Next, the necessary steps to derive the dynamics equations in Kane's form will be shown.

1.1 Dynamics equations as a constrained optimization problem

By indicating with $\boldsymbol{X}$ the vector of state variables and with $\boldsymbol{V}$ the vector containing the time derivatives of the state variables, under the hypothesis of conservative forces, the Lagrangian function

$$L(\boldsymbol{X}, \boldsymbol{V}) = T(\boldsymbol{X}, \boldsymbol{V}) - U(\boldsymbol{X}) \tag{1.1}$$

is defined, where T is the kinetic energy and U is the potential energy from which the forces are derived. Hamilton's Principle, equivalent to that of the Virtual Works, states that in a dynamic system the *action* functional

$$A = \int_{t_0}^{t_\mathrm{f}} L(\boldsymbol{X}, \boldsymbol{V})\, dt \tag{1.2}$$

is minimized. Before addressing this problem, some basic concepts of variational calculus are reviewed in the following.

1.1.1 Minimization of a function

Consider a function of n variables $L(\boldsymbol{X}) = L(x_1, \ldots, x_n)$; its minimum is found by imposing

$$\frac{\partial L}{\partial \boldsymbol{X}} = 0 \tag{1.3}$$

Eq. (1.3) represents a necessary condition.

1.1.2 Minimization of a function subject to a constraint

Consider a function of $n + m$ variables $L(\boldsymbol{X}, \boldsymbol{u}) = L(x_1, \ldots, x_n, u_1, \ldots, u_m)$ (where x_i are the state variables and u_i are those relative to the control) which has to be minimized under the vectorial constraint $\boldsymbol{f}(\boldsymbol{X}, \boldsymbol{u}) = f(x_1, \ldots, x_n, u_1, \ldots, u_m) = \boldsymbol{0}$, that is

$$\begin{aligned}
&\min L(x_1, \ldots, x_n, u_1, \ldots, u_m) \\
&\text{under the constraint:} \\
&f_1(x_1, \ldots, x_n, u_1, \ldots, u_m) = 0 \\
&\vdots \\
&f_q(x_1, \ldots, x_n, u_1, \ldots, u_m) = 0
\end{aligned}$$

To do so, a new function is defined by extending the function which has to be minimized by means of the constraint; this is achieved introducing the vector of the Lagrange multipliers $\boldsymbol{\lambda}$. In other words, the search is for the minimum of the function $H = L + \boldsymbol{\lambda}^{\mathrm{T}} \boldsymbol{f}$ (indeed, if H is minimum, L is minimum as well). In order to find the minimum of H, the following condition needs to be imposed:

$$dH = H_{\boldsymbol{X}} d\boldsymbol{X} + H_{\boldsymbol{u}} d\boldsymbol{u} = 0 \tag{1.4}$$

which leads to the following requirements:

$$H_{\boldsymbol{X}} = \frac{\partial H}{\partial \boldsymbol{X}} = L_{\boldsymbol{X}} + \boldsymbol{\lambda}^{\mathrm{T}} \boldsymbol{f}_{\boldsymbol{X}} = \boldsymbol{0} \tag{1.5}$$

$$H_{\boldsymbol{u}} = \frac{\partial H}{\partial \boldsymbol{u}} = L_{\boldsymbol{u}} + \boldsymbol{\lambda}^{\mathrm{T}} \boldsymbol{f}_{\boldsymbol{u}} = \boldsymbol{0} \tag{1.6}$$

that is:

$$\boldsymbol{\lambda}^{\mathrm{T}} = -L_{\boldsymbol{X}} \boldsymbol{f}_{\boldsymbol{X}}^{+} \tag{1.7}$$

$$L_{\boldsymbol{u}} + \boldsymbol{\lambda}^{\mathrm{T}} \boldsymbol{f}_{\boldsymbol{u}} = \boldsymbol{0} \tag{1.8}$$

Eqs. (1.7) and (1.8) are those for the constrained minimization of a function.

1.1.3 Minimization of a functional subject to a constraint

Hamilton's principle though requires the constrained minimization not of a function, but of a functional instead in that the Lagrangian function is a function of functions. In this case the constraint can be represented either by the actual presence of joints or by the fact that kinematic relations hold. In fact, if Lagrangian variables (which by definition are already compatible with the physical constraints) are chosen as the mechanical system state variables, the relation which states that the velocity is the time derivative of the position needs to be satisfied.

On account of this, for a system that is not physically constrained or constrained but described by means of the Lagrangian variables, since the Lagrangian function depends upon position $\boldsymbol{X}$ and velocity $\boldsymbol{V}$ ($L = L(x_1, \ldots, x_n, v_1, \ldots, v_n)$), the constraint relation $\dot{\boldsymbol{X}} = \boldsymbol{V}$ has to hold.

In general, the proposed problem can be declined as a constrained optimization problem where the functional to be minimized (the action functional) can be expressed as

$$A = \int_{t_0}^{t_{\mathrm{f}}} L(\boldsymbol{X}(t), \boldsymbol{V}(t), t)\, dt \tag{1.9}$$

under the dynamic constraint

$$\dot{\boldsymbol{X}}(t) = \boldsymbol{f}(\boldsymbol{X}(t), \boldsymbol{V}(t), t) \tag{1.10}$$

To include the constraint in the minimization problem, a functional augmented by the constraint is introduced; this is done by means of a vector of Lagrangian multipliers $\boldsymbol{\lambda}(t)$:

$$\bar{A} = \int_{t_0}^{t_\mathrm{f}} \{L(\boldsymbol{X}(t), \boldsymbol{V}(t), t) + \boldsymbol{\lambda}^\mathrm{T}(t)[\boldsymbol{f}(\boldsymbol{X}(t), \boldsymbol{V}(t), t) - \dot{\boldsymbol{X}}(t)]\}\, dt \tag{1.11}$$

Defining the Hamiltonian functional as

$$H(\boldsymbol{X}(t), \boldsymbol{V}(t), \boldsymbol{\lambda}(t), t) = L(\boldsymbol{X}(t), \boldsymbol{V}(t), t) + \boldsymbol{\lambda}^\mathrm{T}(t)\boldsymbol{f}(\boldsymbol{X}(t), \boldsymbol{V}(t), t) \tag{1.12}$$

the action functional can be written as

$$\bar{A} = \int_{t_0}^{t_\mathrm{f}} [H(\boldsymbol{X}(t), \boldsymbol{V}(t), \boldsymbol{\lambda}(t), t) - \boldsymbol{\lambda}^\mathrm{T}(t)\dot{\boldsymbol{X}}(t)]\, dt \tag{1.13}$$

Integrating by parts results in the following:

$$\bar{A} = -\boldsymbol{\lambda}^\mathrm{T}(t_\mathrm{f})\boldsymbol{X}_\mathrm{f} + \boldsymbol{\lambda}^\mathrm{T}(t_0)\boldsymbol{X}_0 + \int_{t_0}^{t_\mathrm{f}} [H(\boldsymbol{X}(t), \boldsymbol{V}(t), \boldsymbol{\lambda}(t), t) + \dot{\boldsymbol{\lambda}}^\mathrm{T}(t)\boldsymbol{X}(t)]\, dt \tag{1.14}$$

In order to solve the optimization problem, the differential of $\bar{A}$ has to be null; the latter is given by the sum of two contributions:

$$\delta\bar{A} = \int_{t_0}^{t_\mathrm{f}} \left[\frac{\partial(H(\boldsymbol{X}(t), \boldsymbol{V}(t), \boldsymbol{\lambda}(t), t) + \dot{\boldsymbol{\lambda}}^\mathrm{T}(t)\boldsymbol{X}(t))}{\partial \boldsymbol{X}}\, d\boldsymbol{X} + \frac{\partial(H(\boldsymbol{X}(t), \boldsymbol{V}(t), \boldsymbol{\lambda}(t), t) + \dot{\boldsymbol{\lambda}}^\mathrm{T}(t)\boldsymbol{X}(t))}{\partial \boldsymbol{V}}\, d\boldsymbol{V} \right] dt \tag{1.15}$$

For the first term:

$$\frac{\partial[H(\boldsymbol{X}(t), \boldsymbol{V}(t), \boldsymbol{\lambda}(t), t) + \dot{\boldsymbol{\lambda}}^\mathrm{T}(t)\boldsymbol{X}(t)]}{\partial \boldsymbol{X}} = \begin{bmatrix} \frac{\partial H}{\partial x_1} + \dot{\lambda}_1 \\ \vdots \\ \frac{\partial H}{\partial x_n} + \dot{\lambda}_n \end{bmatrix}^\mathrm{T} =$$

$$= \begin{bmatrix} \frac{\partial L}{\partial x_1} + \lambda_1 \frac{\partial f_1}{\partial x_1} + \lambda_2 \frac{\partial f_2}{\partial x_1} + \cdots + \lambda_n \frac{\partial f_n}{\partial x_1} + \dot{\lambda}_1 \\ \vdots \\ \frac{\partial L}{\partial x_n} + \lambda_1 \frac{\partial f_1}{\partial x_n} + \lambda_2 \frac{\partial f_2}{\partial x_n} + \cdots + \lambda_n \frac{\partial f_n}{\partial x_n} + \dot{\lambda}_n \end{bmatrix}^\mathrm{T} = \left[\left(\frac{\partial L}{\partial \boldsymbol{X}}\right)^\mathrm{T} + \left(\frac{\partial f}{\partial \boldsymbol{X}}\right)^\mathrm{T} \boldsymbol{\lambda} + \dot{\boldsymbol{\lambda}} \right]^\mathrm{T} \tag{1.16}$$

For the second term:

$$\frac{\partial[H(\boldsymbol{X}(t),\boldsymbol{V}(t),\boldsymbol{\lambda}(t),t)+\dot{\boldsymbol{\lambda}}^{\mathrm{T}}(t)\boldsymbol{X}(t)]}{\partial \boldsymbol{V}}=\begin{bmatrix}\frac{\partial H}{\partial v_1}\\ \vdots \\ \frac{\partial H}{\partial v_n}\end{bmatrix}^{\mathrm{T}}= \\ =\begin{bmatrix}\frac{\partial L}{\partial v_1}+\lambda_1\frac{\partial f_1}{\partial v_1}+\lambda_2\frac{\partial f_2}{\partial v_1}+\cdots+\lambda_n\frac{\partial f_n}{\partial v_1}\\ \vdots \\ \frac{\partial L}{\partial v_n}+\lambda_1\frac{\partial f_1}{\partial v_n}+\lambda_2\frac{\partial f_2}{\partial v_n}+\cdots+\lambda_n\frac{\partial f_n}{\partial v_n}\end{bmatrix}^{\mathrm{T}}=\left[\Big(\frac{\partial L}{\partial \boldsymbol{V}}\Big)^{\mathrm{T}}+\Big(\frac{\partial f}{\partial \boldsymbol{V}}\Big)^{\mathrm{T}}\boldsymbol{\lambda}\right]^{\mathrm{T}} \tag{1.17}$$

The two conditions to be imposed in order to null the differential are then

$$\dot{\boldsymbol{\lambda}}=-\Big(\frac{\partial L}{\partial \boldsymbol{X}}\Big)^{\mathrm{T}}-\Big(\frac{\partial f}{\partial \boldsymbol{X}}\Big)^{\mathrm{T}}\boldsymbol{\lambda} \tag{1.18}$$

$$\Big(\frac{\partial L}{\partial \boldsymbol{V}}\Big)^{\mathrm{T}}+\Big(\frac{\partial f}{\partial \boldsymbol{V}}\Big)^{\mathrm{T}}\boldsymbol{\lambda}=\mathbf{0} \tag{1.19}$$

In the case of a dynamic system defined by means of Lagrangian variables, the constraint is given by $\boldsymbol{f}=\boldsymbol{V}$. Since $\partial \boldsymbol{f}/\partial \boldsymbol{V}=\mathbf{I}$ (where $\mathbf{I}$ is an $n\times n$ identity matrix), using Eq. (1.19) the following is obtained:

$$\boldsymbol{\lambda}=-\Big(\frac{\partial L}{\partial \boldsymbol{V}}\Big)^{\mathrm{T}} \tag{1.20}$$

Consequently, deriving with respect to time leads to

$$\dot{\boldsymbol{\lambda}}=-\frac{d}{dt}\Big(\frac{\partial L}{\partial \boldsymbol{V}}\Big)^{\mathrm{T}}=-\left[\frac{d}{dt}\Big(\frac{\partial L}{\partial \boldsymbol{V}}\Big)\right]^{\mathrm{T}} \tag{1.21}$$

Substituting Eq. (1.21) into Eq. (1.18), one obtains

$$\dot{\boldsymbol{\lambda}}=-\Big(\frac{\partial L}{\partial \boldsymbol{X}}\Big)^{\mathrm{T}}-\Big(\frac{\partial f}{\partial \boldsymbol{X}}\Big)^{\mathrm{T}}\boldsymbol{\lambda}=-\left[\frac{d}{dt}\Big(\frac{\partial L}{\partial \boldsymbol{V}}\Big)\right]^{\mathrm{T}} \tag{1.22}$$

But since $\frac{\partial \boldsymbol{f}}{\partial \boldsymbol{X}}=\frac{\partial \boldsymbol{V}}{\partial \boldsymbol{X}}=\mathbf{0}$, Eq. (1.22) becomes

$$\left[\frac{d}{dt}\Big(\frac{\partial L}{\partial \boldsymbol{V}}\Big)\right]^{\mathrm{T}}-\Big(\frac{\partial L}{\partial \boldsymbol{X}}\Big)^{\mathrm{T}}=\mathbf{0}\quad\rightarrow\quad\frac{d}{dt}\Big(\frac{\partial L}{\partial \boldsymbol{V}}\Big)-\frac{\partial L}{\partial \boldsymbol{X}}=\mathbf{0} \tag{1.23}$$

which are the Euler-Lagrange equations (notice that, in the case of presence of non-conservative forces, there would be a non-null term on the right hand side of Eq. (1.23) which would be the projection of these forces on the dynamics equations).

Performing the derivatives, one arrives at a form of the dynamics equations which is

$$\mathbf{M}\ddot{\boldsymbol{X}} = \boldsymbol{C}(\boldsymbol{X}, \dot{\boldsymbol{X}}) + \boldsymbol{F} \tag{1.24}$$

where $\mathbf{M}$ is the generalized mass matrix, $\boldsymbol{C}$ is the non-linear terms vector and $\boldsymbol{F}$ is the vector of external forces and moments projected on the dynamics equations.

1.1.4 Minimization of the action functional under physical constraints

The case where $\boldsymbol{X}$ is not a set of Lagrangian variables is now considered. It will be necessary to add, besides the kinematic constraint, also the physical constraints that are present. Constraints are classified in the following way:

- *Holonomic*: they can be reduced in a finite form, i.e. the constraint equation can be written in terms of positions and/or rotations)

    1. *Rheonomic*: there is an explicit dependency on time of the constraint algebraic equations, i.e.
    $$\boldsymbol{\Psi}(\boldsymbol{X}, t) = \mathbf{0} \tag{1.25}$$

    2. *Scleronomic*: there is not an explicit dependency on time of the constraint algebraic equations, i.e.
    $$\boldsymbol{\Psi}(\boldsymbol{X}) = \mathbf{0} \tag{1.26}$$

- *Non-Holonomic*: they cannot be reduced in a finite form, but only in differential form, i.e.
$$\boldsymbol{\Psi}(\boldsymbol{X}, \dot{\boldsymbol{X}}, t) = \mathbf{0} \tag{1.27}$$

In the case of scleronomic constraints, the problem can be formulated as follows:

$$\min A = \int_{t_0}^{t_f} L \, dt \tag{1.28}$$

under the constraints

$$\dot{\boldsymbol{X}} = \boldsymbol{V} \tag{1.29}$$

$$\boldsymbol{\Psi}(\boldsymbol{X}) = \mathbf{0} \tag{1.30}$$

One has then to define a functional augmented by the differential constraint and the algebraic constraint:

$$H = L + \boldsymbol{\lambda}_1^{\mathrm{T}} \boldsymbol{V} + \boldsymbol{\lambda}_2{}^{\mathrm{T}} \boldsymbol{\Psi} \tag{1.31}$$

The conditions to be imposed are

$$\frac{\partial H}{\partial \boldsymbol{V}} = \mathbf{0} \quad \rightarrow \quad \Big(\frac{\partial L}{\partial \boldsymbol{V}}\Big)^{\mathrm{T}} + \Big(\frac{\partial \boldsymbol{V}}{\partial \boldsymbol{V}}\Big)\boldsymbol{\lambda}_1 + \Big(\frac{\partial \boldsymbol{\Psi}}{\partial \boldsymbol{V}}\Big)^{\mathrm{T}} \boldsymbol{\lambda}_2 = \Big(\frac{\partial L}{\partial \boldsymbol{V}}\Big)^{\mathrm{T}} + \boldsymbol{\lambda}_1 = \mathbf{0} \tag{1.32}$$

$$\dot{\boldsymbol{\lambda}}_1 = -\Big(\frac{\partial L}{\partial \boldsymbol{X}}\Big)^{\mathrm{T}} - \Big(\frac{\partial \boldsymbol{V}}{\partial \boldsymbol{X}}\Big)^{\mathrm{T}} \boldsymbol{\lambda}_1 - \Big(\frac{\partial \boldsymbol{\Psi}}{\partial \boldsymbol{X}}\Big)^{\mathrm{T}} \boldsymbol{\lambda}_2 = -\frac{\partial L}{\partial \boldsymbol{X}} - \boldsymbol{\Psi}_{\boldsymbol{X}}{}^{\mathrm{T}} \boldsymbol{\lambda}_2 \tag{1.33}$$

Deriving Eq. (1.32) one gets

$$\dot{\boldsymbol{\lambda}}_1 = -\left[\frac{d}{dt}\frac{\partial L}{\partial \boldsymbol{V}}\right]^{\mathrm{T}} \tag{1.34}$$

which substituted into Eq. (1.33) leads to

$$\left[\frac{d}{dt}\frac{\partial L}{\partial \boldsymbol{V}}\right]^{\mathrm{T}} - \Big(\frac{\partial L}{\partial \boldsymbol{X}}\Big)^{\mathrm{T}} - \boldsymbol{\Psi}_{\boldsymbol{X}}^{\mathrm{T}} \boldsymbol{\lambda}_2 = \mathbf{0} \tag{1.35}$$

Eq. (1.35) represents Euler-Lagrange equations in the case where the used variables are not Lagrangian variables which makes the explicit introduction of the physical constraints necessary (analogous considerations to the ones made for Eq. (1.23) hold in the case of presence of non-conservative forces here as well). Performing the derivatives one obtains

$$\mathbf{M}\ddot{\boldsymbol{X}} + \boldsymbol{\Psi}_{\boldsymbol{X}}^{\mathrm{T}} \boldsymbol{\lambda} = \boldsymbol{C}(\boldsymbol{X}, \dot{\boldsymbol{X}}) + \boldsymbol{F} \tag{1.36}$$

The term $\boldsymbol{\Psi}_{\boldsymbol{X}}^{\mathrm{T}} \boldsymbol{\lambda}$ represents the constraints reactions projected on the dynamics equations.

1.2 Kane's approach for obtaining the dynamics equations

Now the equations of motion will be obtained using a Kane-like formulation that permits to model spacecraft systems with a minimum set of equations reducing the computational costs with respect to a classic Eulerian approach. Starting from the Eulerian formulation (which allows a simple definition of bodies equations of motion), the model is reduced to a system of a minimum set of variables and equations (similar

to one obtained via a Lagrangian approach) through the Jacobian operator which takes the compatibility conditions between the bodies into account. This approach has the following advantages:

- The system is constituted by Ordinary Differential Equations (ODEs) instead of Differential Algebraic Equations (DAEs) (the latter are obtained using the Eulerian approach);
- The kinematics are compatible with the physical constraints; this implies that there is no problem with the choice of consistent initial conditions which instead is an aspect to be taken into account when using the Eulerian approach;
- It is good for the implementation of the manipulator controller since it provides straightforward information on the control actions actually required from the SMS actuators (in order to obtain the same kind of data using the Eulerian approach, additional calculations need to be done).

The convenience of using this approach appears evident as the system becomes more and more articulated (i.e. with an increasing number of arms and links forming the arms and the presence of more complex joints).

The procedure to obtain the dynamics equations in Kane's form is illustrated in the following. In first place, one defines the state vector $\boldsymbol{X}$ which contains the variables that describe the kinematic state of each body (just like in the Eulerian approach). All the variables are defined with respect to an inertial reference frame. In second place, one then defines the vector of minimal (Lagrangian) variables $\boldsymbol{Q}$. The two vectors (or, more precisely, their time derivatives) are related through the Jacobian matrix $\mathbf{J}$:

$$\dot{\boldsymbol{X}} = \mathbf{J}\dot{\boldsymbol{Q}} \tag{1.37}$$

The dynamics equations are written for the system of bodies taking into account the constraints reactions:

$$\mathbf{M}\ddot{\boldsymbol{X}} + \boldsymbol{\Psi}_{\boldsymbol{X}}^{\mathrm{T}}\boldsymbol{\lambda} = \boldsymbol{C}(\boldsymbol{X}, \dot{\boldsymbol{X}}) + \boldsymbol{F} \tag{1.38}$$

to which the constraints equations have to be added:

$$\boldsymbol{\Psi} = \mathbf{0} \tag{1.39}$$

Eq. (1.39) is derived with respect to time:

$$\boldsymbol{\Psi}_{\boldsymbol{X}}\dot{\boldsymbol{X}} = \mathbf{0} \tag{1.40}$$

Using Eq. (1.37), one has:

$$\boldsymbol{\Psi}_{\boldsymbol{X}}\mathbf{J}\dot{\boldsymbol{Q}} = \mathbf{0} \tag{1.41}$$

Since the trivial case where $\dot{\boldsymbol{Q}} = \mathbf{0}$ (which means that the system remains stationary at its initial conditions) is not considered, Eq. (1.41) leads to

$$\boldsymbol{\Psi}_{\boldsymbol{X}}\mathbf{J} = \mathbf{0} \tag{1.42}$$

Eq. (1.42) implies that $\mathbf{J}$ is the null space of $\boldsymbol{\Psi}_{\boldsymbol{X}}$. Pre-multiplying by $\mathbf{J}^{\mathrm{T}}$ and taking into account Eq. (1.37), the dynamics equations can be written as

$$\mathbf{J}^{\mathrm{T}}\mathbf{M}\mathbf{J}\ddot{\boldsymbol{Q}} + \mathbf{J}^{\mathrm{T}}\mathbf{M}\dot{\mathbf{J}}\dot{\boldsymbol{Q}} + \mathbf{J}^{\mathrm{T}}\boldsymbol{\Psi}_{\boldsymbol{X}}^{\mathrm{T}}\boldsymbol{\lambda} = \mathbf{J}^{\mathrm{T}}\boldsymbol{C} + \mathbf{J}^{\mathrm{T}}\boldsymbol{F} \tag{1.43}$$

But since $\boldsymbol{\Psi}_{\boldsymbol{X}}\mathbf{J} = \mathbf{0}$, $\mathbf{J}^{\mathrm{T}}\boldsymbol{\Psi}_{\boldsymbol{X}}^{\mathrm{T}} = \mathbf{0}$ also holds and the dynamics equations in terms of minimal variables are obtained:

$$\mathbf{J}^{\mathrm{T}}\mathbf{M}\mathbf{J}\ddot{\boldsymbol{Q}} + \mathbf{J}^{\mathrm{T}}\mathbf{M}\dot{\mathbf{J}}\dot{\boldsymbol{Q}} = \mathbf{J}^{\mathrm{T}}\boldsymbol{C} + \mathbf{J}^{\mathrm{T}}\boldsymbol{F} \tag{1.44}$$

Chapter 2

Deployment maneuver of a robotic Space Manipulator System

The extremely high number of objects orbiting the Earth calls for solutions to keep free operational space for telecommunication systems in geo-synchronized orbit as well as to prevent the endangering of space systems in Low-Earth orbit [16]. Future on-orbit servicing missions will entail many challenges such as the capture of nonfunctional satellites, spent spacecraft or last stages of rockets [15, 37]. Some of them are related to accurate position and attitude control in autonomous tracking and rendezvous operations between the chaser and target satellites. Within this framework, a crucial phase for mission success is the deployment of the robotic equipment mounted on the chaser base platform. As a matter of fact, this equipment is placed in its stowed configuration during launch and needs to be deployed once in orbit in order to reach the target of interest. Nevertheless, the achievement of this goal poses a few issues to be addressed: differently from on-ground operations where both the target and the base of the manipulator are constrained, the on-orbit environment requires an ad-hoc approach due to the fact in this case they are floating instead.

2.1 Particle Swarm Optimization applied to arm deployment maneuver

As stated, the deployment phase consists in the task of bringing the robotic arm(s) from its initial (stowed) configuration to the appropriate final conditions which are compatible with successive grasping operations of a target object to be captured. In the context of deployment maneuvers, the issue of choosing an optimal strategy is certainly relevant given the limited amount of resources available on board of space systems and the strict operational requirements and constraints often characterizing space activities. Consequently, the choice of such optimality criteria should take into consideration aspects such as propellant consumption, maneuver time duration, disturbances induced on the base platform, mechanical limits concerning the manipulator components and mission requirements on the end-effector kinematic state. Indeed, the problem can be stated as being a Multi-Objective (MO) Constrained Optimization problem [38, 39].

Different algorithms have been developed to tackle optimization problems on a general basis [40]. Population-based optimization techniques such as Genetic Algorithms (GAs) [41], Particle Swarm Optimization (PSO) [42], Differential Evolution (DE) [43]-[45] and Ant Colony Optimization (ACO) [46] have been popular choices for solving MO problems. Research shows that the PSO algorithm offers some advantages over GAs being simpler and less expensive from the computational cost standpoint [47, 48]. Given the positive results obtained by using PSO in single-objective optimization applications, this technique has been extended to MO problems as well. A review of strategies which adopt the PSO algorithm within the MO context can be found in [49]. Nevertheless, the majority of the reported approaches are constraint-free. Since the nature of the problem being here analyzed is indeed characterized by the presence of significant constraint conditions, the methodology developed by L. D Li et Al. in [50] is embraced and properly adapted to the case under examination.

The deployment maneuver is studied by means of an in-house developed Matlab code which allows for an easy parameterization with respect to the sensitive variables in the system dynamics and optimization procedure. Three-dimensional dynamics will be considered.

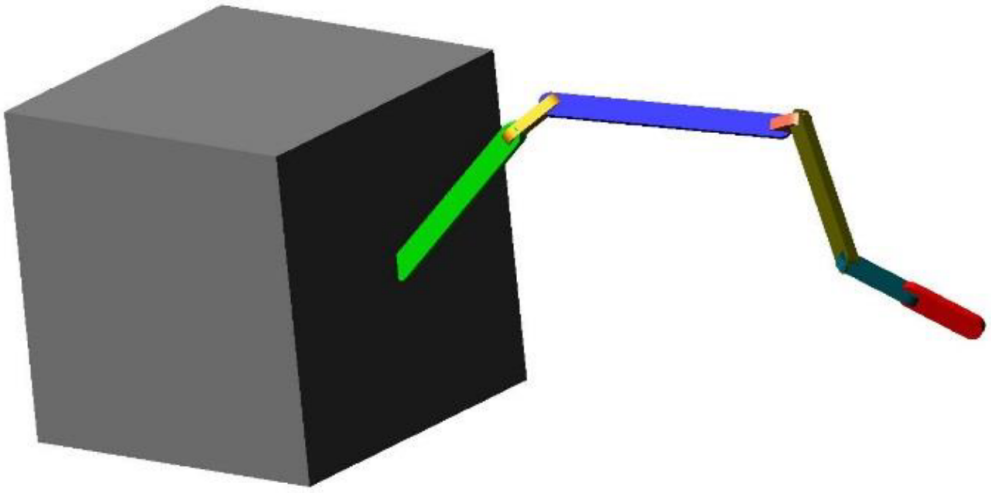

Figure 2.1. Schematic of the multi-body space manipulator.

2.1.1 Single-arm multi-body space manipulator

In Fig.2.1 the schematic of the one-arm space manipulator is reported. The first link of the robotic arm is connected to the base platform by means of a revolute joint and the links are connected with each other by revolute joints as well with axes oriented at 90° with respect to the previous one. The end-effector (which can be identified with the last link) is connected to the rest of the arm by means of a translational joint. The arm has a total of $n_l = 7$ links. The position of the attaching point of the arm on the SMS base (referred to as the shoulder) has been fixed at the geometrical center of its right-side face. The bus of the SMS has a cubic shape

Table 2.1. Properties of the links of the space manipulator.

Link	Mass kg	Length m	Width m	Depth m
1	20	1	0.1	0.05
2	5	0.2	0.1	0.05
3	20	1	0.1	0.05
4	5	0.2	0.1	0.05
5	20	1	0.1	0.05
6	5	0.3	0.1	0.05
7	5	0.3	0.1	0.05

of length 1.5 m, its mass is $m_B = 500$ kg. The main properties of the arm links are reported in Tab. 2.1. For what concerns the control capabilities of the SMS, the base platform is equipped with a set of three thrusters and three control moment

Table 2.2. Maximum control actions that can be supplied by the SMS actuators.

Actuator	Maximum value of supplied control action
Base thrusters	50 N
Base ACS	50 N m
Revolute joints motors	30 N m
Linear actuator	50 N

gyros placed along the base principal body axes; furthermore, each revolute joint and the translational joint can be actuated by means of an electric motor and a linear actuator respectively. The maximum control actions which can be supplied by the latter are listed in Tab. 2.2.

2.1.2 Algorithm description

Most real-world search and optimization problems involve multiple objectives (MO) that need to be achieved simultaneously. The presence of constraints adds difficulties to the already challenging task of finding optimal solutions to the problem under consideration. All solutions to a multi-objective optimization problem are called Pareto-optimal solutions and the curve obtained by joining these solutions is known as a Pareto-optimal front. In solving MO problems, three goals need to be achieved [51]:

1. Find a set of solutions as close as possible to the true Pareto-optimal front;
2. Find a set of solutions as diverse as possible;
3. Find a set of solutions as many as possible.

The objective is to find optimal solutions for the problem concerning the deployment of the SMS robotic arm in order to reach a moving target point. The adopted methodology for tackling this issue is that of Particle Swarm Optimization (PSO) properly modified to take into account both the multi-objective nature of the problem and the presence and the presence of operational constraints as well [50].

To begin with, a general multi-objective constrained optimization problem involves a vector of variables to be optimized (the "decision vector") $\boldsymbol{x} = [x_1, x_2, \ldots, x_n]$, an objective function vector $\boldsymbol{f}(\boldsymbol{x}) = [f_1(\boldsymbol{x}), f_2(\boldsymbol{x}), \ldots, f_k(\boldsymbol{x})]$ and a constraint function vector $\boldsymbol{g}(\boldsymbol{x}) = [g_1(\boldsymbol{x}), g_2(\boldsymbol{x}), \ldots, g_m(\boldsymbol{x})]$. The problem can be stated as finding

$\boldsymbol{x}^*$ which

$$\text{minimize} \quad f_j(\boldsymbol{x}), \quad j = 1, 2, \ldots, k, \quad \text{subject to} \quad g_i(\boldsymbol{x}) \leq 0, \quad i = 1, 2, \ldots, m$$

where k is the total number of objective functions and m is the total number of constraints. In searching for the optimal solutions of the problem, the particles (i.e. the members of the swarm) define trajectories in the parameter space (i.e. iteratively update their positions) based on the following relations:

$$\boldsymbol{v}_i^{(t+1)} = w\boldsymbol{v}_i^{(t)} + c_1 r_1^{(t)}(\boldsymbol{pBest}_i^{(t)} - \boldsymbol{x}_i^{(t)}) + c_2 r_2^{(t)}(\boldsymbol{lBest}^{(t)} - \boldsymbol{x}_i^{(t)}) \tag{2.1}$$

$$\boldsymbol{x}_i^{(t+1)} = \boldsymbol{x}_i^{(t)} + \boldsymbol{v}_i^{(t+1)} \tag{2.2}$$

where $\boldsymbol{x}_i$ is the i-th decision vector (i.e. the i-th particle in the swarm population) in a D-dimensional search space; $\boldsymbol{pBest}_i$ is the best previous position of the i-th particle in the flight history; $\boldsymbol{lBest}$ is the best particle of the swarm (a global PSO is here implemented); $\boldsymbol{v}_i$ denotes the i-th particle velocity; c_1 and c_2 are cognitive and social parameters respectively; w is the inertia weight; r_1 and r_2 are two random numbers uniformly distributed in the range $[0, 1]$; t denotes the iteration. The velocity vectors govern the way particles move across the search space and are made of the contribution of three terms (see right side of Eq. (2.1)); the first one, defined as the *inertia* or *momentum*, prevents the particle from drastically changing direction by keeping track of the previous flow direction; the second term, called *cognitive component*, accounts for the tendency of particles to return to their own previously found best positions; the last one, named the *social component*, identifies the propensity of a particle to move towards the best position of the whole swarm. The selection criteria for $\boldsymbol{pBest}_i^{(t)}$ and $\boldsymbol{lBest}^{(t)}$ can be found in [50]. Nevertheless, it is important to highlight these criteria are responsible for involving the minimization and constraint evaluation features typical of such algorithm.

Before defining the f and g vectors for the problem under examination, it is necessary to point out the adopted control strategy; for what concerns the joint torques and the prismatic joint force, they consist of step-constant control [32]: the n_{c_l} intervals into which the mission duration is divided correspond to n_{c_l} levels of each required control action. Given the number of actuation degrees described above, there will be $n_l n_{c_l}$ step values. The sequence of steps is applied in open-loop to the system. Regarding the base platform control, a closed-loop strategy is adopted instead. More in detail, the base is controlled so that its center of mass moves along

a desired orbit and its attitude tracks a set behavior (these will be more precisely defined in the following). The selected regulator for the implementation of such a strategy is a Proportional-Derivative (PD) Control in which the translational and rotational control are characterized by different gains (namely, two for the translational part and two for the rotational one; further details will be given in the following).

Defining

$$\boldsymbol{u}_i = \left[\bar{u}_{i,1}, \ldots, \bar{u}_{i,n_{c_l}}\right]^{\mathrm{T}}, \qquad i = 1, \ldots, n_l$$

as the vector of the i-th joint control sequence and $K_{p_{T_B}}$, $K_{d_{T_B}}$, $K_{p_{R_B}}$, $K_{d_{R_B}}$ as the base PD Control gains, the vector of variables to be optimized is the following:

$$\boldsymbol{x} = \left[\boldsymbol{u}_1^T, \ldots, \boldsymbol{u}_{n_l}^T, K_{p_{T_B}}, K_{d_{T_B}}, K_{p_{R_B}}, K_{d_{R_B}}, t_f\right]^{\mathrm{T}} \tag{2.3}$$

where t_f is the deployment maneuver time duration.

The next step is to define the objective functions vector. The chosen criteria concern the maneuver time duration, the effort demanded from the control system in terms of supplied actions from the actuators and deviation of the base behavior from the desired one. These considerations lead to the following form of the $\boldsymbol{f}(\boldsymbol{x})$ vector:

$$\boldsymbol{f}(\boldsymbol{x}) = \begin{bmatrix} t_f \\ \frac{1}{t_f}\int_0^{t_f}\left(\sum_{i=1}^{n_l}|u_i| + |{}^B\boldsymbol{u}_{T_B}| + |{}^B\boldsymbol{u}_{R_B}|\right)dt \\ max(|{}^I_{O_I}\boldsymbol{r}_{O_B} - {}^I_{O_I}\boldsymbol{r}^{\mathrm{des}}_{O_B}|) \\ max(|{}^I\boldsymbol{a}_B - {}^I\boldsymbol{a}^{\mathrm{des}}_B|) \end{bmatrix} \tag{2.4}$$

The second row of Eq. (2.4) contains the mean value of the control actions supplied by the SMS actuators; the third and fourth rows respectively represent the maximum deviation of the base center of mass position, defined by vector ${}^I_{O_I}\boldsymbol{r}_{O_B}$, and base attitude, defined by ${}^I\boldsymbol{a}_B$, from their desired values, namely ${}^I_{O_I}\boldsymbol{r}^{\mathrm{des}}_{O_B}$ and ${}^I\boldsymbol{a}^{\mathrm{des}}_B$ respectively. It should be noted the base attitude is expressed in terms of 321 body-fixed Euler angles. All these quantities need to be minimized.

Nevertheless, the optimization procedure which leads to the minimization of the elements in $\boldsymbol{f}$ has to satisfy a certain number of constraint conditions which can result from operational requirements, limitations on the actuators suppliable control actions and user-defined constraints. On account of these, the $\boldsymbol{g}(\boldsymbol{x})$ vector is chosen

as:

$$\boldsymbol{g}(\boldsymbol{x}) = \begin{bmatrix} |u_i| - u_{J_{\max}}, \quad i = 1, \ldots, n_l - 1 \\ |u_{n_l}| - u_{P_{\max}} \\ |{}^B u_{T_{B_i}}| - u_{T_{B_{\max}}}, \quad i = 1, 2, 3 \\ |{}^B u_{R_{B_i}}| - u_{R_{B\max}}, \quad i = 1, 2, 3 \\ |{}^I_{O_I}\boldsymbol{r}_{EE}(t_f) - {}^I_{O_I}\boldsymbol{r}^{\text{des}}_{EE}(t_f)| - \varepsilon_{\text{tol}} \\ |{}^I_{O_I}\dot{\boldsymbol{r}}_{EE}(t_f) - {}^I_{O_I}\dot{\boldsymbol{r}}^{\text{des}}_{EE}(t_f)| - \dot{\varepsilon}_{\text{tol}} \\ |q_P| - q_{P_{\max}} \\ t_f - t_{\lim} \end{bmatrix} \tag{2.5}$$

The first four rows respectively contain conditions on the maximum actions which can be supplied by the joint motors, the linear actuator, the base thrusters and ACS; the fifth and sixth rows respectively provide tolerance relations regarding the end-effector final position and velocity (ε_{tol} and $\dot{\varepsilon}_{\text{tol}}$ are indeed user-definable tolerances); the seventh row represents a condition on the maximum allowable linear joint displacement and the last row indicates a limitation on the deployment maneuver time duration.

A detailed description of the examined case study will be given in the next section.

2.1.3 Numerical results

Case study description

As initial conditions, the SMS base platform has its center of mass moving on an equatorial circular orbit of radius $R_o = 7 \times 10^3$ km, with its body axes aligned with the inertial axes and with zero angular velocity with respect to the inertial reference frame. The arm is in its stowed configuration and the joint rates are null. Furthermore, the translational degree of freedom characterizing the telescopic end-effector is mostly exploited during the last phase of the deployment maneuver when the close proximity approach takes place. Nevertheless, the present study main focus is on the deployment phase preceding the latter; indeed, in the results reported in the following, the linear degree of freedom is blocked and the relevant contributions in the previously defined objective and constraint functions are consequently removed.

SMS base platform PD Control and end-effector desired trajectory

As anticipated above, the SMS base platform is controlled by means of a PD Control for what concerns both translational and rotational motion. The control

law is given by:

$$\begin{aligned}
\boldsymbol{u}_{B_T} &= -K_{P_{B_T}}\left({}^{I}_{O_I}\boldsymbol{r}_{O_B} - {}^{I}_{O_I}\boldsymbol{r}^{\text{des}}_{O_B}\right) - K_{D_{B_T}}\left({}^{I}_{O_I}\dot{\boldsymbol{r}}_{O_B} - {}^{I}_{O_I}\dot{\boldsymbol{r}}^{\text{des}}_{O_B}\right) \\
\boldsymbol{u}_{B_R} &= -K_{P_{B_R}}\left({}^{I}\boldsymbol{a}_B - {}^{I}\boldsymbol{a}^{\text{des}}_B\right) - K_{D_{B_R}}\left({}^{I}_{I}\boldsymbol{\omega}_B - {}^{I}_{I}\boldsymbol{\omega}^{\text{des}}_B\right) \\
\boldsymbol{u}_B &= \begin{bmatrix} \boldsymbol{u}_{B_T} \\ \boldsymbol{u}_{B_R} \end{bmatrix}
\end{aligned} \tag{2.6}$$

For what concerns the desired values appearing in Eq. (2.6), the goal is to maintain the base c.m. on its initial orbit and to make the base rotate synchronously to the orbital motion. This translates into the following:

$$\begin{aligned}
{}^{I}_{O_I}x^{\text{des}}_{O_B} &= R_o\cos\left(\Omega_o t\right) \\
{}^{I}_{O_I}y^{\text{des}}_{O_B} &= 0 \\
{}^{I}_{O_I}z^{\text{des}}_{O_B} &= -R_o\sin\left(\Omega_o t\right) \\
{}^{I}_{O_I}\dot{x}^{\text{des}}_{O_B} &= -\Omega_o R_o\sin\left(\Omega_o t\right) \\
{}^{I}_{O_I}\dot{y}^{\text{des}}_{O_B} &= 0 \\
{}^{I}_{O_I}\dot{z}^{\text{des}}_{O_B} &= -\Omega_o R_o\cos\left(\Omega_o t\right) \\
{}^{I}\psi^{\text{des}}_B &= 0 \\
{}^{I}\theta^{\text{des}}_B &= \Omega_o t \\
{}^{I}\varphi^{\text{des}}_B &= 0 \\
{}^{I}_{I}\omega^{\text{des}}_{x_B} &= 0 \\
{}^{I}_{I}\omega^{\text{des}}_{y_B} &= \Omega_o \\
{}^{I}_{I}\omega^{\text{des}}_{z_B} &= 0
\end{aligned}$$

where $\Omega_o = \sqrt{\mu_E/R_o^3}$ is the orbital angular velocity being μ_E the Earth gravitational parameter.

The SMS dynamics equation takes the following form:

$$\mathbf{J}^T\mathbf{M}\mathbf{J}\ddot{\boldsymbol{Q}} = \mathbf{J}^T\boldsymbol{C} + \mathbf{J}^T\boldsymbol{F} - \mathbf{J}^T\mathbf{M}\dot{\mathbf{J}}\dot{\boldsymbol{Q}} + \boldsymbol{u} \tag{2.7}$$

Vector $\boldsymbol{u}_B$ occupies the first six rows of vector $\boldsymbol{u}$ while the joint torques fill in the remaining positions.

Shifting to the end-effector desired final conditions, the target point is orbiting on a circular concentric co-planar orbit characterized by a difference in radius equal to d_o. Consequently, the expressions for the quantities appearing in Eq. (2.5) are

formally the same as those reported for the base c.m. with the difference that $R_o + d_o$ replaces R_o, $\Omega_{o_{tar}} = \sqrt{\mu_E/(R_o + d_o)^3}$ replaces Ω_o and $t = t_f$. This target point could well represent the grasping point on a target satellite to be captured by the SMS.

Based on all the developed considerations, it can be affirmed the optimization procedure seeks to find values for the base PD Control gains, the joint motors torques and the maneuver time duration which minimize the deployment time interval itself, the mean control effort required to the SMS actuators and the deviation of the base behavior from the desired one while not saturating the actuators, bringing the end-effector to final conditions which are compatible with sucesive grasping operations of an orbiting target satellite to be captured and keeping the maneuver duration below a user-defined maximum time limit.

Simulation parameters description

Table 2.3. Values for simulation parameters.

Parameter	Value
Base control gains (s.s. min)	1
Base control gains (s.s. max)	1000
ε_{tol}	$0.1\,\text{m}$
$\dot{\varepsilon}_{\text{tol}}$	$5 \cdot 10^{-3}\,\text{m/s}$
d_o	$3\,\text{m}$
t_{lim}	$60\,\text{s}$
n_{c_l}	60

The values for the simulation parameters have been chosen as reported in Tab. 2.3 (s.s. stands for "search space"). The last row of the table implies the open-loop control values are updated every $t_\text{f}/t_{\text{lim}}$ seconds throughout the maneuver duration. The swarm is formed by 15 particles and the algorithm iterations number has been taken equal to 100 (those parameters were furthermore chosen to take computational resources limits into account as well). For what concerns the PSO algorithm parameters, it has been set $c_1 = c_2 = 2$ and the inertia weight being defined according to the linearly decreasing rule [52] with $w_{\min} = 0.4$ and $w_{\max} = 0.9$.

Optimization procedure results

In Tables from 2.4 to 2.8 the values for the quantities relevant to the evaluation of the objective and constraint functions are reported for each particle at the end

Table 2.4. Maximum deviation of SMS base c.m. position.

Particle N.	$e_{B_{cm_{\max}}}$ (cm)
1	29.60
2	44.40
3	9.74
4	37.47
5	38.68
6	47.54
7	35.18
8	49.33
9	28.86
10	20.07
11	37.40
12	29.31
13	42.53
14	8.23
15	43.79

Table 2.5. Maximum deviation of SMS base attitude.

Particle N.	$e_{B_{att_{\max}}}$ (deg)
1	3.53
2	4.01
3	0.15
4	4.32
5	4.51
6	3.97
7	4.29
8	4.49
9	3.30
10	0.44
11	4.47
12	3.69
13	4.08
14	0.48
15	4.15

Table 2.6. Final end-effector position and velocity errors.

Particle N.	e_{EE_f} (cm)	e_{EE_f} (mm/s)
1	4.52	26.65
2	5.00	6.71
3	3.18	11.12
4	3.26	20.77
5	5.26	6.25
6	2.58	11.44
7	2.27	34.02
8	2.96	82.98
9	3.77	12.17
10	2.12	12.32
11	1.94	18.56
12	2.47	115.41
13	2.96	145.11
14	2.31	13.55
15	2.13	15.66

Table 2.7. Maneuver time duration.

Particle N.	t_{man} (s)
1	19.0
2	65.7
3	14.1
4	21.6
5	46.0
6	30.7
7	40.8
8	55.5
9	14.1
10	13.1
11	83.2
12	17.4
13	18.6
14	12.1
15	55.5

Table 2.8. Mean control effort required to the on-board actuators system.

Particle N.	u_{mean}
1	96.4
2	106.0
3	83.3
4	84.9
5	103.0
6	82.3
7	83.9
8	113.2
9	108.5
10	221.1
11	81.6
12	82.2
13	70.6
14	150.1
15	97.0

of the optimization procedure (i.e. after the last iteration of the PSO algorithm). The solution vector associated to each particle is not listed here for the sake of conciseness given the large size of the latter. The tables show how the solutions which were found induce a contained disturbance on the SMS base center of mass (of the order of decimeters), and the magnitude of the deviation of its attitude from the desired behavior is always kept below 5 deg. Looking at Tab. 2.6, it can be noticed how the end-effector final position error falls within the prescribed tolerance for the entire swarm of particles; on the contrary, the final velocity errors are still too high compared to the adopted threshold value stated above (particles 2 and 5 are the ones characterized by the lowest errors). Speaking about the maneuver duration, Tab. 2.7 reports a quite diversified range of values and the same feature can be found, though in a less pronounced fashion, for what concerns the overall mean control effort required to the on-board actuators system (see Tab. 2.8). It can be seen how in two occasions (particles 2 and 11) the computed maneuver time exceeds the boundaries of the desired search space.

Despite some of the drawbacks, the algorithm has shown a quite fast convergence rate (i.e. each particle converging to its own final value) within a relatively small number of iterations. Improvement margins are surely present as the optimization procedure has several parameters which can be tuned (see Section 2.1) to increase the quality of the results and make them resemble more the desired ones. Nevertheless, as

literature reports, it is hard to give general guidelines and tests need to be conducted for the specific application under examination. Increasing the swarm population and the number of algorithm iterations would surely help in the search for better solutions under the imposed objectives and constraints, although one must also take into account that doing so will lead to a noticeable computational cost increment. Furthermore, one can reasonably intervene on the user-defined constraints if some operational flexibility is yet admissible.

2.1.4 Conclusions

The present chapter has dealt with a preliminary application of a Multi-Objective Constrained Particle Swarm Optimization approach to the deployment maneuver of a robotic arm mounted on a space free-flying base platform. Both advantages and drawbacks regarding this application have been detected and suggestions on how to potentially overcome the latter have been given.

2.2 Neural Networks applied to a space manipulator deployment maneuver

Another approach which can be adopted to address the challenges characterizing the deployment phase involves the use of Neural Networks (NNs). The latter have widely proved to have powerful capability in solving data-driven nonlinear modeling problems and hence they can represent a viable solution for space activities. Nonetheless, Deep Neural Network (DNN) architectures and the related Deep Learning (DL) techniques can be adopted in order to embed a complex and automatic feature extraction process in the training process and to make performances independent of the physical nature of data to be processed. In the present section, DL strategies applied to the deployment maneuver of a SMS are investigated. The purpose is to design a DNN controller, basically dealing with data regression and model inversion, which could provide proper control inputs when the desired trajectory is given, in a way that the controller can autonomously adapt if the task is changed. In particular, Long Short-Term Memory (LSTM) networks for SMS data prediction are adopted. The latter are a type of Recurrent Neural Network (RNN) able to learn long-term dependencies among data [53]. Structural flexibility and joint friction features are included in the dynamic model. Details regarding implementation, training and validation of the testbed are presented and discussed as well.

2.2.1 Space Manipulator System description

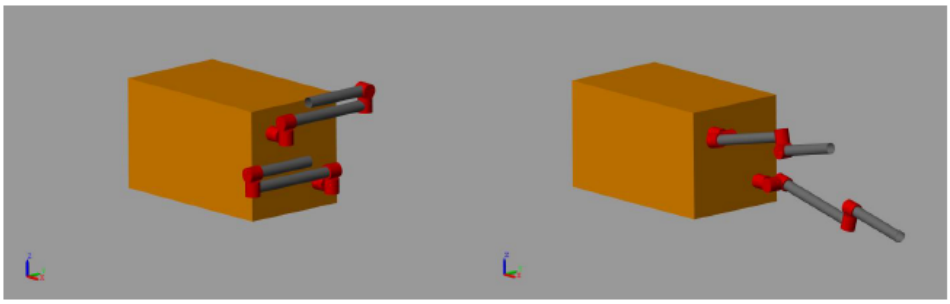

Figure 2.2. Space Manipulator System: stowed (left) and deployed (right) configuration.

The SMS here being considered is depicted in Fig. 2.2. It is formed by a prismatic base (having dimensions $2.5 \times 1.5 \times 1.5$ m and mass equal to 500 kg) equipped with two 4-degree of freedom robotic arms. The joints (weighing 20 kg each, including the motor weight) are all of revolute typology with axes allowing the arms motion in three-dimensional space. The links are aluminum hollow cylinders having diameter and thickness respectively equal to 15 cm and 3 mm. Furthermore, the first one is 1.3 m long and the second one 1.0 m. While the base platform is rigid, the arms links are structurally flexible (modeled by using 1D beam elements). As far as the actuators are concerned, the former is equipped with thrusters and control moment gyros aligned to its body-axes (which are parallel to the base edges) for respectively controlling its position and orientation; on the other hand, a rotational motor is placed at each revolute joint. The maximum actions which can be provided by the

Table 2.9. Maximum control actions that can be supplied by the SMS actuators.

Actuator	Maximum value of supplied control action
Base thrusters	50 N
Base ACS	50 N m
Revolute joints motors	30 N m

control hardware are listed in Tab. 2.9. Joint friction is considered as well and has been modeled as a function of relative angular velocity between the interconnected bodies; in particular, it has been assumed to be the sum of Stribeck, Coulomb and viscous components [54]. The numerical testbed has been developed within the Matlab Simscape environment together with Simulink for the definition of the control system architecture (see Fig. 2.3). This simulation methodology allows for complex mechanical features to be included into the model and to simultaneously

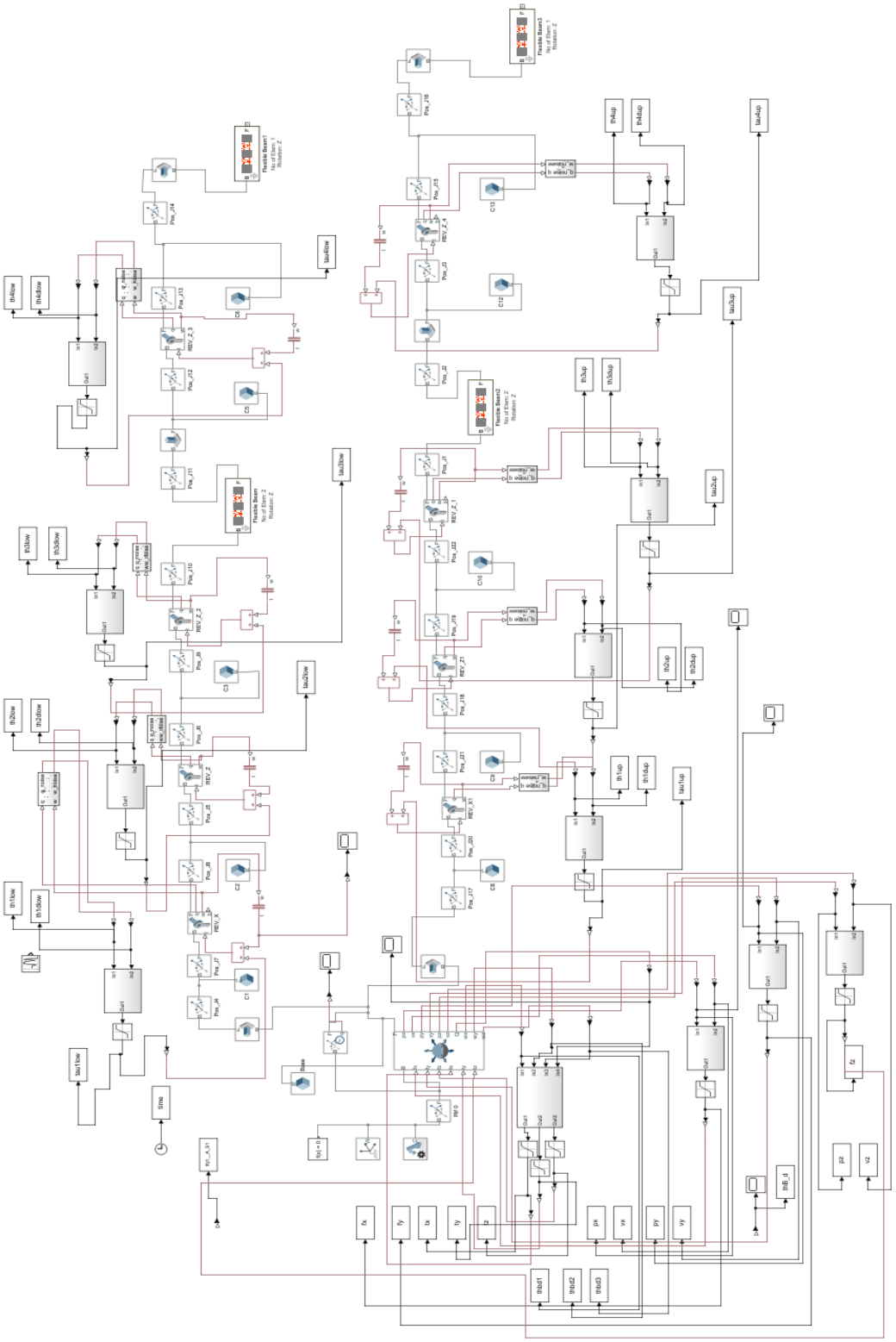

Figure 2.3. Space Manipulator System and control architecture model developed within the Simscape and Simulink environment.

develop the control plant within the same simulation environment thus reducing the overall computational cost (which is a rather relevant aspect when analyzing articulated dynamic systems as space manipulators are).

2.2.2 Long Short-Term Memory Networks

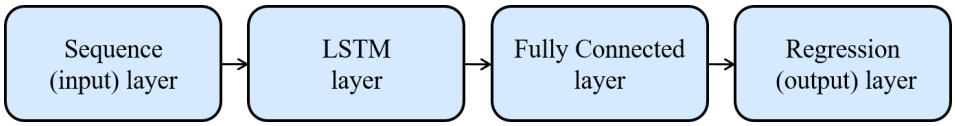

Figure 2.4. Architecture of the adopted LSTM network.

In the following, LSTM networks will be adopted as the reference forecasting model. LSTM models have been introduced in [55] and they have been proved to be effective in several fields, in particular time series forecasting. They are specifically designed to take advantage of long-term dependencies, being able to efficiently tackle a class of problems SMSs dynamics and control can be framed within. By introducing the ability of suitably handling past information in a single cell, DNN architectures can benefit from connecting several LSTM layers. The architecture here used is illustrated in Fig. 2.4 with the following details:

1. Sequence layer sets the data structures for backward training and feed-forward test at each time step;

2. LSTM layer (embedding) is a LSTM layer, as described in the following, with a number of hidden units that aim at reconstructing the internal state evolution of the unknown observed system;

3. LSTM layer (prediction) is the LSTM layer in which, starting from the embedded internal state, prediction is performed considering the long-term dependencies learned by the recurrent dynamical model;

4. Fully-Connected layer is a standard feed-forward layer connecting all the hidden units in the LSTM layer to the output, acting independently at each time step;

5. Regression layer computes the half-mean-squared-error loss at the output for the regression problem to be solved during training.

Let $\boldsymbol{S}[n]$, $n > 0$ be a vector time series to be predicted, assuming the current sample at time step n and all the previous ones as known. For every time step, the first LSTM layer will be fed by a N_i-dimensional column vector $\boldsymbol{x}_n \in \mathbb{R}^{N_i}$, whose entries

are those of the current sample $\boldsymbol{S}[n]$ and, possibly, of other previous samples that are chosen by using a suited criterion [56]. The LSTM layer is made of N_h hidden units; each unit computes at time n the scalar output or "hidden state" $h_n^{(m)}$ and the scalar "cell state" $c_n^{(m)}$, $m = 1, \ldots, N_h$. The column vectors $\boldsymbol{h}_n \in \mathbb{R}^{N_h}$ and $\boldsymbol{c}_n \in \mathbb{R}^{N_h}$, whose entries are the related scalar values, will represent the whole hidden state and the whole cell state of the LSTM layer at time n. Each unit computes both its hidden and cell states in recursive fashion, taking $\boldsymbol{x}_n$ and the previous states $\boldsymbol{h}_{n-1}$, $\boldsymbol{c}_{n-1}$ as inputs (the latter coming from itself and all other units). At each time step, the layer adds information to or removes it from the cell state. This control is carried on via the "gates" in each hidden unit; at time n, the gate outputs are computed in the m-th hidden unit, $m = 1, \ldots, N_h$, as follows:

- Input gate (i) regulates how much of the current input to let through for the newly computed state:

$$i_n^{(m)} = \sigma_g(\boldsymbol{w}_i^{(m)}\boldsymbol{x}_n + \boldsymbol{r}_i^{(m)}\boldsymbol{h}_{n-1} + b_i^{(m)}) \tag{2.8}$$

- Forget gate (f) regulates how much of the previous state to let through:

$$f_n^{(m)} = \sigma_g(\boldsymbol{w}_f^{(m)}\boldsymbol{x}_n + \boldsymbol{r}_f^{(m)}\boldsymbol{h}_{n-1} + b_f^{(m)}) \tag{2.9}$$

- Cell candidate (g) regulates the selective memory of the past:

$$g_n^{(m)} = \sigma_c(\boldsymbol{w}_g^{(m)}\boldsymbol{x}_n + \boldsymbol{r}_g^{(m)}\boldsymbol{h}_{n-1} + b_g^{(m)}) \tag{2.10}$$

- Output gate (o) regulates how much of the internal state to expose to the external network (higher layers and successive time step):

$$o_n^{(m)} = \sigma_g(\boldsymbol{w}_o^{(m)}\boldsymbol{x}_n + \boldsymbol{r}_o^{(m)}\boldsymbol{h}_{n-1} + b_o^{(m)}) \tag{2.11}$$

Row vectors $\boldsymbol{w}_\gamma^{(m)} \in \mathbb{R}^{N_i}$ represents the LSTM input weights of the gates; row vectors $\boldsymbol{r}_\gamma^{(m)} \in \mathbb{R}^{N_h}$ represent the LSTM recurrent weights; $b_\gamma^{(m)} \in \mathbb{R}$ are scalar values representing the LSTM biases; $\sigma_g(\alpha) = (1 + e^{-\alpha})^{-1}$ is the sigmoid activation function; $\sigma_c(\alpha) = \tanh\alpha$ is the hyperbolic tangent activation function; $\gamma \in \{i, f, g, o\}$ denotes the specific gate type. The cell state of the unit is given by:

$$c_n^{(m)} = f_n^{(m)} c_{n-1}^{(m)} + i_n^{(m)} g_n^{(m)} \tag{2.12}$$

and the hidden state is defined as:

$$h_n^{(m)} = o_n^{(m)} \sigma_c(c_n^{(m)}) \tag{2.13}$$

In Fig.2.5 a compact representation of the LSTM layer is shown.

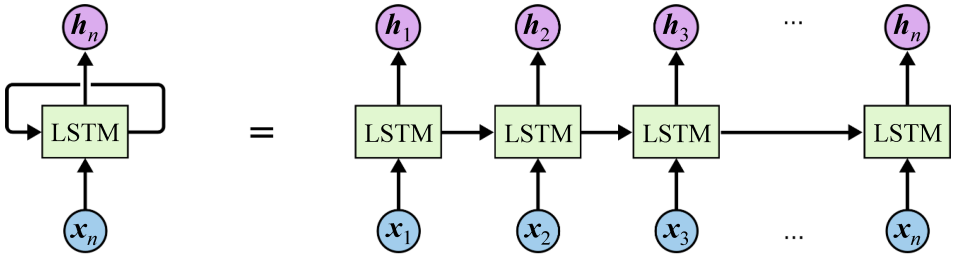

Figure 2.5. Unrolled architecture of the LSTM layer: the hidden state $\boldsymbol{h}_n$ at time n basically depends on the input $\boldsymbol{x}_n$ at same time and on the previous state $\boldsymbol{h}_{n-1}$; this is equivalent to programmatically consider n cascaded blocks where hidden states are propagated properly instead to feed back a same (unique) LSTM block.

The second LSTM layer works similarly, but, in this case, instead of $\boldsymbol{x}_n$, the input to the layer will be the vector $\boldsymbol{h}_n$ of hidden states determined by the previous LSTM layer. The final output $\boldsymbol{y}_n \in \mathbb{R}^{N_o}$ of the LSTM network at time n is computed by the Fully Connected layer, by using the hidden states $\boldsymbol{h}_n^{'}$ computed by the second LSTM layer:

$$\boldsymbol{y}_n = \mathbf{W}_d \boldsymbol{h}_n^{'} + \boldsymbol{b}_d \tag{2.14}$$

where $\mathbf{W}_d \in \mathbb{R}^{N_o \times N_h}$ and $\boldsymbol{b}_d \in \mathbb{R}^{N_o}$ are weights and biases of the layer, respectively.

The parameters to be trained in this model are the 12 matrices for each LSTM layer, for a total of 24 matrices for both the LSTM layers, plus the output matrices $\mathbf{W}_d$ and $\boldsymbol{b}_d$. In order to deal with a compact representation of the parameter space, a column vector $\boldsymbol{\theta}$ will store all the elements of these matrices, which are the parameters to be trained. An important remark must be done on the output $\boldsymbol{y}_n$ and its association with future samples of the predicted time series. In fact, the relation $\tilde{S}[n+q] = y_n$ is commonly used, where $N_o = 1$ and $\tilde{S}[n+q]$ is the estimated sample at a prediction distance $q > 0$, although other options can be adopted to this end [57].

Generally, the initialization of the network parameters $\boldsymbol{\theta}$ is random and hence the performances are not always the same as the final parameters depend upon the specific initialization. The parameters estimation needs the N_r input-output pairs $\{\boldsymbol{x}_\tau, \boldsymbol{y}_\tau\}$ (i.e. the training set), where index τ spans within the time indices of the pairs known before learning. The training algorithm used in this study is the

adaptive moment estimation (ADAM) introduced in [58].

2.2.3 Application of LSTM networks to the SMS robotic arms deployment maneuver

A strategy based on LSTM networks will be applied to the deployment maneuver of the SMS robotic arms. As stated in the previous section, such type of approach requires the definition of a training set. The generic input consists of the base position and attitude variables and each joint angle and relevant joint angle rate, for a total of $N_i = 28$ variables; on the other hand, the generic output is formed by the control actions provided by the SMS actuators, for a total of $N_o = 14$ variables (for the sake of completeness, the first six components, concerning the base platform, are expressed with respect to the inertial frame and they are suitably derived from the actions supplied by the base actuators themselves). It has to be noticed each actuator supplies a control action responding to a set-point Proportional-Derivative (PD) control law acting on the relevant variables (i.e. the base control forces will implement a control based on the platform position and linear velocity errors, the base control torques on the platform attitude and angular velocity errors and the joint motors will refer to the errors on the joint angle and joint angle rate). In

Table 2.10. Reference values used for neural network training.

Variable	Reference value
K_{p_B}	500
K_{d_B}	2000
K_{p_J}	100
K_{d_J}	500
$\theta_{J_{11}} = -\theta_{J_{21}}$	90°
$\theta_{J_{12}} = \theta_{J_{22}}$	80°
$\theta_{J_{13}} = \theta_{J_{23}}$	90°
$\theta_{J_{14}} = -\theta_{J_{24}}$	0°

order to gather the necessary data for network training, 500 deployment maneuvers have been carried out. The maneuvers have a duration of 70 s (the latter is a user-defined value and could as well be changed). K_{p_B} and K_{d_B} are respectively the base proportional and derivative gains, K_{p_J} and K_{d_J} are the same quantities but referred to the joints instead. The variable $\theta_{J_{ij}}$ is the desired relative angle for the j-th joint of the i-th arm (the corresponding desired rates are held constant to a null value and are not reported in table for the sake of conciseness). The adopted logic

was to randomly choose parameters for the PD Control gains and the desired values for joint angles and corresponding desired rates (i.e. the set-point control parameters to be used in each simulation) within certain ranges. The latter have been obtained by setting a reference value for each parameter (shown in Tab. 2.10) and having the interval range $\pm 5\%$ about the reference value itself. This allows for a diversification of the training set and a consequent wider range of operational capability for the proposed LSTM-based control strategy. It has to be underlined each of the cases within the training set has to be considered as a nominal one. The desired position and orientation of the base platform (and the relevant time derivatives) are kept fixed to null values.

The methodology used for the NN training and testing is the so-called *key-folding*; in particular, a 20-fold structure has been chosen. This means that 480 input-output pairs of time series are used for training the network (i.e. identifying the above cited matrices) and 20 are instead tested in order to evaluate the forecasting performance of the developed NN. The selection of the 20 pairs to be used takes place in a random fashion and the procedure is repeated for a total of 25 times ($20 \times 25 = 500$); nevertheless, the algorithm is formulated in such a way, each time, the 20 sets used for network testing do not include any which have been already chosen for the same purpose in a previous iteration. In this way, all pairs will have been used for both training and testing at the end of the procedure, thus guaranteeing a full exploitation of the available data. Furthermore, in order to overcome the above stated issue regarding the variability of network performance depending upon the specific initialization of network parameters, the entire procedure has been replicated for 20 times using different initial sets of the LSTM matrices. Finally, the number of LSTM cells and hidden states $\boldsymbol{h}_n$ in the first LSTM layer is set to 40, whilst the same number $\boldsymbol{h}_n^{'}$ in the second LSTM layer is set to 10. Tab. 2.11 reports the Root Mean Square Error and Standard Deviation of the output variables. The latter are computed over $20 \times 25 \times 20 = 10000$ tests. Furthermore, Figures from 2.6 to 2.11 show indicative plots where the real (i.e. derived from the test sequences descending from the Simscape model simulation and taken as reference ones) and predicted values of the outputs are compared. It can be seen how the LSTM network is able to predict the behavior of the relevant control actions with quite good accuracy. There are some deviations between the real and predicted trends; nevertheless, this shortcoming may as well be solved by further increasing the dimensions of the adopted dataset for the NN training and also by trying a different tuning of the training algorithm hyperparameters.

Table 2.11. Details of the simulation: Root Mean Squared Error (RMSE) and Standard Deviation of the outputs.

Variable	RMSE	St. Dev.
F_{B_x} (N)	0.165	0.054
F_{B_y} (N)	0.101	0.034
F_{B_z} (N)	0.144	0.044
T_{B_x} (N m)	0.108	0.039
T_{B_y} (N m)	0.343	0.103
T_{B_z} (N m)	0.242	0.083
$T_{J1_{UP}}$ (N m)	0.352	0.181
$T_{J2_{UP}}$ (N m)	0.273	0.068
$T_{J3_{UP}}$ (N m)	0.061	0.026
$T_{J4_{UP}}$ (N m)	0.056	0.025
$T_{J1_{DOWN}}$ (N m)	0.356	0.178
$T_{J2_{DOWN}}$ (N m)	0.171	0.041
$T_{J3_{DOWN}}$ (N m)	0.055	0.025
$T_{J4_{DOWN}}$ (N m)	0.056	0.026

Figs. 2.8b and 2.10b show the predicted control torque slightly exceeds the limit on the available joint torque. This problem can be easily avoided by introducing a saturation on the control actions provided by the actuators when the LSTM-based strategy is used to compute them. One last comment has to be made with respect to the lack of data in the reported figures from $t = 0$ to $t = 1\,\mathrm{s}$. This is due to the so-called "dropout" of the network; it is an intrinsic time interval the NN needs to properly start "tracking" the system. The value of $t = 1\,\mathrm{s}$ is a quite conservative choice for such parameter. It could well be reduced to diminish this initial time gap. The reported figures are relative to different tests instead of a single one. This has purposely been done in order to show how the prediction performed by the NN exhibits a good quality on a different variety of experiments. The torques computed by means of the LSTM-based strategy will be applied in an open-loop fashion to the SMS to accomplish the desired task.

It has to be underlined a NN-based control is intrinsically not robust in the sense it is not able to deal with desired conditions falling out from the ranges within which the network has been trained. Consequently, it is definitely desirable to have a training set as wider as possible. Furthermore, a feedback compensation is always to be introduced to properly manage uncertainties and disturbances not accounted for in the network training, thus making the overall control system robust within the training set ranges (this issue raises as the model used for network training may

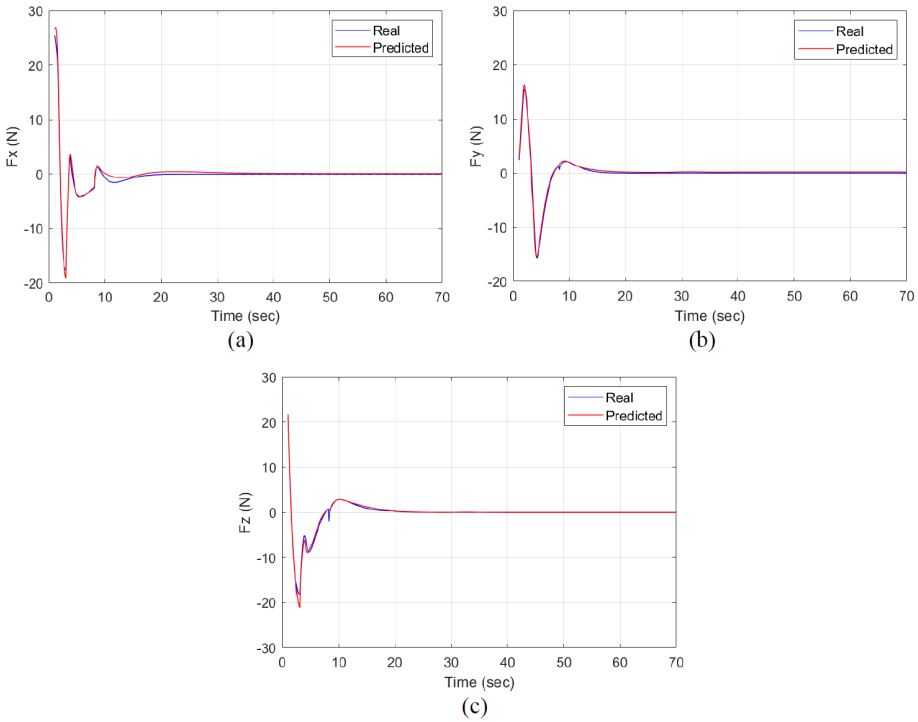

Figure 2.6. Base control force inertial components: (a) X axis, (b) Y axis, (c) Z axis.

present some differences with respect to the actual conditions the manipulator will exhibit when operating in orbit).

It is important to once again highlight how the NN is capable of changing its output to adapt to a different input (within the workspace used for training the network itself), thus allowing for a greater operational flexibility as the diversification of the training set is enhanced.

2.2.4 Conclusions

Neural networks can represent an innovative approach to the control of autonomous space robotic manipulator systems. A LSTM-based strategy has been implemented to predict the behavior of a two-arm space manipulator and to properly tune the necessary control actions finalized to its deployment maneuver. The proposed approach has proved to be suitable for such kind of application showing good performance and effectiveness.

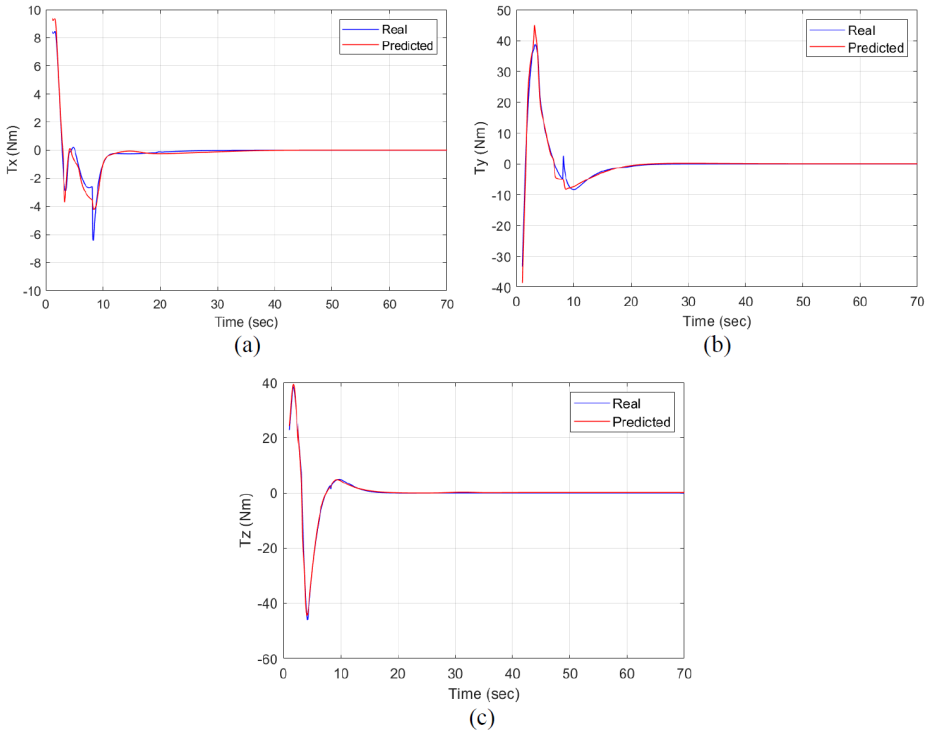

Figure 2.7. Base control torque inertial components: (a) X axis, (b) Y axis, (c) Z axis.

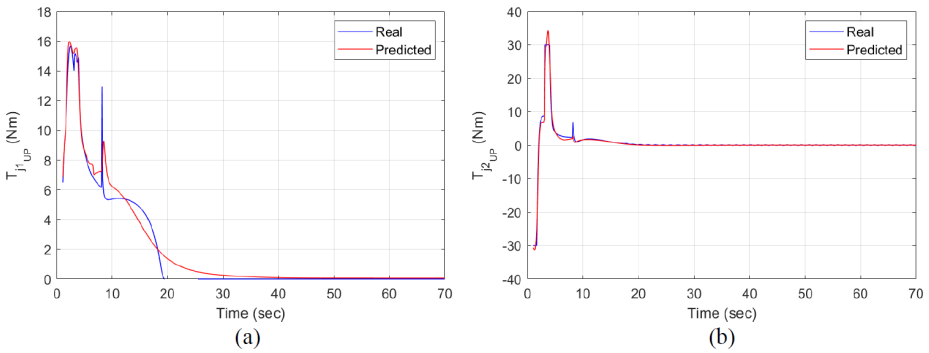

Figure 2.8. Upper arm joint torques: (a) First joint, (b) Second joint.

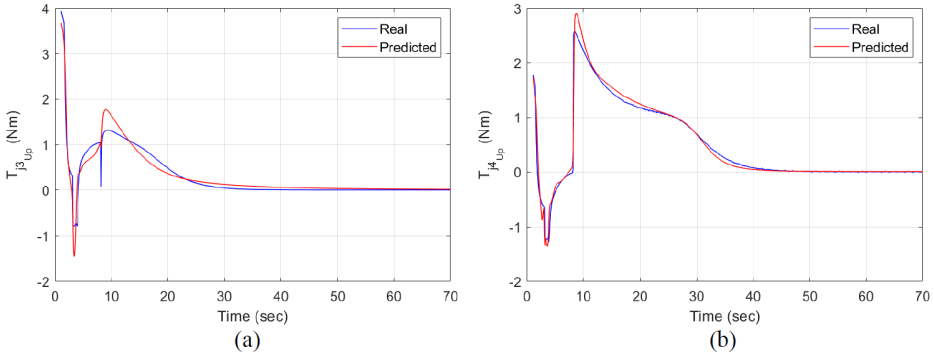

Figure 2.9. Upper arm joint torques: (a) Third joint, (b) Fourth joint.

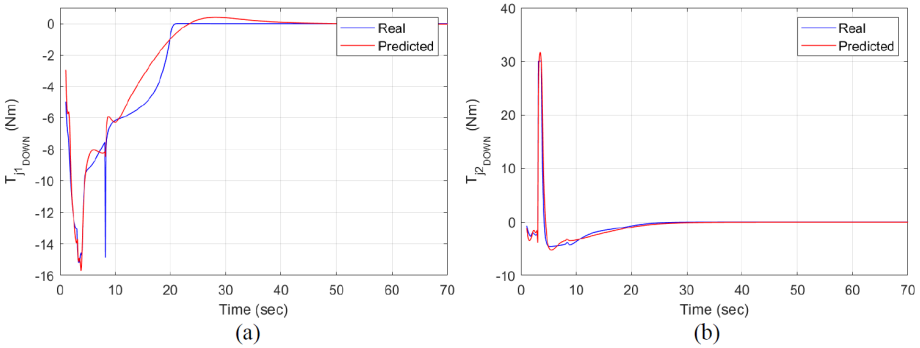

Figure 2.10. Lower arm joint torques: (a) First joint, (b) Second joint.

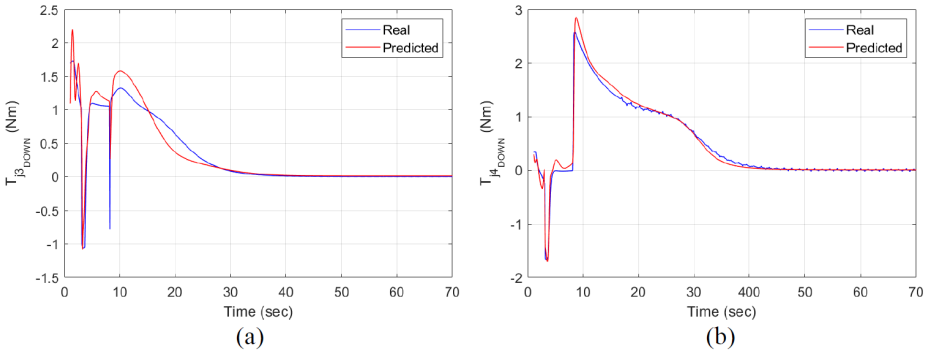

Figure 2.11. Lower arm joint torques: (a) Third joint, (b) Fourth joint.

Chapter 3

Impedance Control applied to Space Manipulator Systems

The pre-grasping phase has the objective of maintaining a stable contact between the manipulator terminal parts (i.e. the end-effectors) and a target object without a solid grasp which can be later obtained by means of an ad-hoc mechanism. At the same time, it is convenient to reduce the target initial relative translational and angular velocities as close to zero as possible before proceeding with the successive grasping phase. The Impedance Control approach is a suitable strategy to solve this problem. In the latter, the end-effector is controlled in order to make it behave like a mass-spring-damper system regardless of the reaction motion of the base so to absorb the impact energy [59]. Previous studies [60],[61],[62] considered a point-mass target and one-dimensional contact dynamics; however, the contact between the manipulator and target could generate a perturbation on the attitude of the target producing an unwanted rotational motion of the latter. Indeed, a two-dimensional contact dynamics between a target and a robotic arm needs further investigations when the control law must be defined. For what concerns impact control, in [63],[64] the goal of the developed control strategy is to minimize the impact on the attitude of the servicing satellite. This is done by finding an optimal time and the corresponding motion state of the tumbling satellite such that the physical interception from capturing operation will have zero or minimal attitude impact on the servicing satellite. Since the control acts before a physical contact happens, it will not affect but actually augment any existing force or impedance control capability of the manipulator. In [65] a full 3D model of a free-flying space robot is proposed, but only a one-arm manipulator with a very simple contact model

and a reduced 2D simulation scenario is presented. In [66] an impedance control algorithm based on velocity is developed for a low impact docking mechanism.

The present chapter investigates the application of the Impedance Control approach to a two-arm space manipulator used to capture a non-cooperative target. The combination of Impedance Control together with Proportional-Derivative (PD) Control (referred to as Impedance+PD Control) is also presented and implemented. The performance of the proposed control architecture will be evaluated by means of a co-simulation involving the MSC Adams multi-body tool (for describing the dynamics of the space robot and target and the contact phase) together with Matlab/Simulink (for the determination of the control actions which is based on a multi-body model of the dynamic system). The co-simulation is a particularly useful tool to implement robust control applied to detailed dynamic systems.

3.1 Impedance control concept and state of the art

Most of the robotic missions, as the ones performed by the ISS Canadarm or the ones proposed for future automatic missions, include both free motion and contact tasks, such as tracking a desired trajectory and interacting with the external environment at specific points, respectively. Hybrid Position/Force Control [67] has been the basic strategy of many of the proposed implementations. The control of a robot during "free motion" tasks (i.e. operations in which the system does not interact with external objects) and the control during contact tasks are considered as two different operational modes: in the case of free motion, an algorithm for position control can be used, whereas, in the case of contact, the interaction of the robot with the external environment has to be managed by means, for example, of force/impedance algorithms. The Impedance Control strategy is a suitable solution to control the interaction forces and the response of the system during contact with external objects.

Impedance Control provides compliant behavior of a manipulator in dynamic interaction with its environment. An impedance controller enforces a relationship between the forces and moments acting on the manipulator end-effector and the acceleration, velocity and position errors of the manipulator end-effector itself [59],[61] (see Fig. 3.1 for the scheme of the Impedance Control approach). The concept of impedance matching has been proposed in the past to find the control parameters in order to optimize Impedance Control both from the transient and stationary response point of view [68]. Furthermore, it was shown that if the magnitude of the

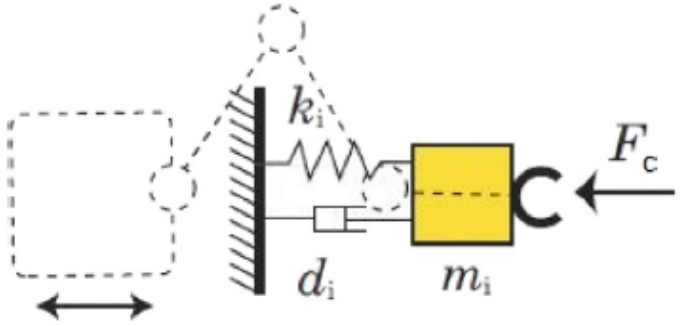

Figure 3.1. Impedance Control concept for a space manipulator [59].

impedance is equal to or lower than that of impedance matching, stable contact can be achieved; in contrast, if the impedance is larger than that of impedance matching, there is no stable contact [69]. Experimental and numerical investigations on the performance of Impedance Control implemented on elastic joints have shown the benefits of adopting this control strategy in compensating undesirable effects caused by system flexibility[70].

In the past, the Object Impedance Control (OIC) technique has been developed in the context of multiple fixed-base mounted robotic arms manipulating a common object [71]. OIC enforces a designated mechanical impedance not for the end-effector of a single arm, but for the manipulated object itself. This control strategy is adopted to make the manipulated object behave as if it were a reference mechanical impedance. However, it has been recognized that applying OIC to the manipulation of a flexible object can lead to instability. This instability problem could be solved either by increasing the desired mass parameters or by filtering the frequency content of the estimated contact force.

More recently, the Multiple Impedance Control (MIC) algorithm has been developed for several cooperating robotic systems manipulating a common object. In [72] MIC is studied in the context of space robotic systems. MIC formulation is employed to impose a reference mechanical impedance to all the elements of a space manipulator (including its base and endpoints) and the manipulated object; in this way an accordant motion of the various subsystems during object manipulation tasks is guaranteed.

In the present chapter, the formulation of Impedance Control proposed in [59] is extended to a two-arm free-floating manipulator system with a particular emphasis on the impact and post-impact phases with an external target satellite. As a matter of fact, there are scenarios in which the use of two or more robotic arms may be

preferable (if not mandatory). These give rise to new issues:

1. The dynamics model has to take into account the interaction between three components of the multi-body system, i.e. the base platform and the two arms, instead of two as in [59] and this is a source of complication in the development of the model itself which is here addressed;

2. The control architecture becomes more sophisticated than that presented in [59].

Furthermore, a dedicated control for the bus based on specific requirements will be introduced. One has to consider that, generally speaking, the control actions have to be determined taking the dynamic coupling among them into consideration. In particular, a control strategy including a PD Control for the base and two Impedance Controls for the arms (which is able to decouple each part of the overall control strategy from the others) is developed and the relevant mathematical formulation is detailed [73]. Within this chapter, all the mathematics is derived in a 2D inertial reference frame, i.e. the motion of the manipulator and target is planar. The origin of the frame is located at the position of the SMS base center of mass at $t = 0$. Rigorously speaking, this should be an orbital reference frame (relative, for example, to the orbit on which the base center of mass is moving before the beginning of the considered maneuver) which is not inertial; nevertheless, in the case study that will later be presented, the considered time interval is relatively short and this justifies neglecting the orbital curvature and to assume the orbital motion as uniform rectilinear thus allowing one to consider the reference frame as inertial. Furthermore, the reduced time scale here involved also allows for the gravitational actions effects to be neglected as well. Furthermore, $\boldsymbol{Q}$ is here defined as the vector containing the base position and attitude variables, the arms joint angles and the distances of the centers of mass of the end-effectors contact plates (see Fig. 3.3) from the endpoint of the corresponding arm last link.

As far as the impact and post-impact dynamics among the end-effectors and the target is concerned, this is modeled through the MSC Adams multi-body software which is also employed in the verification process that enables the detailed simulation of these complex dynamic interactions.

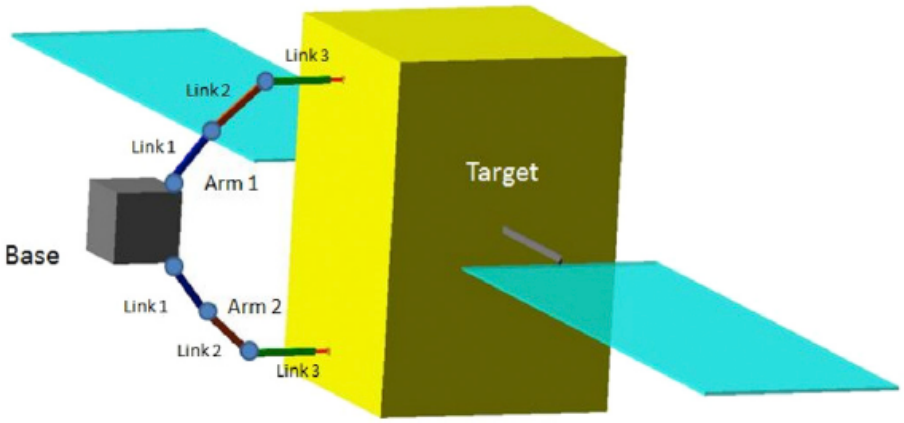

Figure 3.2. Schematic of the multi-body space manipulator and target satellite.

3.2 Two-arm multi-body space manipulator and target satellite description

In Fig. 3.2 the schematic of the two-arm space manipulator (on the left) and target satellite (on the right) is reported.

The manipulator usually suffers from flexible effects caused by joints clearance, gears friction and links elastic behavior. Some interesting researches propose to increase this elasticity in order to exploit its potential advantages over the conventional "rigid" robotic manipulators [74]. on the other hand, the most common choice, which is also adopted here, is to design the manipulator so that the elastic dynamics is reduced as far as possible, and therefore, in a first approximation, all the parts of the multi-body system will be considered as actually rigid.

The first link of each robotic arm is connected to the base platform by means of a revolute joint and the links are connected with each other by revolute joints as well.

The two end-effectors are formed by a contact plate which is connected to the last link of the corresponding arm by means of a prismatic joint, i.e. it can only translate relatively to the last link along the direction of the latter (see Fig. 3.3), and a spring-damper mechanism. This special configuration of the end-effector will be shortly discussed.

The length of the links, as reported in Tab. 3.1, ensures safe operations by keeping a safety distance between the chaser base and the target. The position of the arms shoulders on the bus has been opportunely chosen in order to take also advantage of the size of the bus to reach two points fixed on one face of the target

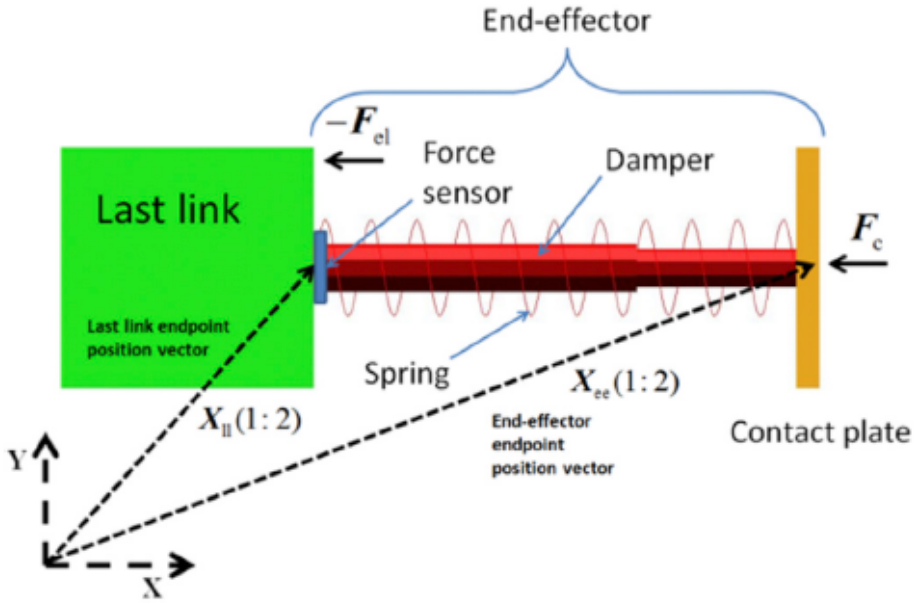

Figure 3.3. Schematic of the end-effector: Spring stiffness coefficient 300 N/m, Damper damping coefficient 20 N s/m.

Table 3.1. Properties of the links of the space manipulator.

Link	Mass kg	Length m	J_J kg m^2
1	20.00	1.10	6.93
2	20.00	1.10	6.93
3	19.27	1.05	6.56

which are functional to the successive grasping phase. The target is considered as a rigid central body with two appendages rigidly attached to the main bus.

The base of the manipulator has a cubic shape of length 1 m, its mass is $m_B = 500\,\mathrm{kg}$ and its moment of inertia about the z axis of the center of mass body-fixed reference frame is $J_B = 83.33\mathrm{kg\,m^2}$. The contact plate reported in Fig. 3.3 is 0.10 m high, with a mass of 0.35 kg and a moment of inertia of $2.95 \cdot 10^{-4}\,\mathrm{kg\,m^2}$. The spring length at rest is 0.2 m. Tab. 3.1 also reports the moments of inertia of the links referred to their left-end revolute joint. The mass of the target is 2721 kg and its moment of inertia about the z axis of the center of mass body-fixed reference frame is $7895\,\mathrm{kg\,m^2}$.

3.3 Impedance Control for a space manipulator

In the Impedance Control approach the end-effector is controlled in order to make it behave like a mass-spring-damper system regardless of the reaction motion of the base so to absorb the impact energy. The Impedance Control concept is illustrated in Fig. 3.1 in a simple one-dimensional context; one should actually imagine a complete set of orthogonal translational and rotational mass-spring-damper systems, i.e. a translational one along the x inertial axis, a translational one along the y inertial axis and a rotational one about the z inertial axis.

The Impedance Control law is defined as:

$$\mathbf{M}_{\mathrm{i}_k}\ddot{\boldsymbol{X}}_{\mathrm{ee}_k} + \mathbf{D}_{\mathrm{i}_k}(\dot{\boldsymbol{X}}_{\mathrm{ee}_k} - \dot{\boldsymbol{X}}_{\mathrm{ee}_{\mathrm{des}_k}}) + \mathbf{K}_{\mathrm{i}_k}(\boldsymbol{X}_{\mathrm{ee}_k} - \boldsymbol{X}_{\mathrm{ee}_{\mathrm{des}_k}}) = \boldsymbol{A}_{\mathrm{c}_k}, \quad k = 1, 2 \tag{3.1}$$

where $\ddot{\boldsymbol{X}}_{\mathrm{ee}_k} \in \mathbb{R}^{3\times1}$, $\dot{\boldsymbol{X}}_{\mathrm{ee}_k} \in \mathbb{R}^{3\times1}$, $\boldsymbol{X}_{\mathrm{ee}_k} \in \mathbb{R}^{3\times1}$ are respectively the k-th end-effector endpoint acceleration, velocity and position (translational and angular ones (actually, the angular ones are those of the end-effector itself)), $\dot{\boldsymbol{X}}_{\mathrm{ee}_{\mathrm{des}_k}} \in \mathbb{R}^{3\times1}$, $\boldsymbol{X}_{\mathrm{ee}_{\mathrm{des}_k}} \in \mathbb{R}^{3\times1}$ are their desired values, $\mathbf{M}_{\mathrm{i}_k} \in \mathbb{R}^{3\times3}$, $\mathbf{D}_{\mathrm{i}_k} \in \mathbb{R}^{3\times3}$, $\mathbf{K}_{\mathrm{i}_k} \in \mathbb{R}^{3\times3}$ are the Impedance Control matrices (denoting by $\mathbf{I}$ the identity matrix, they will be chosen as diagonal matrices of the form $m_{\mathrm{i}_k}\mathbf{I}^{3\times3}$, $d_{\mathrm{i}_k}\mathbf{I}^{3\times3}$, $k_{\mathrm{i}_k}\mathbf{I}^{3\times3}$) and $\boldsymbol{A}_{\mathrm{c}_k} \in \mathbb{R}^{3\times1}$ are the contact actions exerted on the k-th end-effector by the target satellite.

A problem rises: it often happens that Impedance Control cannot be sufficiently effective during contact because of the presence of actuation time delay in real systems. Therefore, the contact interface must be compliant enough for Impedance Control to be more effective to increase contact duration [75]. A way to achieve this is to place a translational spring-damper group between the arm last link and the

contact plate (see Fig. 3.3).[1] From a design point of view, it is convenient to consider the last link endpoint rather than the end-effector endpoint as the controlled point since, in this way, there are no passive elements (represented, in this case, by the spring-damper group) in between the actuators and the controlled point. This allows to consider the spring-damper force acting on the last link rather than the contact force acting on the contact plate. In fact, the spring-damper force is the external force acting on the tip of the last link just as the contact force is the external force acting on the tip of the end-effector.

On account of the above considerations, Eq. (3.1) is modified to become:

$$\mathbf{M}_{\mathrm{i}_k}\ddot{\boldsymbol{X}}_{\mathrm{ll}_k} + \mathbf{D}_{\mathrm{i}_k}(\dot{\boldsymbol{X}}_{\mathrm{ll}_k} - \dot{\boldsymbol{X}}_{\mathrm{ll}_{\mathrm{des}_k}}) + \mathbf{K}_{\mathrm{i}_k}(\boldsymbol{X}_{\mathrm{ll}_k} - \boldsymbol{X}_{\mathrm{ll}_{\mathrm{des}_k}}) = -\boldsymbol{A}_{\mathrm{el}_k}, \quad k = 1, 2 \tag{3.2}$$

where $\ddot{\boldsymbol{X}}_{\mathrm{ll}_k} \in \mathbb{R}^{3\times 1}$, $\dot{\boldsymbol{X}}_{\mathrm{ll}_k} \in \mathbb{R}^{3\times 1}$, $\boldsymbol{X}_{\mathrm{ll}_k} \in \mathbb{R}^{3\times 1}$ are respectively the k-th arm last link endpoint acceleration, velocity and position (translational and angular ones (actually the angular ones are those of the last link itself)) and $-\boldsymbol{A}_{\mathrm{el}_k} \in \mathbb{R}^{3\times 1}$ are the spring-damper actions acting on the last link of the k-th arm. To complete the governing equations, one has to express the variables characterizing the last link endpoint position and orientation as a function of the set of Kane's variables. This is done by means of a Jacobian matrix $\mathbf{J}_{\mathrm{ll}_k} \in \mathbb{R}^{3\times(8+n_{l_1}+n_{l_2})}$ (where n_{l_1} and n_{l_2} are the number of links forming the first and second arm respectively) which relates the time derivative of the former to those of the latter:

$$\dot{\boldsymbol{X}}_{\mathrm{ll}_k} = \mathbf{J}_{\mathrm{ll}_k}\dot{\boldsymbol{Q}}, \quad k = 1, 2 \tag{3.3}$$

Deriving Eq.(3.3) with respect to time, one gets:

$$\ddot{\boldsymbol{X}}_{\mathrm{ll}_k} = \mathbf{J}_{\mathrm{ll}_k}\ddot{\boldsymbol{Q}} + \dot{\mathbf{J}}_{\mathrm{ll}_k}\dot{\boldsymbol{Q}}, \quad k = 1, 2 \tag{3.4}$$

Substituting Eq.(3.4) into Eq.(3.2), the following expression for $\ddot{\boldsymbol{Q}}$ is obtained:

$$\begin{aligned}\ddot{\boldsymbol{Q}}_k = -(\mathbf{M}_{\mathrm{i}_k}\mathbf{J}_{\mathrm{ll}_k})^+ \big[\mathbf{M}_{\mathrm{i}_k}\dot{\mathbf{J}}_{\mathrm{ll}_k}\dot{\boldsymbol{Q}} + \mathbf{D}_{\mathrm{i}_k}(\mathbf{J}_{\mathrm{ll}_k}\dot{\boldsymbol{Q}} - \dot{\boldsymbol{X}}_{\mathrm{ll}_{\mathrm{des}_k}}) + \\ + \mathbf{K}_{\mathrm{i}_k}(\boldsymbol{X}_{\mathrm{ll}_k} - \boldsymbol{X}_{\mathrm{ll}_{\mathrm{des}_k}}) + \boldsymbol{A}_{\mathrm{el}_k}\big], \quad k = 1, 2\end{aligned} \tag{3.5}$$

where the + superscript indicates the pseudo-inversion operation. Eq. (3.2) is the *synthetic control*: it is the motion that must be imposed on the last link endpoint

[1] Note that the end-effector spring-damper group exists for real; it does not correspond to the imaginary spring and damper of the Impedance Control reported in Fig. 3.1.

variables to make it behave as if it was a mass-spring-damper system regardless of the reaction motion of the base (see Fig. 3.1). The subsequent step is to determine the control actions required to impose this motion coherently, of course, with the control actions that are actually available on board of the manipulator system.

The control actions here considered are two forces acting on the base along the base x and y body axes, a torque acting o the base about the base z body axis (which is parallel to the z inertial axis) and a number of torques equal to the number of joint motors whose axes lie along the joints z axes which are parallel to the z inertial axis (and, consequently, the torques they produce are about the z inertial axis).

3.3.1 Impedance+PD control strategy definition

Impedance Control does not impose any explicit requirement on the base behavior. This could be not acceptable in cases where stringent constraints on the base motion (both translational and angular) need to be satisfied. In order to overcome this problem, a suitable solution is to elaborate a control architecture where the Impedance Control involves the joint motors, while a separate control strategy is applied to the base involving the base actuators. One common approach for controlling the base of the manipulator is by means of LQR algorithms (as for example in [76]), a technique that requires the linearization of the system dynamics. Another possible choice for the base control is the use of a Proportional-Derivative (PD) algorithm. Defining $\boldsymbol{X}_B = [x_B, y_B, \theta_B]^{\mathrm{T}}$ (i.e. the vector containing the base center of mass position and the relevant attitude angle), the PD synthetic control law is given by

$$\ddot{\boldsymbol{X}}_B = -\mathbf{K}_{\mathrm{p}}(\boldsymbol{X}_B - \boldsymbol{X}_{B_{\mathrm{des}}}) - \mathbf{K}_{\mathrm{d}}(\dot{\boldsymbol{X}}_B - \dot{\boldsymbol{X}}_{B_{\mathrm{des}}}) \tag{3.6}$$

where $\mathbf{K}_{\mathrm{p}} \in \mathbb{R}^{3\times3}$ and $\mathbf{K}_{\mathrm{d}} \in \mathbb{R}^{3\times3}$ are respectively the control proportional and derivative gain matrices (in the following results they are chosen as diagonal matrices). The vector $\dot{\boldsymbol{X}}_B$ is expressed in terms of the vector $\dot{\boldsymbol{Q}}$ by means of a Jacobian matrix $\mathbf{J}_B \in \mathbb{R}^{3\times(8+n_{l_1}+n_{l_2})}$ such that:

$$\dot{\boldsymbol{X}}_B = \mathbf{J}_B\dot{\boldsymbol{Q}} \tag{3.7}$$

Deriving Eq.(3.7) with respect to time and substituting into Eq. (3.6) leads to:

$$\ddot{\boldsymbol{Q}} = -\mathbf{J}_B^{+}[\mathbf{K}_{\mathrm{p}}(\boldsymbol{X}_B - \boldsymbol{X}_{B_{\mathrm{des}}}) + \mathbf{K}_{\mathrm{d}}(\dot{\boldsymbol{X}}_B - \dot{\boldsymbol{X}}_{B_{\mathrm{des}}})] \tag{3.8}$$

The equations describing the controlled dynamics of the SMS can be written in the following form:

$$\mathbf{J}^T\mathbf{M}\mathbf{J}\ddot{\boldsymbol{Q}} = -\mathbf{J}^T\mathbf{M}\dot{\mathbf{J}}\dot{\boldsymbol{Q}} + \mathbf{J}^T\boldsymbol{C} + \mathbf{J}^T\boldsymbol{F} + \mathbf{B}_1\boldsymbol{u}_1 + \mathbf{B}_2\boldsymbol{u}_2 + \mathbf{B}_3\boldsymbol{u}_3 \tag{3.9}$$

Referring to the right-hand side of Eq. (3.9), vectors $\boldsymbol{u}_1 \in \mathbb{R}^{n_{l_1}\times 1}$ and $\boldsymbol{u}_2 \in \mathbb{R}^{n_{l_2}\times 1}$ contain the joint torques supplied by the joint motors which participate to the Impedance Control of the last link of the first and second arm respectively, while vector $\boldsymbol{u}_3 \in \mathbb{R}^{3\times 1}$ represents the base control actions which participate to the PD Control of the base. The terms $\mathbf{B}_1 \in \mathbb{R}^{(8+n_{l_1}+n_{l_2})\times n_{l_1}}$, $\mathbf{B}_2 \in \mathbb{R}^{(8+n_{l_1}+n_{l_2})\times n_{l_2}}$ and $\mathbf{B}_3 \in \mathbb{R}^{(8+n_{l_1}+n_{l_2})\times 3}$ are the matrices that map the control actions vectors onto the dynamics equations. Separately substituting the desired accelerations appearing in Eqs. (3.5) and (3.8) into Eq. (3.9), one obtains the vectors of generalized control forces:

$$\begin{aligned}\boldsymbol{u}_1 =&\mathbf{B}_1^{+}\{\mathbf{J}^{\mathrm{T}}\mathbf{M}\mathbf{J}(\mathbf{M}_{\mathrm{i}_1}\mathbf{J}_{\mathrm{ll}_1})^{+}[-\mathbf{M}_{\mathrm{i}_1}\dot{\mathbf{J}}_{\mathrm{ll}_1}\dot{\boldsymbol{Q}} - \mathbf{D}_{\mathrm{i}_1}(\dot{\boldsymbol{X}}_{\mathrm{ll}_1} - \dot{\boldsymbol{X}}_{\mathrm{ll}_{1_{\mathrm{des}}}}) - \mathbf{K}_{\mathrm{i}_1}(\boldsymbol{X}_{\mathrm{ll}_1} - \boldsymbol{X}_{\mathrm{ll}_{1_{\mathrm{des}}}})+\\ &- \boldsymbol{A}_{\mathrm{el}_1}] + \mathbf{J}^{\mathrm{T}}\mathbf{M}\dot{\mathbf{J}}\dot{\boldsymbol{Q}} - \mathbf{J}^{\mathrm{T}}\boldsymbol{C} - \mathbf{J}^{\mathrm{T}}\boldsymbol{F}' - \mathbf{B}_2\boldsymbol{u}_2 - \mathbf{B}_3\boldsymbol{u}_3\}\end{aligned} \tag{3.10}$$

$$\begin{aligned}\boldsymbol{u}_2 =&\mathbf{B}_2^{+}\{\mathbf{J}^{\mathrm{T}}\mathbf{M}\mathbf{J}(\mathbf{M}_{\mathrm{i}_2}\mathbf{J}_{\mathrm{ll}_2})^{+}[-\mathbf{M}_{\mathrm{i}_2}\dot{\mathbf{J}}_{\mathrm{ll}_2}\dot{\boldsymbol{Q}} - \mathbf{D}_{\mathrm{i}_2}(\dot{\boldsymbol{X}}_{\mathrm{ll}_2} - \dot{\boldsymbol{X}}_{\mathrm{ll}_{2_{\mathrm{des}}}}) - \mathbf{K}_{\mathrm{i}_2}(\boldsymbol{X}_{\mathrm{ll}_2} - \boldsymbol{X}_{\mathrm{ll}_{2_{\mathrm{des}}}})+\\ &- \boldsymbol{A}_{\mathrm{el}_2}] + \mathbf{J}^{\mathrm{T}}\mathbf{M}\dot{\mathbf{J}}\dot{\boldsymbol{Q}} - \mathbf{J}^{\mathrm{T}}\boldsymbol{C} - \mathbf{J}^{\mathrm{T}}\boldsymbol{F}' - \mathbf{B}_1\boldsymbol{u}_1 - \mathbf{B}_3\boldsymbol{u}_3\}\end{aligned} \tag{3.11}$$

$$\begin{aligned}\boldsymbol{u}_3 =&\mathbf{B}_3^{+}\{\mathbf{J}^{\mathrm{T}}\mathbf{M}\mathbf{J}\mathbf{J}_{\mathrm{B}}^{+}[-\mathbf{K}_{\mathrm{p}}(\boldsymbol{X}_{\mathrm{B}} - \boldsymbol{X}_{\mathrm{B}_{\mathrm{des}}}) - \mathbf{K}_{\mathrm{d}}(\dot{\boldsymbol{X}}_{\mathrm{B}} - \dot{\boldsymbol{X}}_{\mathrm{B}_{\mathrm{des}}})] + \mathbf{J}^{\mathrm{T}}\mathbf{M}\dot{\mathbf{J}}\dot{\boldsymbol{Q}} - \mathbf{J}^{\mathrm{T}}\boldsymbol{C}+\\ &- \mathbf{J}^{\mathrm{T}}\boldsymbol{F}' - \mathbf{B}_1\boldsymbol{u}_1 - \mathbf{B}_2\boldsymbol{u}_2\}\end{aligned} \tag{3.12}$$

where the modified vector of external generalized forces appearing in Eqs. (3.10)-(3.12) is defined as follows:

$$\boldsymbol{F}' = \begin{bmatrix} \mathbf{0}^{2\times1} \\ 0 \\ \mathbf{0}^{2\times1} \\ 0 \\ \vdots \\ -\boldsymbol{F}_{\mathrm{el}_1} \\ 0 \\ \mathbf{0}^{2\times1} \\ \mathbf{0}^{2\times1} \\ 0 \\ \vdots \\ -\boldsymbol{F}_{\mathrm{el}_2} \\ 0 \\ \mathbf{0}^{2\times1} \\ \mathbf{0}^{2\times1} \\ 0 \end{bmatrix} \tag{3.13}$$

whereas the vector of generalized forces $\boldsymbol{F}$ is defined as the column vector

$$\boldsymbol{F} = \begin{bmatrix} \mathbf{0}^{2\times1} \\ 0 \\ \mathbf{0}^{2\times1} \\ 0 \\ \vdots \\ -\boldsymbol{F}_{\mathrm{el}_1} \\ 0 \\ \boldsymbol{F}_{\mathrm{el}_1} + \boldsymbol{F}_{\mathrm{c}_1} \\ \mathbf{0}^{2\times1} \\ 0 \\ \vdots \\ -\boldsymbol{F}_{\mathrm{el}_2} \\ 0 \\ \boldsymbol{F}_{\mathrm{el}_2} + \boldsymbol{F}_{\mathrm{c}_2} \\ -(\boldsymbol{F}_{\mathrm{c}_1} + \boldsymbol{F}_{\mathrm{c}_2}) \\ m_{\mathrm{ct}} \end{bmatrix} \tag{3.14}$$

where $-\boldsymbol{F}_{\mathrm{el}_k}$, $k = 1, 2$ (corresponding to the first two rows of vector $-\boldsymbol{A}_{\mathrm{el}_k}$ in Eq. (3.2)) is the spring-damper force acting on the last link of the k-th arm, $\boldsymbol{F}_{\mathrm{c}_k}$, $k = 1, 2$ (corresponding to the first two rows of vector $\boldsymbol{A}_{\mathrm{c}_k}$ in Eq. (3.1)) is the contact force acting on the k-th end-effector and the last three rows of $\boldsymbol{F}$ are the contact force and moment acting on the target. In order to simplify the design of the end-effector, it could be desirable to avoid placing a force sensor on the contact plate. This implies not to have the contact force measurement available. On account of this, the approximation $\boldsymbol{F}_{\mathrm{c}_k} \simeq -\boldsymbol{F}_{\mathrm{el}_k}$ is made meaning the contact force is assumed to be roughly equal to the one measured by the sensor placed at the end tip of the last link (see Fig. 3.3). Furthermore, the last components of vector $\boldsymbol{F}$, i.e. $[-(\boldsymbol{F}_{\mathrm{c}_1} + \boldsymbol{F}_{\mathrm{c}_2})^{\mathrm{T}}, m_{\mathrm{ct}}]^{\mathrm{T}}$, can be assumed to be null in vector $\boldsymbol{F}'$ since it can be demonstrated that the product $\mathbf{B}_k^{+}\mathbf{J}^{\mathrm{T}}\boldsymbol{F}$, $k = 1, 2, 3$ associated to these components is always null. The previous considerations justify vector $\boldsymbol{F}'$ taking the place of vector $\boldsymbol{F}$ in Eqs. (3.10)-(3.12). It has to be noticed that in vector $\boldsymbol{F}$ no external actions other than contact ones are assumed to be present.

From Eqs. (3.10)-(3.12) it can be noticed that the control vectors are, in general, dynamically coupled among each other. However, in this control architecture, this is not true given the form of the $\mathbf{B}_k$, $k = 1, 2, 3$ matrices appearing in Eq. (3.9). In fact, it occurs that $\mathbf{B}_k\mathbf{B}_p^{+}$, $k, p = 1, 2, 3$; $p \neq k$. This is due to the fact each part of the control architecture (i.e. the two Impedance Controls and the PD Control) involves separate control actions, i.e. each control action is not involved in different controls at the same time.

This leads to the final control actions vectors:

$$\begin{aligned}\boldsymbol{u}_1 = \mathbf{B}_1^{+}\{&\mathbf{J}^{\mathrm{T}}\mathbf{M}\mathbf{J}(\mathbf{M}_{\mathrm{i}_1}\mathbf{J}_{\mathrm{ll}_1})^{+}[-\mathbf{M}_{\mathrm{i}_1}\dot{\mathbf{J}}_{\mathrm{ll}_1}\dot{\boldsymbol{Q}} - \mathbf{D}_{\mathrm{i}_1}(\dot{\boldsymbol{X}}_{\mathrm{ll}_1} - \dot{\boldsymbol{X}}_{\mathrm{ll}_{1_{\mathrm{des}}}}) - \mathbf{K}_{\mathrm{i}_1}(\boldsymbol{X}_{\mathrm{ll}_1} - \boldsymbol{X}_{\mathrm{ll}_{1_{\mathrm{des}}}}) + \\ &- \boldsymbol{A}_{\mathrm{el}_1}] + \mathbf{J}^{\mathrm{T}}\mathbf{M}\dot{\mathbf{J}}\dot{\boldsymbol{Q}} - \mathbf{J}^{\mathrm{T}}\boldsymbol{C} - \mathbf{J}^{\mathrm{T}}\boldsymbol{F}'\}\end{aligned} \tag{3.15}$$

$$\begin{aligned}\boldsymbol{u}_2 = \mathbf{B}_2^{+}\{&\mathbf{J}^{\mathrm{T}}\mathbf{M}\mathbf{J}(\mathbf{M}_{\mathrm{i}_2}\mathbf{J}_{\mathrm{ll}_2})^{+}[-\mathbf{M}_{\mathrm{i}_2}\dot{\mathbf{J}}_{\mathrm{ll}_2}\dot{\boldsymbol{Q}} - \mathbf{D}_{\mathrm{i}_2}(\dot{\boldsymbol{X}}_{\mathrm{ll}_2} - \dot{\boldsymbol{X}}_{\mathrm{ll}_{2_{\mathrm{des}}}}) - \mathbf{K}_{\mathrm{i}_2}(\boldsymbol{X}_{\mathrm{ll}_2} - \boldsymbol{X}_{\mathrm{ll}_{2_{\mathrm{des}}}}) + \\ &- \boldsymbol{A}_{\mathrm{el}_2}] + \mathbf{J}^{\mathrm{T}}\mathbf{M}\dot{\mathbf{J}}\dot{\boldsymbol{Q}} - \mathbf{J}^{\mathrm{T}}\boldsymbol{C} - \mathbf{J}^{\mathrm{T}}\boldsymbol{F}'\}\end{aligned} \tag{3.16}$$

$$\begin{aligned}\boldsymbol{u}_3 = \mathbf{B}_3^{+}\{&\mathbf{J}^{\mathrm{T}}\mathbf{M}\mathbf{J}\mathbf{J}_{\mathrm{B}}^{+}[-\mathbf{K}_{\mathrm{p}}(\boldsymbol{X}_{\mathrm{B}} - \boldsymbol{X}_{\mathrm{B}_{\mathrm{des}}}) - \mathbf{K}_{\mathrm{d}}(\dot{\boldsymbol{X}}_{\mathrm{B}} - \dot{\boldsymbol{X}}_{\mathrm{B}_{\mathrm{des}}})] + \mathbf{J}^{\mathrm{T}}\mathbf{M}\dot{\mathbf{J}}\dot{\boldsymbol{Q}} + \\ &- \mathbf{J}^{\mathrm{T}}\boldsymbol{C} - \mathbf{J}^{\mathrm{T}}\boldsymbol{F}'\}\end{aligned} \tag{3.17}$$

In the following, the overall control strategy will be referred to as Impedance+PD Control.

3.3.2 Direct PD Control for a space manipulator

Besides Impedance+PD Control, a conventional control like, for example, a simple PD Control applied directly on the arm joint torques and on the base position and attitude control actions, is considered (in the following it will be referred to as Direct PD Control). The control vectors will in this case be given by:

$$\boldsymbol{u}_1 = -\mathbf{K}_{\mathrm{p}_1}(\boldsymbol{\theta}_{\mathrm{J}_1} - \boldsymbol{\theta}_{\mathrm{J}_{1_{\mathrm{des}}}}) - \mathbf{K}_{\mathrm{d}_1}(\dot{\boldsymbol{\theta}}_{\mathrm{J}_1} - \dot{\boldsymbol{\theta}}_{\mathrm{J}_{1_{\mathrm{des}}}}) \tag{3.18}$$

$$\boldsymbol{u}_2 = -\mathbf{K}_{\mathrm{p}_2}(\boldsymbol{\theta}_{\mathrm{J}_2} - \boldsymbol{\theta}_{\mathrm{J}_{2_{\mathrm{des}}}}) - \mathbf{K}_{\mathrm{d}_2}(\dot{\boldsymbol{\theta}}_{\mathrm{J}_2} - \dot{\boldsymbol{\theta}}_{\mathrm{J}_{2_{\mathrm{des}}}}) \tag{3.19}$$

$$\boldsymbol{u}_3 = -\mathbf{K}_{\mathrm{p}_3}(\boldsymbol{X}_{\mathrm{B}} - \boldsymbol{X}_{\mathrm{B}_{\mathrm{des}}}) - \mathbf{K}_{\mathrm{d}_3}(\dot{\boldsymbol{X}}_{\mathrm{B}} - \dot{\boldsymbol{X}}_{\mathrm{B}_{\mathrm{des}}}) \tag{3.20}$$

where $\boldsymbol{\theta}_{\mathrm{J}_k} \in \mathbb{R}^{n_{l_k}\times 1}$, $k = 1, 2$ is the joint angles vector of the k-th arm, $\boldsymbol{\theta}_{\mathrm{J}_{k_{\mathrm{des}}}} \in \mathbb{R}^{n_{l_k}\times 1}$, $k = 1, 2$ is its desired value, $\boldsymbol{X}_{\mathrm{B}} \in \mathbb{R}^{3\times 1}$ is the vector containing the base position and attitude variables, $\boldsymbol{X}_{\mathrm{B}_{\mathrm{des}}} \in \mathbb{R}^{3\times 1}$ is its desired value and $\mathbf{K}_{\mathrm{p}_j} \in \mathbb{R}^{3\times 3}$, $j = 1, 2, 3$, $\mathbf{K}_{\mathrm{d}_j} \in \mathbb{R}^{3\times 3}$, $j = 1, 2, 3$ are respectively the control proportional and derivative gain matrices.

The Direct PD Control gains are selected as $\mathbf{K}_{\mathrm{p}_k} = k_{\mathrm{i}_k}\mathbf{I}^{n_{l_k}\times n_{l_k}}$, $k = 1, 2$, $\mathbf{K}_{\mathrm{d}_k} = d_{\mathrm{i}_k}\mathbf{I}^{n_{l_k}\times n_{l_k}}$, $k = 1, 2$, $\mathbf{K}_{\mathrm{p}_3} = \mathbf{K}_{\mathrm{p}}$ and $\mathbf{K}_{\mathrm{d}_3} = \mathbf{K}_{\mathrm{d}}$. This choice is made in order to make a comparison between the two control architectures (i.e. the Direct PD and the Impedance+PD Controls) by taking the same control gains into account.

3.3.3 Numerical approach for the selected case study

In the previous section, the Impedance-based Control for a 2D space manipulator to capture a non-cooperative target satellite has been developed and detailed. Of course, the control algorithms must be tested and their robustness verified numerically and/or experimentally.

It is worth noting that, by means of numerical simulations, it is possible to perform, in general, a complete analysis considering the effects of the mass and inertia properties and of the forcing terms and perturbations, if any, all along the studied maneuver. The ideal case study is the one in which the dynamics and the control are based on the same model. In this case, the whole simulation can be conducted in a single environment as, for example, Matlab. On the other hand, if one wants to take more realistic models for the system dynamics into consideration, one can resort to different simulation approaches. The accurate simulation, for example, of the contact dynamics already available in commercial software suggests leaving aside the development of in-house dedicated numerical codes.

On the other hand, commercial codes oriented to multi-body dynamics should allow the inclusion of in-house routines for simulating phenomena which are not included in their standard libraries (i.e. orbital dynamics, space environment actions, control schemes, thrusters, attitude control actuators, sensors, etc.). As a result, the choice adopted in this study is to use a state of the art-commercial multi-body code (i.e. MSC Adams) in co-simulation with an Impedance+PD Control scheme developed in the Simulink environment. This allows to simulate in detail the kinematics and dynamics of the space robot and target satellite and, of course, the contact dynamic phase. Fig.3.4 shows a block diagram of the co-simulation logic used

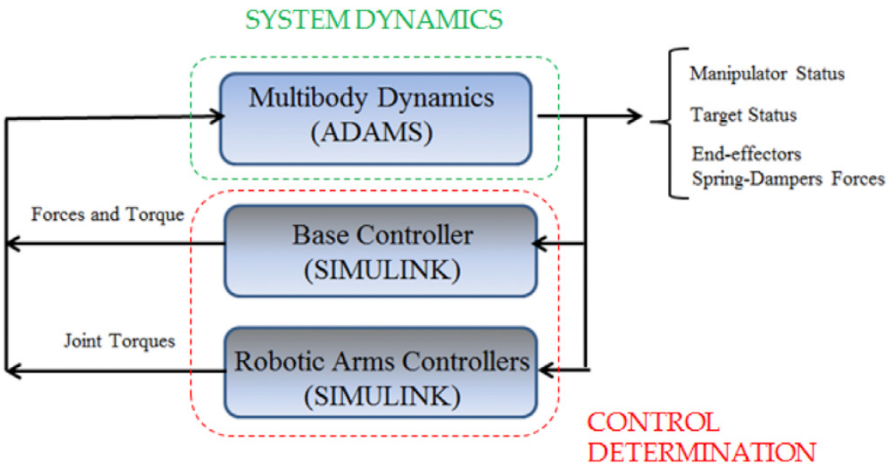

Figure 3.4. Co-simulation logic block diagram.

for the simulations. The *s-function* block connecting the Simulink environment with the Adams software is on the top. Within this approach, the inputs to the dynamic plant (i.e. the joint control torques, the position and attitude control actions applied to the spacecraft and, eventually, environmental actions) are evaluated by means of Matlab functions and passed, at each integration time-step, to the Adams solver. The outputs of the dynamics (i.e. the system state vector and other quantities like, for example, the spring-damper forces) are used to evaluate the control actions thus closing the loop. Details on the adopted co-simulation approach can be found in [77].

It is important to underline the Kane-like model is the core for the synthesis of the Impedance+PD Control used in the co-simulation approach.

3.4 Numerical results

As mentioned above, the goal of this chapter is to study the dynamic interaction of a space manipulator and a non-cooperative target orbiting nearby. In particular, the attention is focused on the contact and post-contact (pre-grasping) phases.

As initial conditions, the arm of the SMS are already deployed and the end-effectors are very close to the target satellite. The SMS is at rest, with its center of mass aligned along the x inertial axis with the target center of mass. For what concerns the target, the translational velocity components with respect to the inertial reference frame are assumed as $V_{x_0} = -5\,\text{cm/s}$ and $V_{y_0} = 0$ (the positive directions of the inertial axes are shown in Fig. 3.3); it also has an angular velocity about its center of mass of $\omega_{z_0} = 1\,\text{deg/s}$. As far as the desired values of the state variables appearing in Eqs. (3.15)-(3.20) - i.e. translational and angular positions and velocities of the base and the arms - are concerned, they are assumed to be equal to those of the initial conditions.

In all the following simulations, a duration time of the maneuver equal to 60 s has been considered. After this time interval, a new phase of the mission is supposed to take place where the grasping of the target with the use of mechanical grippers or robotic hands is involved.

3.4.1 Control strategies effectiveness evaluation

The effectiveness of a control strategy in a pre-grasping operation can be positively evaluated when some requirements on the kinematic and dynamic state of the SMS and target are satisfied (the adopted threshold values are reported in parentheses):

1. The magnitude of the contact forces is sufficiently small ($\leq 1\,\text{N}$);
2. During the maneuver, the distances between the end-effectors and the target are null or within a prescribed tolerance (of the order of centimeters);
3. During the maneuver, the SMS base shows relatively small translational displacements magnitude and angular displacements (respectively $\leq 5\,\text{cm}$ and $\leq 2\,\text{deg}$);
4. The target translational velocity magnitude and angular velocity are smaller than prescribed design ones (respectively $\leq 0.5\,\text{cm/s}$ and $\leq 0.05\,\text{deg/s}$);
5. Conditions 1 and 4 are maintained for a prescribed time interval (of the order of 10 s).

3.4.2 Control gains selection procedure

In all the following numerical simulations, the values of the Impedance Control gains are chosen as follows:

$$\begin{aligned} m_{\mathrm{i}_k} &= 5, \quad k = 1, 2 \\ d_{\mathrm{i}_k} &= 100, \quad k = 1, 2 \\ k_{\mathrm{i}_k} &= 0, \quad k = 1, 2 \end{aligned} \tag{3.21}$$

The choice of setting k_{i_k} equal to zero is made in order to avoid a potential "spring-effect" behavior on both the end-effectors which could produce an unwanted early detachment of the target.

SMS base PD Control gains parametric analysis

For what concerns the SMS base PD Control, the gains which will be considered as parameters are the proportional and derivative gains for the translational motion ($K_{\mathrm{p_T}}$ and $K_{\mathrm{d_T}}$ respectively) and the proportional and derivative gains for the rotational one ($K_{\mathrm{p_R}}$ and $K_{\mathrm{d_R}}$ respectively). This implies that the gain matrices in Eq. (3.6) are given by

$$\mathbf{K}_{\mathrm{p}} = \begin{bmatrix} K_{\mathrm{p_T}} & 0 & 0 \\ 0 & K_{\mathrm{p_T}} & 0 \\ 0 & 0 & K_{\mathrm{p_R}} \end{bmatrix}, \quad \mathbf{K}_{\mathrm{p}} = \begin{bmatrix} K_{\mathrm{d_T}} & 0 & 0 \\ 0 & K_{\mathrm{d_T}} & 0 \\ 0 & 0 & K_{\mathrm{d_R}} \end{bmatrix}$$

Furthermore, an additional constraint between the gains in the two sets has been introduced, namely that of critical damping conditions. From the mathematical standpoint, this is given by

$$\zeta_{\mathrm{T}} = \frac{K_{\mathrm{d_T}}}{2\sqrt{K_{\mathrm{p_T}} m_B}} = 1, \quad \zeta_{\mathrm{R}} = \frac{K_{\mathrm{d_R}}}{2\sqrt{K_{\mathrm{p_R}} J_B}} = 1 \tag{3.22}$$

This allows one to reduce the number of independent parameters from four to two; in particular, here the proportional gains are obtained once the derivative ones are set:

$$K_{\mathrm{p_T}} = \frac{K_{\mathrm{d_T}}^2}{4 m_B}, \quad K_{\mathrm{p_R}} = \frac{K_{\mathrm{d_R}}^2}{4 J_B}$$

In order to take the different variables of interest into account when evaluating the "best" control gains set, a Cost Function is defined as the following:

$$J = P_1 e_{\mathrm{T}} + P_2 e_{\mathrm{R}} + P_3 u_{\mathrm{T}} + P_4 u_{\mathrm{R}} + P_5 e_{\mathrm{J}} \tag{3.23}$$

where P_i, $i = 1, \ldots, 5$ are properly chosen weighting parameters such that $P_i = P_{i_1} P_{i_2}$ where P_{i_1} are non-dimensionalization parameters and P_{i_2} are the effective weights which are used to establish the relevance that wants to be assigned to the term they multiply. Namely, the latter are assumed as $P_{1_2} = P_{2_2} = 1$, $P_{3_2} = P_{4_2} = P_{5_2} = 10$ (this choice was made in order for the different terms present on the right-hand side of Eq. (3.23) to be of the same order of magnitude). The other quantities appearing in the above relation are given by:

$$\begin{aligned}
e_{\mathrm{T}} &= \max \sqrt{e_{\mathrm{T}_x}^2 + e_{\mathrm{T}_y}^2} \\
e_{\mathrm{R}} &= \max |e_{\mathrm{R}_z}| \\
u_{\mathrm{T}} &= \mathrm{mean}\, |u_{\mathrm{T}_x}| + \mathrm{mean}\, |u_{\mathrm{T}_y}| \\
u_{\mathrm{R}} &= \mathrm{mean}\, |u_{\mathrm{R}_z}| \\
u_{\mathrm{J}} &= \sum_{k=1}^{n_{l_1}+n_{l_2}} \mathrm{mean}\, |u_{\mathrm{J}_{z_k}}|
\end{aligned}$$

where e_{T_x} is the x inertial component of the SMS base center of mass position deviation from the desired one, e_{T_y} is the y inertial component of the same entity, e_{R_z} is the deviation of the SMS base attitude angle with respect to the x inertial axis from the desired one, u_{T_x} is the control force (along the base x body axis) acting on the SMS base, u_{T_y} is the y body component of the same quantity, u_{R_z} is the control torque (about the base z body axis) acting on the SMS base and $u_{\mathrm{J}_{z_k}}$ is the control torque (about the joint z axis) acting at the k-th joint.

All the tested combinations between the translational and rotational derivative gains values (together with the corresponding proportional gains) satisfy the mission requirements.

The "best" set of gains is chosen as the one that minimizes the above defined cost function. Fig. 3.5 shows a plot of the values assumed by the latter where the presence of a central plateau region can be detected. In particular, the minimum is found for $K_{\mathrm{d_T}} = 10$ (with a corresponding $K_{\mathrm{p_T}} = 0.05$) and $K_{\mathrm{d_R}} = 40$ (with a corresponding $K_{\mathrm{p_R}} = 4.8$) which are used in the subsequent results.

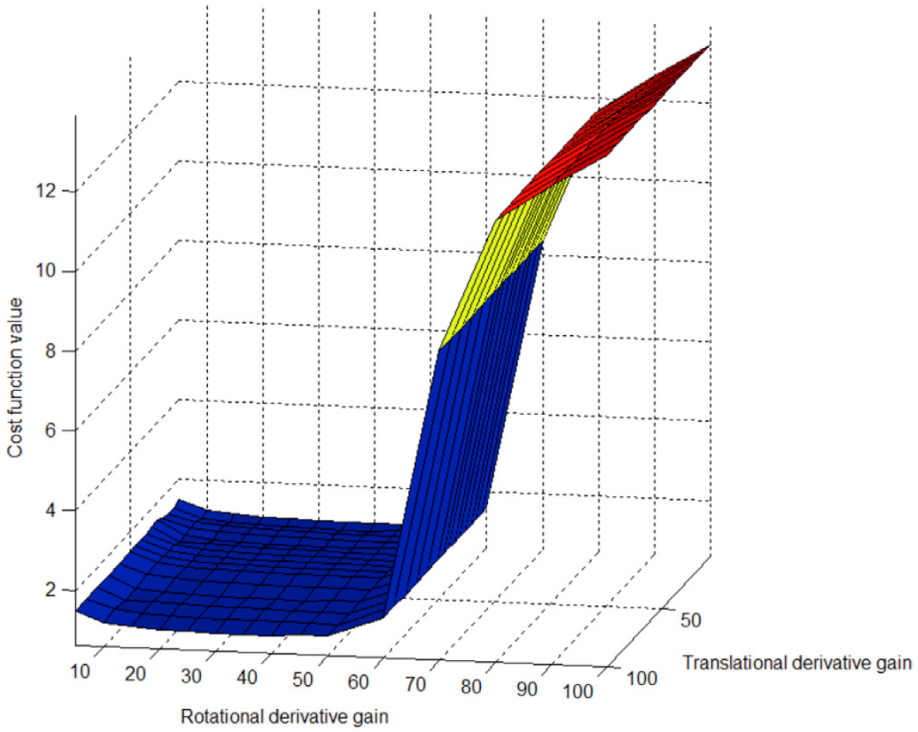

Figure 3.5. Cost function value vs. $K_{\mathrm{d_T}}$ and $K_{\mathrm{d_R}}$ variations.

3.4.3 Analysis of the Direct PD Control performance

In this section the performance of the Direct PD Control during the impact and post-impact phases is analyzed. In Fig.3.6 the sketch of the configurations assumed by the system during the maneuver is reported. It is evident that the base of the chaser is not maintained fixed both in translation and rotation after the first contact and the controller fails in accomplishing the mission within 60 s. In Fig.3.7 the magnitude of the contact forces between the end-effectors and the target satellite are shown. It is interesting to observe that, as far as arm 1 is concerned, the first impact takes place after a few seconds (as clearly visible from the sharp variation on the value of the contact force) and afterwards a rebound between the end-effector and the target occurs, but towards the end of the maneuver the two bodies are still in contact as can be deduced from the non-null contact force values. Looking at the dynamics of arm 2, it loses contact with the target soon after the first impact (zero value of contact force). For a better understanding of the dynamics of the target, its translational velocity magnitude and angular velocity are reported in Figs. 3.8 and 3.9 respectively. It is worth noting that at the prescribed final time the translational and angular velocities of the target are not damped out. We can

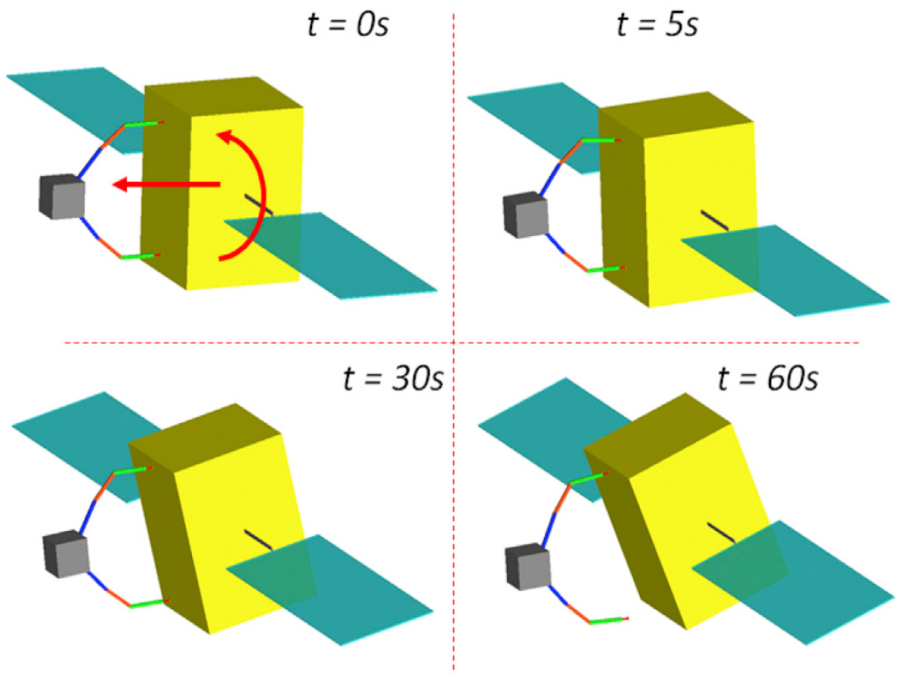

Figure 3.6. Sketch of the system dynamic evolution when Direct PD Control is applied.

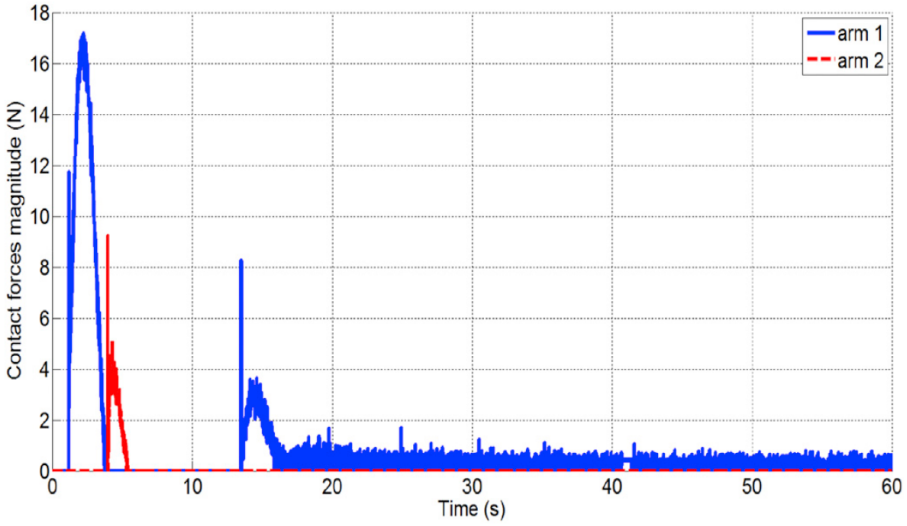

Figure 3.7. Magnitude of the contact forces acting between the SMS end-effectors and the target.

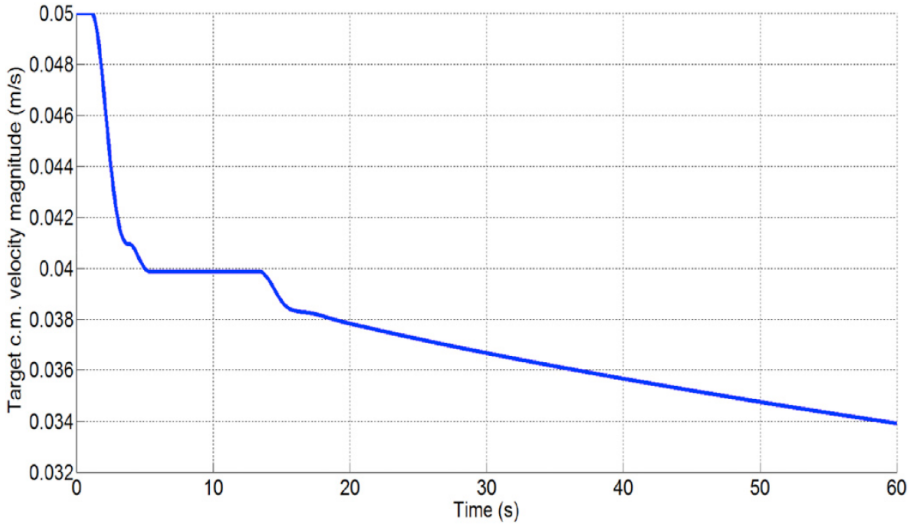

Figure 3.8. Target center of mass inertial velocity magnitude.

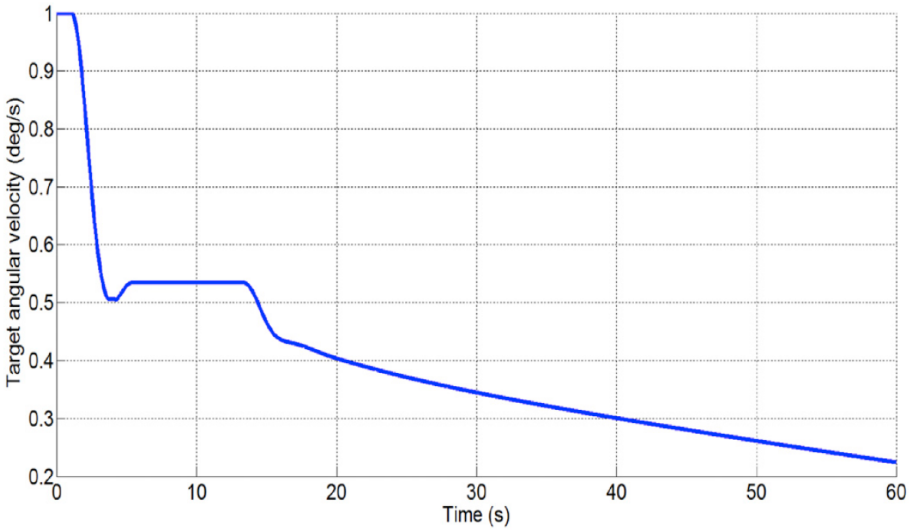

Figure 3.9. Target inertial angular velocity.

conclude that a simple Direct PD Control applied to a robotic manipulator is not suitable for a pre-grasping maneuver.

3.4.4 Analysis of the Impedance+PD Control performance and preliminary robustness analysis

In the present section, a detailed discussion on the Impedance+PD Control effectiveness is presented. Four different cases are analyzed:

1. case 0: the nominal case (nominal means the fact the control block uses the same bodies inertial parameters of the Adams dynamics block);
2. case 1: the controller overestimates the bodies inertial parameters by 10%;
3. case 2: the controller underestimates the bodies inertial parameters by 10%;
4. case 3: the controller underestimates the bodies inertial parameters by 10% and joint friction is added to the dynamics model (but not considered in the control synthesis).

Concerning case 3, a simple friction model has been adopted [78]:

$$\tau_{\mathrm{f}} = -\tau_{\mathrm{c}}\mathrm{sign}(\dot{\theta}_{\mathrm{J}}) - d\dot{\theta}_{\mathrm{J}} \tag{3.24}$$

where τ_{f} is the friction torque, τ_{c} and d are coefficients of constant and velocity-dependent friction torque respectively (assumed equal to $5\,\mathrm{N\,m}$ and $15\,\mathrm{N\,m\,s/rad}$ respectively) and $\dot{\theta}_{\mathrm{J}}$ represents the angular rate of the joint. In Fig.3.10 the configurations assumed by the SMS and target when the Impedance+PD Control algorithm is applied are shown. From Fig.3.10a (which refers to case 0) it is possible to observe that, at the end of the maneuver, both the end-effectors of the SMS remain very close to the target. From Fig.3.10b (which instead refers to case 3) it can be noticed that the arms configuration evolution is significantly different from that of the nominal case 0. However, at the end of the maneuver both the end-effectors are very close (even if slightly less than the nominal case 0) to the target despite the fact the control determination is based upon a model which presents some inaccuracies and neglects certain actions. The sketches for cases 1 and 2 are not reported for the sake of brevity since they are substantially the same as that of Fig.3.10a. In Figs.3.11 and 3.12 the time histories of the contact forces acting on the end-effectors of the two arms are reported for all the test cases, where it is possible to see that the first requirement is satisfied. It is interesting to observe that the first three cases show

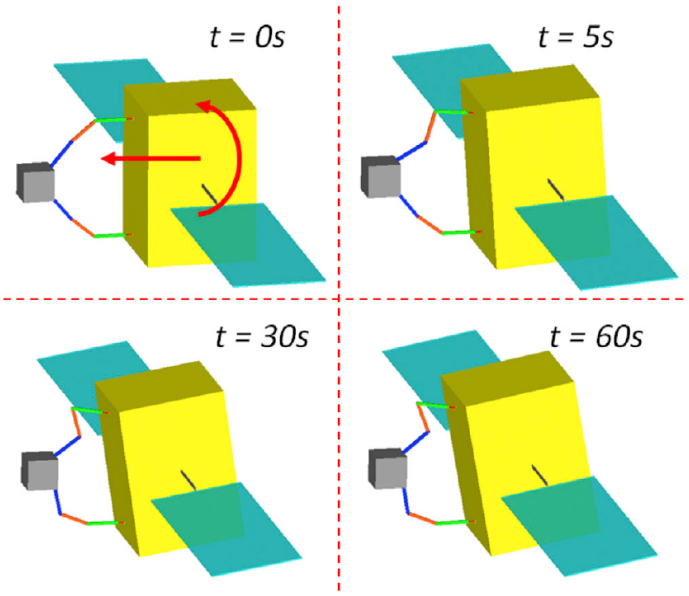

a. Nominal case (Case 0)

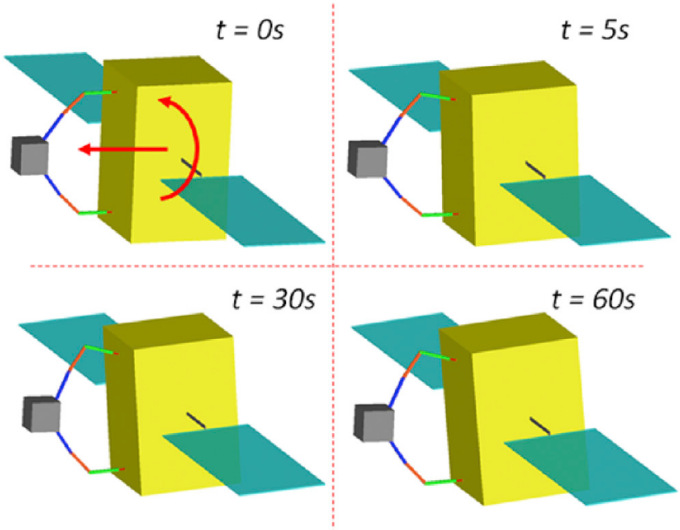

b. Underestimated inertial parameters and neglected joint friction (Case 3)

Figure 3.10. Sketch of the system dynamic evolution when Impedance+PD Control is applied.

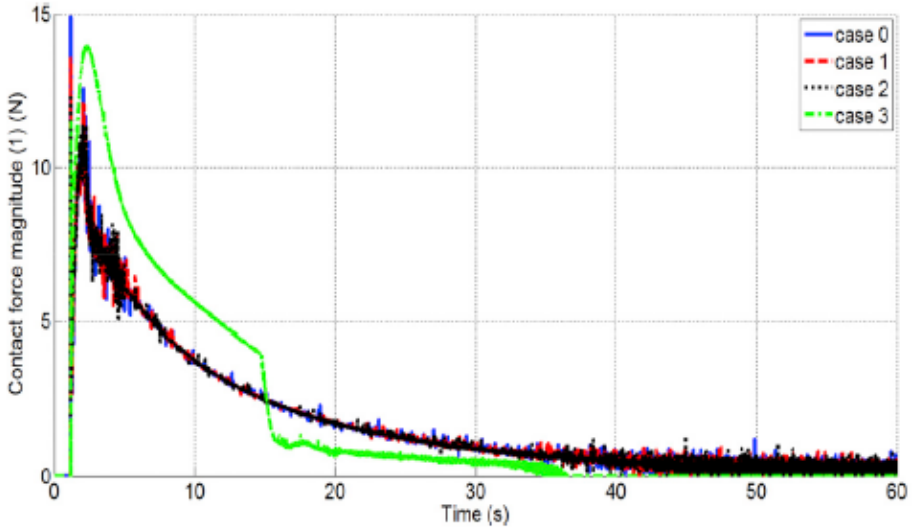

Figure 3.11. Magnitude of the contact force acting between the SMS arm 1 contact plate and the target.

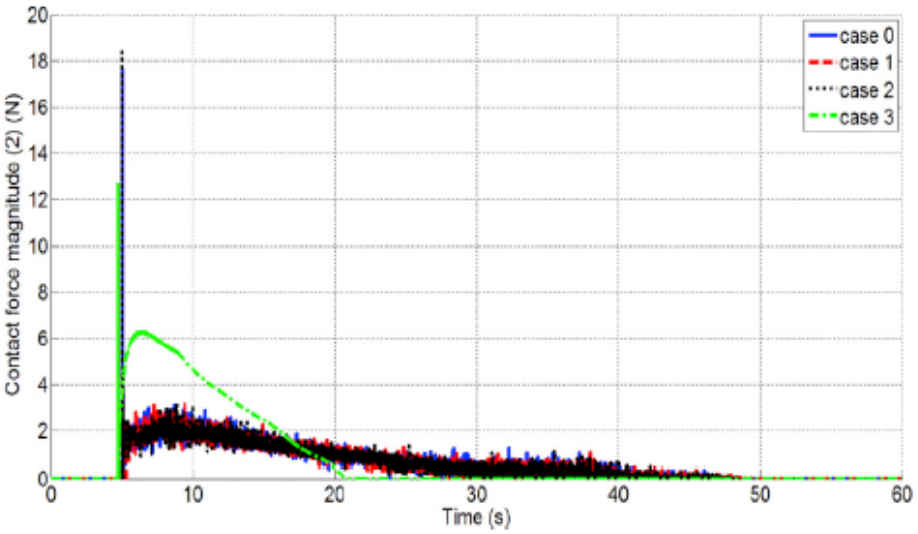

Figure 3.12. Magnitude of the contact force acting between the SMS arm 2 contact plate and the target.

values which are very close among each other, while the last one (case 3) presents a behavior which is remarkably different from the previous ones, especially in the initial transient phase.

As far as the second requirement (i.e. the distances between the end-effectors and the target are null or within a prescribed tolerance) is concerned, no graphs are reported. For the first arm, it is sufficient to say the small values of the contact force observed in the last phase of the simulation for the first three test cases are indicative of the continuity of contact. In case 3 the contact force magnitude reaches a constant zero value from roughly $t = 36\,\mathrm{s}$ on. This means the end-effector has actually lost contact, but looking at the values of the distance separating the end-effector contact plate from the target, it has been verified they were absolutely acceptable (of the order of centimeters). For the second arm, the simulation shows that for cases 0, 1 and 2 the contact force goes to zero at $t = 49\,\mathrm{s}$ roughly; this once again means the end-effector has actually lost contact, but the distance values are acceptable here too. In case 3 the contact force magnitude reaches a null value at $t = 21\,\mathrm{s}$ roughly; in this case though the distance separating the contact plate from the target bus has reached a limit value. Concerning the third requirement (i.e. the SMS base shows

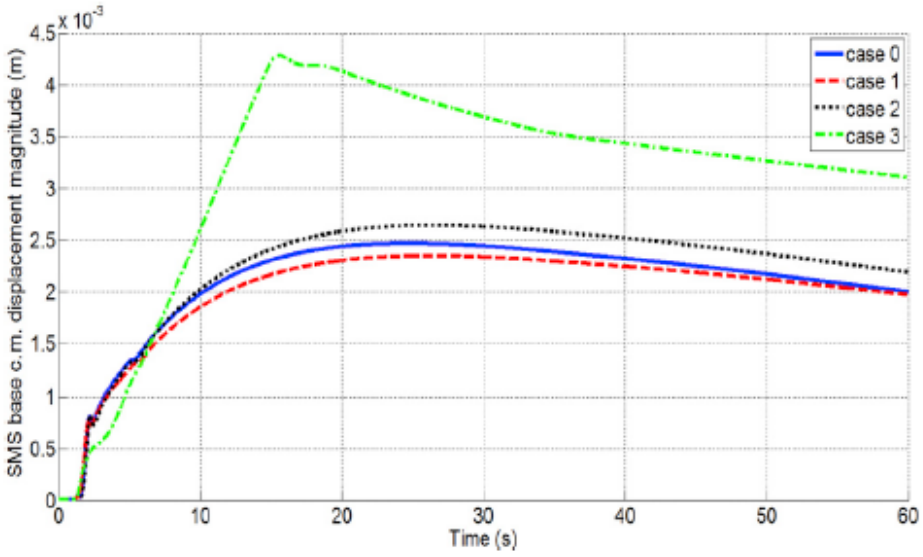

Figure 3.13. SMS base center of mass displacement magnitude.

relatively small linear and angular displacements), the displacement magnitude of the SMS base center of mass is shown in Fig. 3.13 for all cases. It is possible to appreciate the displacement is of the order of millimeters. The first three curves are qualitatively similar and it can be seen how the values are lower for case 1 and higher

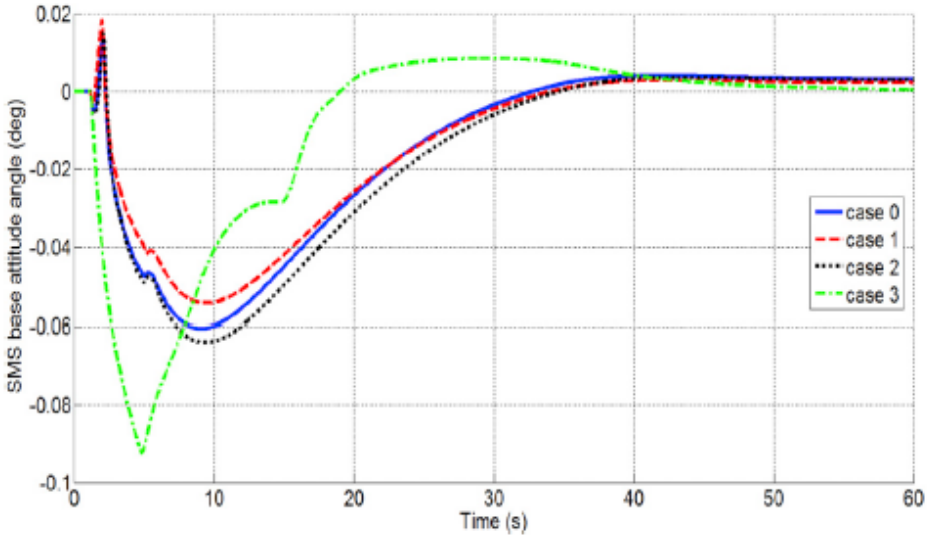

Figure 3.14. SMS base attitude angle with respect to the x inertial axis.

for case 2 with respect to the nominal case 0. For what concerns case 3, the curve is significantly different showing higher values for most of the mission duration. As far as the attitude of the SMS base is concerned, the relevant time histories are reported in Fig. 3.14. Indeed, we observe a very similar behaviour for the first three cases. On the contrary, for case 3 the base attitude angle presents lower values (in magnitude) for most of the mission duration. Anyway, the attitude variation magnitude is lower than 0.1 deg in all cases. The effect of the proportional contribution to the base control is clearly visible from the fact the attitude angle is going back to zero (which is the desired value) within a relatively short time. The above results allow to say the third requirement is also satisfied. To verify the fourth requirement (i.e. the target translational velocity magnitude and the angular velocity are respectively lower or equal to 0.5 cm/s and 0.05 deg/s), in Fig. 3.15 the magnitude of the target center of mass velocity is reported. Impedance+PD Control succeeds in slowing down the translational motion within the prescribed time interval. Furthermore, it is also able to perform a de-tumbling maneuver of the target as shown in Fig. 3.16 where the target angular velocity is reduced to a nearly-zero value in about 50 s. So it can be said the fourth requirement is satisfied as well. In these two figures it can be seen how the curves for cases from 0 to 2 are again practically coincident, while the curve for case 3 shows a noticeable deviation from the others.

As regards the fifth requirement, it can be said it is functional to the successive grasping phase in the sense the time interval could be, for example, the time necessary to the grippers to perform the grasping maneuver. From Figs. 3.11, 3.12, 3.15 and

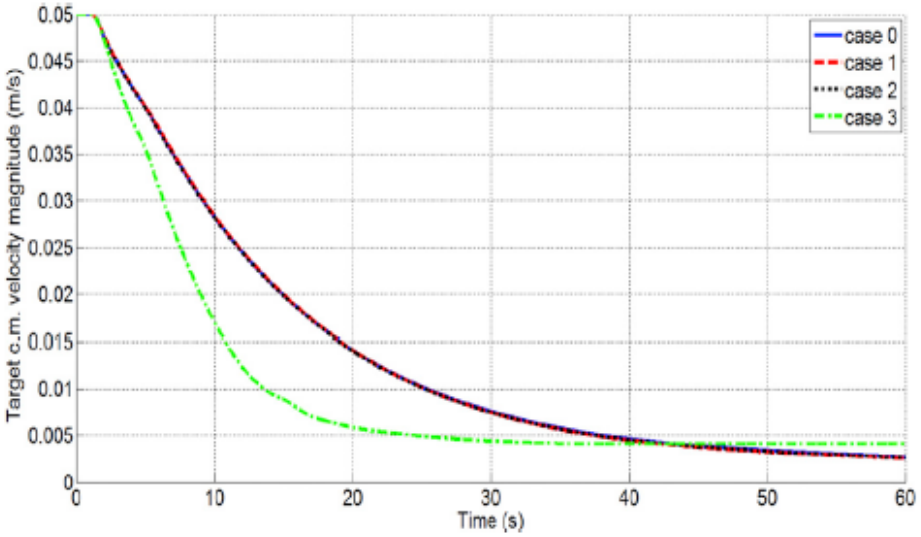

Figure 3.15. Target center of mass velocity magnitude.

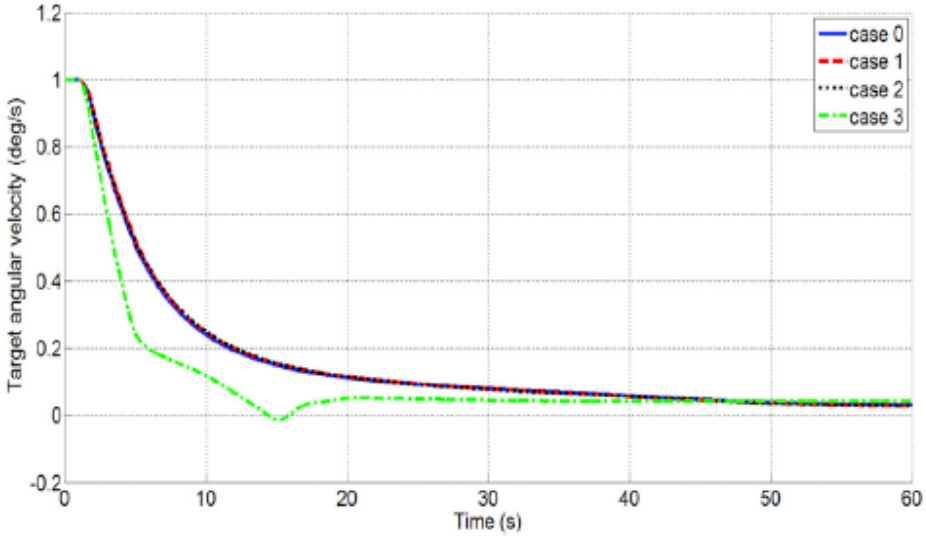

Figure 3.16. Target angular velocity.

3.16 it can be seen that requirements 1 and 4 are satisfied starting from $t = 50\,\mathrm{s}$. Consequently, $t = 50\,\mathrm{s}$ could be taken as the grasping maneuver beginning time instant. The performance and preliminary robustness analysis results discussed above

Table 3.2. Impedance+PD Control performance and preliminary robustness analysis results.

Requirement	CASE			
	0	1	2	3
Requirement 1	√	√	√	√
Requirement 2	√	√	√	×
Requirement 3	√	√	√	√
Requirement 4	√	√	√	√
Requirement 5	√	√	√	√

are summarized in Tab. 3.2 where the check and cross symbols indicate whether the requirement is satisfied or not respectively. It can be concluded that the proposed Impedance+PD Control is quite robust to uncertainties on the inertial parameters, while it is more sensitive to non-modeled dynamic phenomena as joint friction.

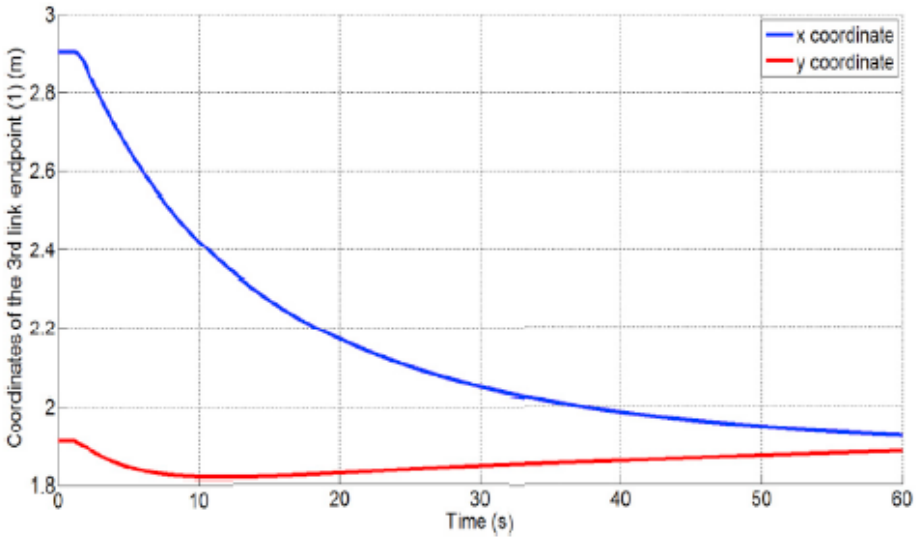

Figure 3.17. SMS arm 1 last link endpoint inertial coordinates (Case 0).

A comment on the choice of the gains used in the two Impedance Controls is due. In particular, it has been said the proportional gains were set to zero. It could be argued if, with this choice, the controlled variables remain close to their initial values (which are the desired ones). Indeed, this requirement is satisfied even when only the derivative contributions to the control are active, as shown, for example, in Figs. 3.17

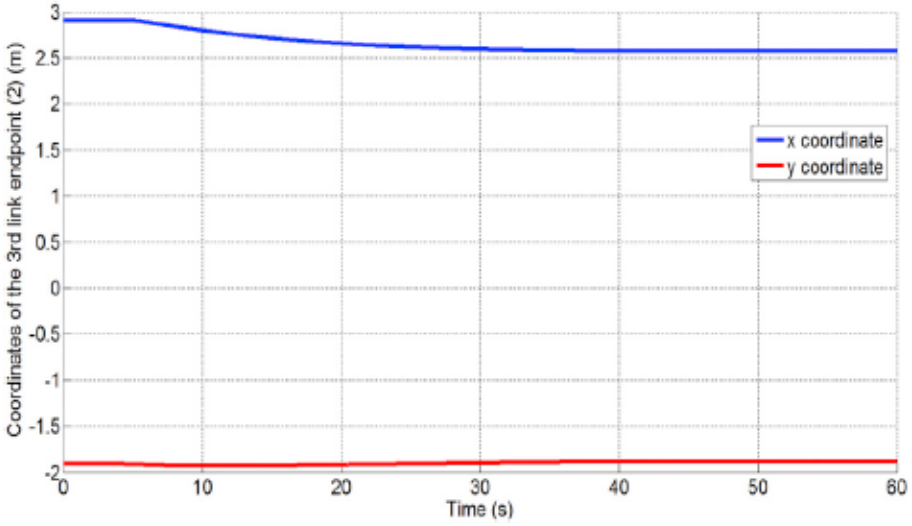

Figure 3.18. SMS arm 2 last link endpoint inertial coordinates (Case 0).

and 3.18 for the nominal case. In particular, it can be observed the variations on the last link endpoints positions are of the order of decimeters throughout the entire maneuver.

3.5 Impedance Control gains tuning procedure

After having selected the gains for the SMS base platform control (section 3.4.2), a tuning procedure for the robotic arms Impedance Control gains is now presented. First of all, the structure of the gain matrices is generalized by assuming different coefficients for the translational and rotational portions of the control and the constraint of null virtual stiffness control coefficient is removed. This mathematically translates into having the following form for the Impedance Control matrices:

$$\mathbf{M}_{\mathrm{i}_k} = \begin{bmatrix} m_{\mathrm{i}_{\mathrm{T}_k}} & 0 & 0 \\ 0 & m_{\mathrm{i}_{\mathrm{T}_k}} & 0 \\ 0 & 0 & m_{\mathrm{i}_{\mathrm{R}_k}} \end{bmatrix}, \ \mathbf{D}_{\mathrm{i}_k} = \begin{bmatrix} c_{\mathrm{i}_{\mathrm{T}_k}} & 0 & 0 \\ 0 & c_{\mathrm{i}_{\mathrm{T}_k}} & 0 \\ 0 & 0 & c_{\mathrm{i}_{\mathrm{R}_k}} \end{bmatrix}, \ \mathbf{K}_{\mathrm{i}_k} = \begin{bmatrix} k_{\mathrm{i}_{\mathrm{T}_k}} & 0 & 0 \\ 0 & k_{\mathrm{i}_{\mathrm{T}_k}} & 0 \\ 0 & 0 & k_{\mathrm{i}_{\mathrm{R}_k}} \end{bmatrix} \tag{3.25}$$

This allows for a higher operational flexibility in dealing with the target satellite initial kinematic conditions. Nevertheless, although this choice on one hand can lead to better performances of the control strategy, on the other poses the issue of carefully choosing adequate combinations of the mass, damping and stiffness parameters in order to avoid the “spring-effect” earlier described. In all the following

results, the values for the base PD Control are those obtained in Section 3.4.2. All

Table 3.3. Analyzed control gain parameters

m_{i_T}	c_{i_T}	k_{i_T}	m_{i_R}	c_{i_R}	k_{i_R}	$m_i : c_i : k_i$	Result
2.5	125	0.125	25	1250	1.25	1:50:0.05	√
2.5	125	0.625	25	1250	6.25	1:50:0.25	√
2.5	125	1.25	25	1250	12.5	1:50:0.5	√
2.5	125	1.875	25	1250	18.75	1:50:0.75	√
2.5	125	2.5	25	1250	25	1:50:1	×
2.5	125	3.125	25	1250	31.25	1:50:1.25	×
2.5	125	3.75	25	1250	37.5	1:50:1.5	×
10	**500**	**0.5**	**100**	**5000**	**5**	**1:50:0.05**	√
10	500	2.5	100	5000	25	1:50:0.25	√
10	500	5	100	5000	50	1:50:0.5	√
10	500	7.5	100	5000	75	1:50:0.75	√
10	500	10	100	5000	100	1:50:1	√
10	500	12.5	100	5000	125	1:50:1.25	√
10	500	15	100	5000	150	1:50:1.5	√
100	5000	5	1000	50000	50	1:50:0.05	√
100	5000	25	1000	50000	250	1:50:0.25	√
100	5000	50	1000	50000	500	1:50:0.5	√
100	5000	75	1000	50000	750	1:50:0.75	√
100	5000	100	1000	50000	1000	1:50:1	√
100	5000	125	1000	50000	1250	1:50:1.25	×
100	5000	150	1000	50000	1500	1:50:1.5	×
100	10000	5	1000	100000	50	1:100:0.05	×
100	10000	25	1000	100000	250	1:100:0.25	×
100	10000	50	1000	100000	500	1:100:0.5	×
100	10000	75	1000	100000	750	1:100:0.75	×
100	10000	100	1000	100000	1000	1:100:1	×
100	10000	125	1000	100000	1250	1:100:1.25	×
100	10000	150	1000	100000	1500	1:100:1.5	×
200	10000	10	2000	100000	100	1:50:0.05	×
200	10000	50	2000	100000	500	1:50:0.25	×
200	10000	100	2000	100000	1000	1:50:0.5	×
200	10000	150	2000	100000	1500	1:50:0.75	×
200	10000	200	2000	100000	2000	1:50:1	×
200	10000	250	2000	100000	2500	1:50:1.25	×
200	10000	300	2000	100000	3000	1:50:1.5	×

the tested gains combinations are reported in Tab. 3.3, where the check and cross symbols in the last column respectively indicate whether the mission requirements stated in Section 3.4.1 are satisfied or not. As it can be seen, there are many gains sets which satisfy the mission requirements. The cost function here used is defined

as:

$$J = P_1 e_{\mathrm{T}} + P_2 e_{\mathrm{R}} + P_3 u_{\mathrm{T}} + P_4 u_{\mathrm{R}} + P_5 e_{\mathrm{J}} + P_6 e_{\mathrm{T_t}} + P_7 e_{\mathrm{R_t}} \tag{3.26}$$

where the previously defined cost function (3.23) has been augmented to take the target kinematic state into account. The additional terms are given by

$$e_{\mathrm{T_t}} = \text{mean}\sqrt{v_{\mathrm{t}_x}^2 + v_{\mathrm{t}_y}^2}$$
$$e_{\mathrm{R_t}} = \text{mean}\,|\omega_{\mathrm{t}_z}|$$

where v_{t_x} and v_{t_y} are respectively the x and y inertial components of the target center of mass velocity and ω_{t_z} is the target angular velocity (about the z inertial axis). Furthermore, it has been set $P_{1_2} = P_{3_2} = P_{4_2} = P_{6_2} = P_{7_2} = 1$, $P_{2_2} = P_{5_2} = 10$ (once again to have terms of the same order of magnitude on the right-hand side of Eq. (3.26)). The "best" set of gains is chosen as the one which minimizes the above defined the above defined cost function; in particular, the minimum is found for the gains set highlighted in red in Tab. 3.3. In the following simulations the latter is used for the Impedance Control of both the last links.

3.5.1 Analysis of the Impedance+PD Control performance and applicability range evaluation

Impedance+PD Control performance analysis

Taking the Impedance Control gains evaluated in Section 3.5 into consideration, the performance of the control strategy is analyzed in the nominal scenario. In Fig.3.19 a sketch of the evolution of the system is reported. It is possible to observe how the developed strategy makes the chaser able to absorb the impact and that, at the end of the maneuver, both the end-effectors of the SMS remain very close to the target satellite. In Fig.3.20 the time history of the contact forces acting on the contact plates of the two end-effectors is also reported. The sharp variations in the two curves are indicative of the beginning of the contact phase between the bodies. It can be seen that for arm 1 the magnitude reaches a constant zero value from $t = 29.7\,\mathrm{s}$ on; an analogous thing happens for arm 2 starting from $t = 19.2\,\mathrm{s}$. This means both the end-effectors have actually lost contact with the target; nevertheless, it has been verified the distances dividing the contact plates from the target bus display values which are below the threshold given for requirement 2. These considerations allow to say the first two requirements are satisfied. In Figs.3.21 and 3.22 the magnitude of the SMS base center of mass displacement and the base attitude angle with respect

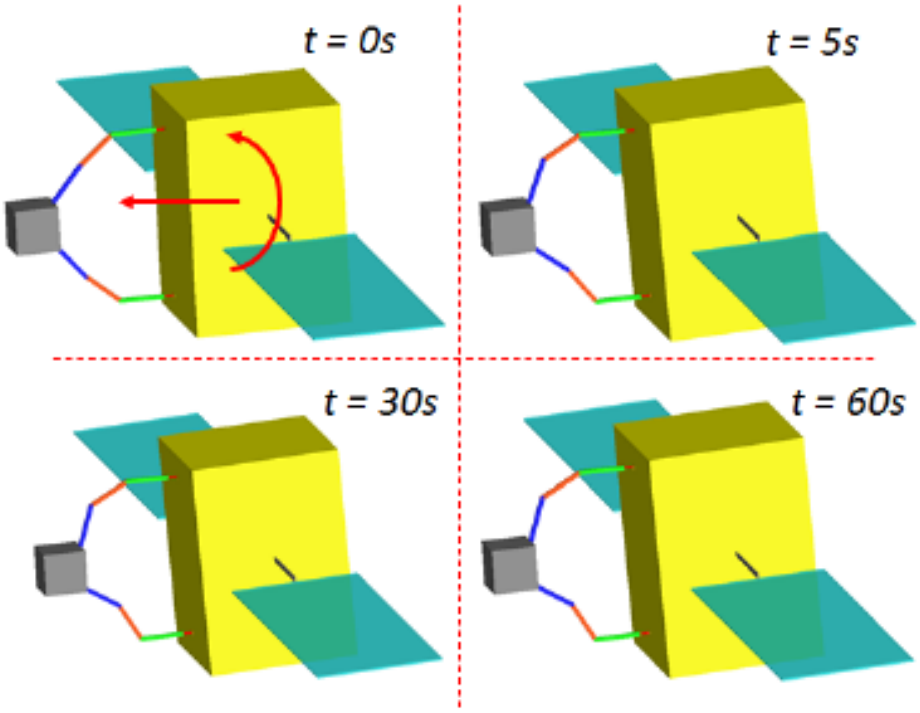

Figure 3.19. Sketch of the system dynamic evolution when Impedance+PD Control is applied (nominal case).

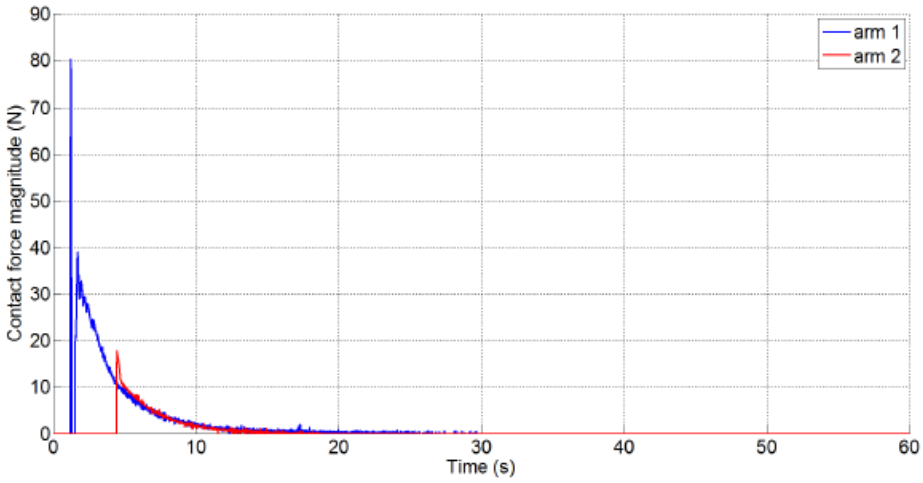

Figure 3.20. Magnitude of the contact forces acting between the SMS contact plates and the target (nominal case).

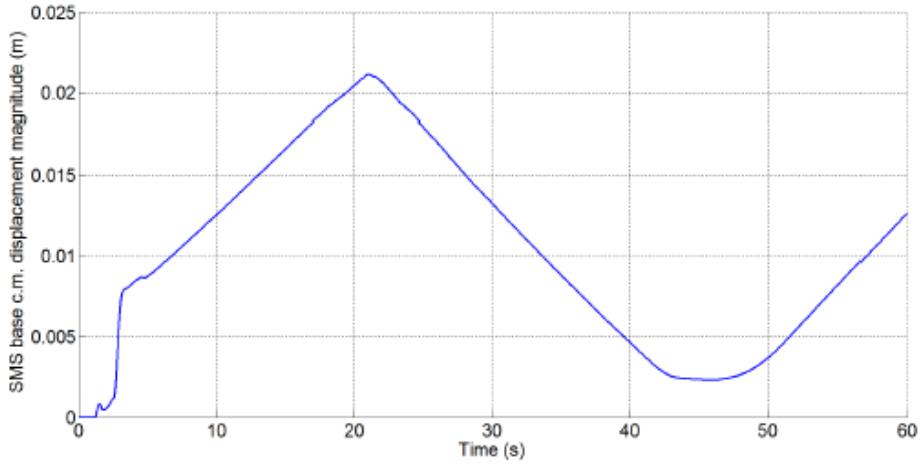

Figure 3.21. SMS base center of mass displacement magnitude (nominal case).

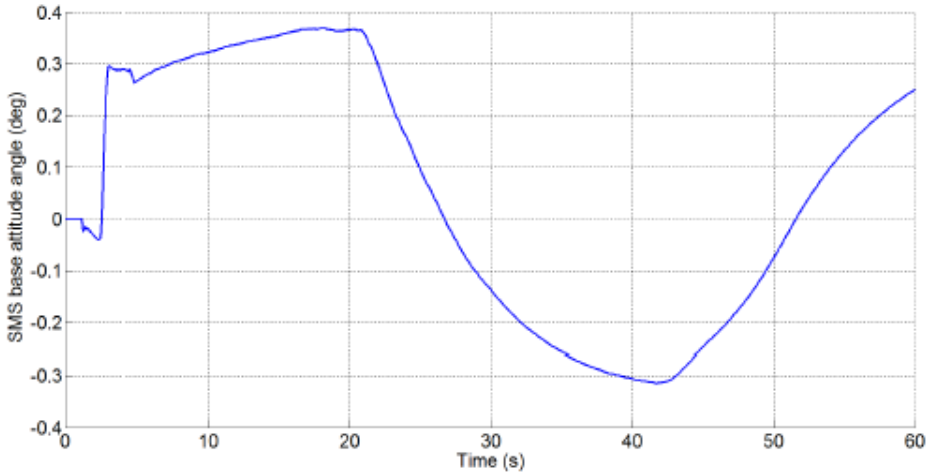

Figure 3.22. SMS base attitude angle with respect to the x inertial axis (nominal case).

to the x inertial axis are respectively reported. It can be noticed these two variables are well below the maximum allowed ones which implies the third requirement is satisfied as well. It is interesting to observe both the curves show a periodic-like behavior. The kinematic behavior of the target is shown in Figs. 3.23 and 3.24.

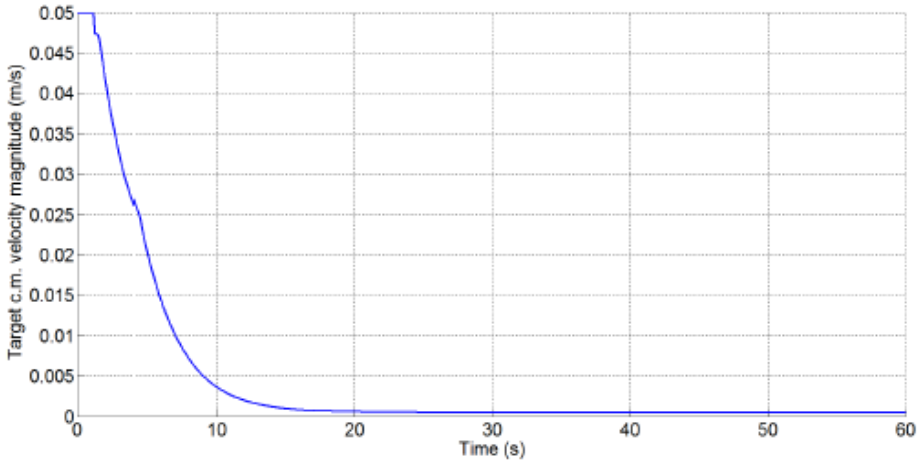

Figure 3.23. Target center of mass velocity magnitude (nominal case).

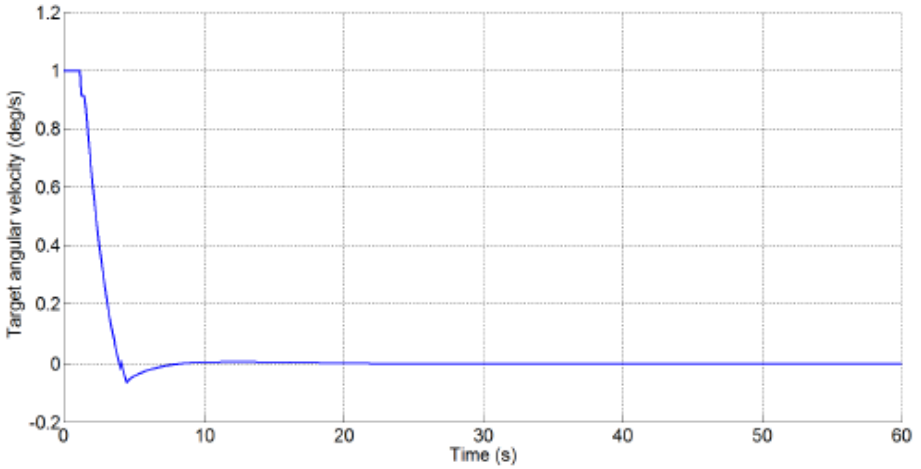

Figure 3.24. Target angular velocity (nominal case).

The target center of mass velocity magnitude is reduced to much less than a tenth of its initial value and the target angular velocity practically to zero. So requirement 4 is verified.

As far as the fifth requirement is concerned, from Figs. 3.20, 3.23 and 3.24 it can be seen requirements 1 and 4 are verified starting from $t = 20\,\mathrm{s}$ on. Consequently, the grasping operation could begin at any time instant following $t = 20\,\mathrm{s}$.

Impedance+PD Control applicability range evaluation

It could well happen in actual on-orbit missions that the initial kinematic conditions of the target satellite do not coincide with those considered in the nominal design. On account of this, it is interesting to evaluate the applicability range of the proposed Impedance+PD Control strategy given the optimal set of gains determined in the nominal conditions and varying the target satellite initial kinematic state. Tab.3.4 shows the results of this analysis where in the first column and first row the

Table 3.4. Impedance+PD Control applicability range evaluation.

	0.5	1	1.5	2	2.5	3
2.5	√	√	×	×	×	×
5	√	√	√	√	×	×
7.5	√	√	√	√	√	×
10	×	√	√	×	×	×
12.5	×	×	×	×	×	×

magnitude of the target center of mass initial velocity and the target initial angular velocity are respectively reported. The check and cross symbols respectively indicate the mission is either accomplished or not. Looking at the table, it is possible to notice how the selected gains set is actually able to face a good number of out-of-design conditions, ranging from 2.5 to 10 cm/s and from 0.5 to 2.5 deg/s. A relevant aspect that has been detected in this analysis - besides the values of the two variables taken separately - is their combination. In fact, it can be seen that high or low values for the target initial conditions could be sustainable or not according to the way they are reciprocally coupled.

In order to have a more quantitative idea of how the controller behaves in out-of-design conditions, in the following the results relative to the worst analyzed case (i.e. 12.5 cm/s - 3 deg/s) are shown. Figures from 3.25 to 3.30 show that requirement 1 is satisfied, but, on the other hand, requirements 2, 3, 4 and 5 are not. Nevertheless, the reported values of the SMS base attitude angle and the target angular velocity violate just slightly the imposed constraints and those of the SMS base center of mass displacement magnitude and the target center of mass velocity magnitude remain of the same order of magnitude of the maximum allowed ones.

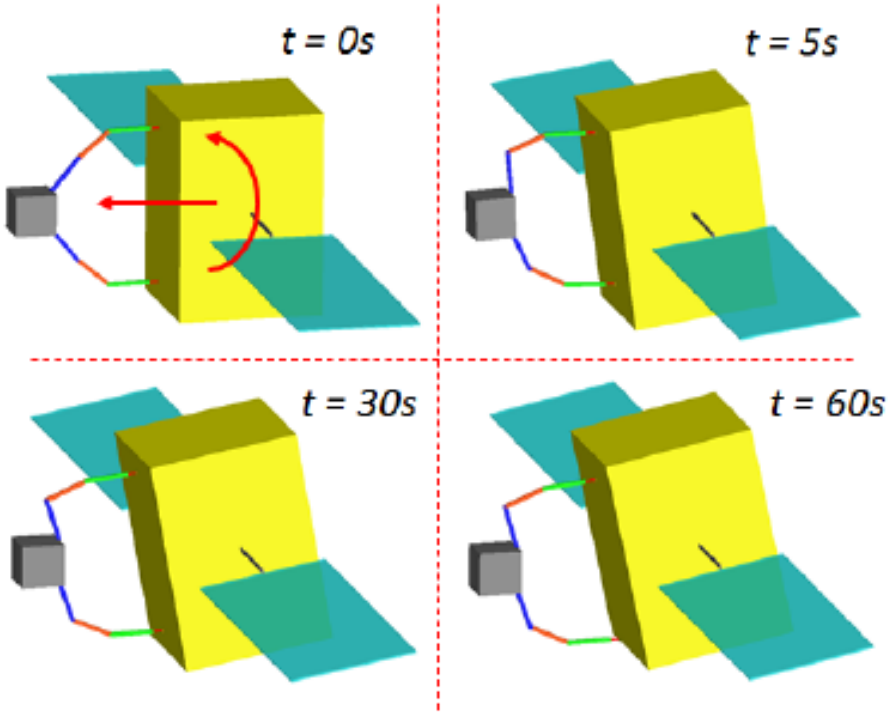

Figure 3.25. Sketch of the system dynamic evolution when Impedance+PD Control is applied (worst case).

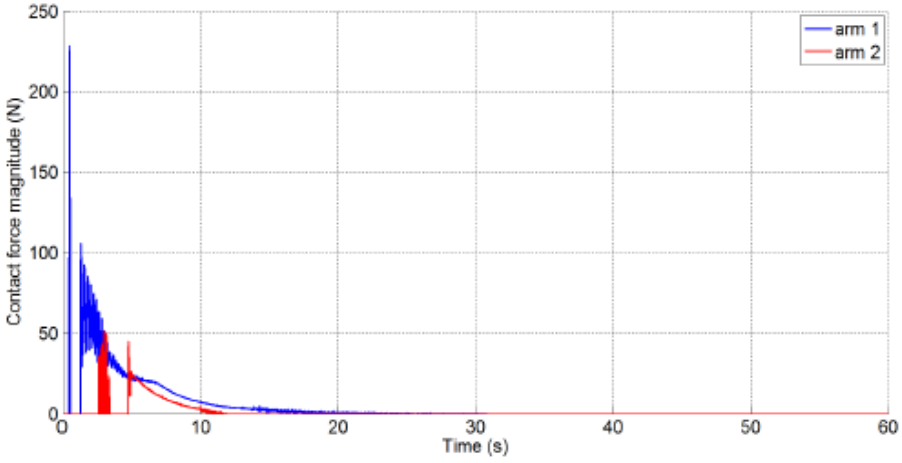

Figure 3.26. Magnitude of the contact forces acting between the SMS contact plates and the target (worst case).

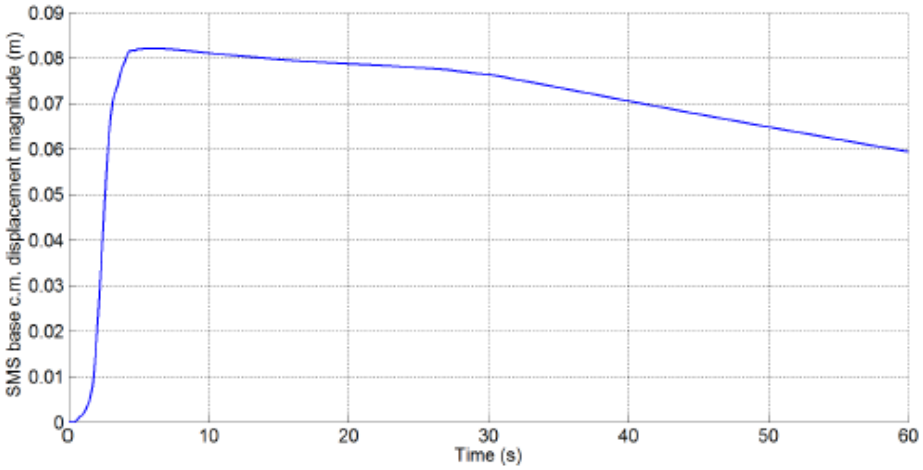

Figure 3.27. SMS base center of mass displacement magnitude (worst case).

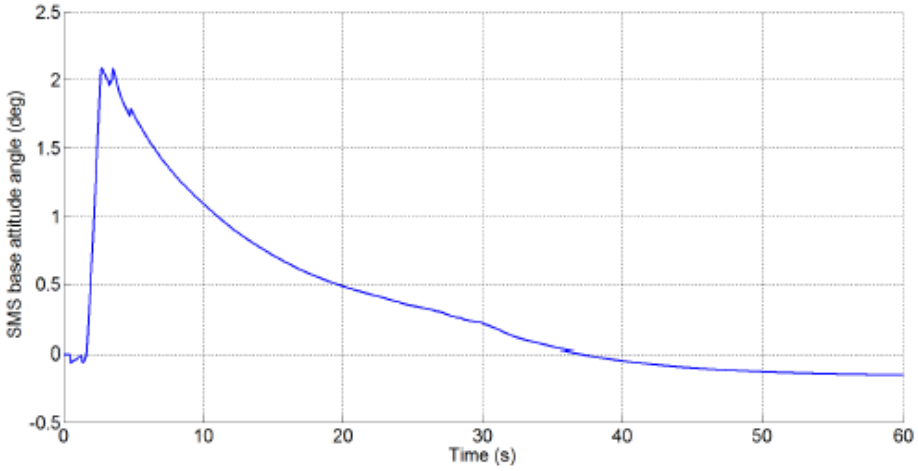

Figure 3.28. SMS base attitude angle with respect to the x inertial axis (worst case).

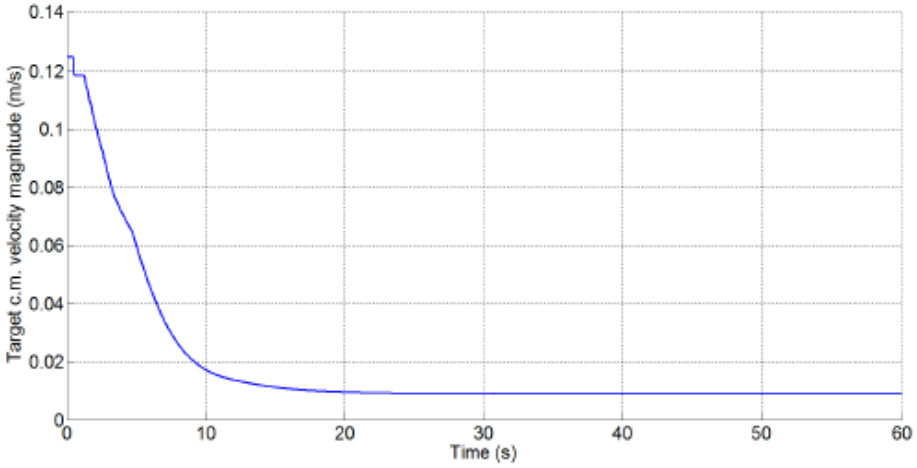

Figure 3.29. Target center of mass velocity magnitude (worst case).

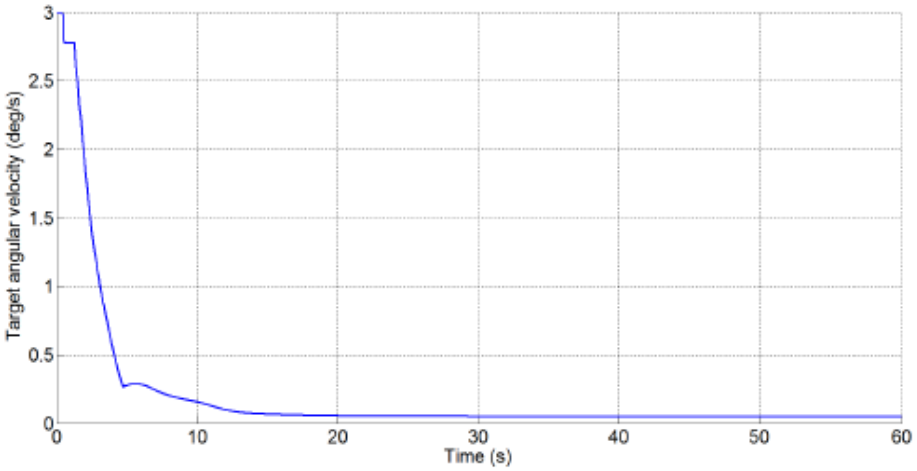

Figure 3.30. Target angular velocity (worst case).

3.6 Conclusions

In this chapter a Kane-like formulation for the kinematics and dynamics of a two-arm space manipulator system and a non-cooperative target satellite coming in contact has been presented. An Impedance+PD Control algorithm has been developed to allow contact keeping between the manipulator end-effectors and the target without performing a real grasp. The performance of the proposed control architecture has been evaluated by means of a co-simulation methodology involving the commercial multi-body code MSC Adams and Simulink. Furthermore, a preliminary robustness analysis was conducted considering uncertainties on the bodies inertial parameters and neglecting joint friction in the control synthesis. The obtained results allow to say the developed control strategy is suitable for application in a pre-grasping maneuver satisfying the user-defined requirements and also showing a preliminary good level of robustness. The performance of Impedance+PD Control was also compared to that of a Direct PD Control showing the former is able to accomplish the mission requirements while the latter fails. As far as the choice of the gains for the PD Control of the base platform is concerned, a parametric analysis has been conducted. In particular, the proportional and derivative parts haven't been independently chosen, but imposing they satisfy a critical damping condition both in translation and rotation control instead. An additional parametric study has been performed as well to choose a suitable set of gains for the Impedance Control of the two arms. An applicability range evaluation analysis has been conducted considering out-of-design values for the target initial kinematic conditions which showed a good effectiveness of the controller from this point of view as well.

Chapter 4

Closed-loop system dynamics and operations

The goal of the present chapter is to design a post-grasping docking mission of a target object to be retrieved towards the space manipulator base platform. The attention will be focused on developing a multi-body dynamic model of the closed-loop system formed by a fully flexible Space Manipulator System (SMS) and the non-cooperative target object to be manipulated and on synthesizing a suitable control strategy for the mission to be accomplished. The controlled dynamics of the system will be simulated by means of an in-house developed Matlab code combined with MSC Nastran for what concerns the extraction of the structural dynamics properties of the flexible components.

To begin with, the dynamics equations of a fully flexible three-dimensional space manipulator are recalled in the following section.

4.1 Space Manipulator System dynamics equations

Assume the space multi-body system can be represented by N bodies interconnected by $N-1$ joints, leading to a serial kinematic chain as depicted in Figure 4.1. Now associate a reference frame to each body b_i of the kinematic chain (more specifically, for the base platform, the axes of such frame will be parallel to the base sides directions; for the arms links, the x body axis will be directed along the link longitudinal axis, while the other two will be positioned so as to form a right-hand orthonormal frame). Position of the origin (O_i) of this reference frame with respect to the origin of the inertial reference frame (O_I) can be indicated by vector ${}^{I}_{O_I}\boldsymbol{r}_{O_i}$, where the bottom right index represents the endpoint of vector $\boldsymbol{r}$ and the bottom

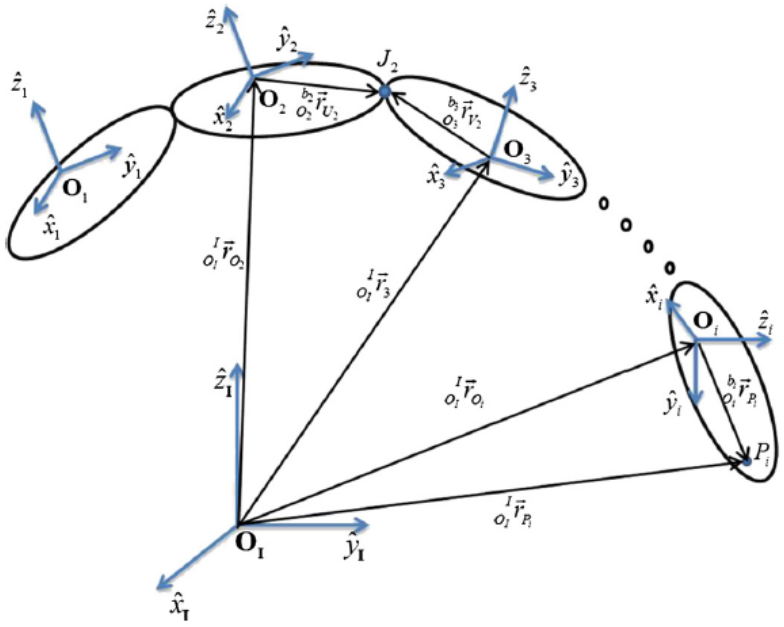

Figure 4.1. Reference frames associated to the multi-body system.

and upper left indexes represent its origin (O_I) and the reference frame (I) in which the same vector is expressed in, respectively. In a similar way, the attitude of the body b_i is described by a transformation matrix ${}^{I}\mathbf{T}_{b_i}$, which maps the coordinates from the reference frame detected by the bottom right index (b_i) to the reference frame identified by the upper left index (I). The inertial reference frame considered in the following is an Earth-Centered Inertial (ECI) frame.

The variables which will be used have the following meaning:

m_b = mass of body b

${}^{b}_{O_b}\mathbf{I}_{0_b}$ = rigid inertia tensor of body b with respect to the b body frame

${}^{b}_{O_b}\tilde{\mathbf{I}}_b$ = second-order elastic inertia tensor of body b with respect to the b body frame

${}^{b}_{I}\boldsymbol{\Omega}_b = \mathrm{skw}({}^{b}_{I}\boldsymbol{\omega}_b)$

${}^{b}\boldsymbol{\Lambda}_k$ = k-th translational modal participation factor for body b expressed in the b body frame

${}^{b}\tilde{\boldsymbol{\Gamma}}_k$ = k-th elastic rotational modal participation factor for body b expressed in the b body frame

${}^{b}\tilde{\boldsymbol{p}}_b$ = elastic static moment of body b expressed in the b body frame

${}^{B}_{O_B}\boldsymbol{d}^{C}_{R}$ = vector joining the base c.m. with the right panel clamping point
${}^{B}_{O_B}\mathbf{D}^{C}_{R} = \text{skw}({}^{B}_{O_B}\boldsymbol{d}^{C}_{R})$
${}^{B}_{O_B}\boldsymbol{d}^{C}_{L}$ = vector joining the base c.m. with the left panel clamping point
${}^{B}_{O_B}\mathbf{D}^{C}_{L} = \text{skw}({}^{B}_{O_B}\boldsymbol{d}^{C}_{L})$

See [79] for the definition of the listed and additional variables appearing in the following equations. The skw$(\cdot)$ operator outputs the skew-symmetric matrix built on the vector being its argument. Furthermore, $\boldsymbol{\omega}_b$ and ${}^{b}A_k$ respectively indicate an angular velocity and the k-th modal amplitude associated to body b.

The first issue to be addressed is how to describe the dynamics of the manipulator base+solar panels assembly. This can be accomplished by the following steps:

1. Write the translational, rotational and elastic equations for each of the two flexible solar panels;

2. Write the translational and rotational equations for the manipulator rigid base platform;

3. Combine the latter by means of the reaction forces and torques (present in the equations of the three bodies) in order to form an overall flexible monolithic body.

This procedure leads to the equations presented hereafter. The base body frame origin is located at its center of mass. For the translation:

$$
\begin{aligned}
&(m_B+2m_P)\,{}^{I}_{O_I}\ddot{\boldsymbol{r}}_{O_B} - (m_P\,{}^{I}_{O_B}\mathbf{D}^{c}_{R} + {}^{I}\mathbf{T}_{B}\,{}^{B}\mathbf{T}_{P_R}\,{}^{P_R}\tilde{\boldsymbol{p}}_{P_R} + m_P\,{}^{I}_{O_B}\mathbf{D}^{c}_{L} + {}^{I}\mathbf{T}_{B}\,{}^{B}\mathbf{T}_{P_L}\,{}^{P_L}\tilde{\boldsymbol{p}}_{P_L})\,{}^{I}\mathbf{T}_{B}\,{}^{B}_{I}\dot{\boldsymbol{\omega}}_{B} + \\
&\quad + \sum_{k=1}^{{}^{P}N_M} {}^{I}\mathbf{T}_{B}({}^{P_R}\ddot{A}_k\,{}^{B}\mathbf{T}_{P_R} + {}^{P_L}\ddot{A}_k\,{}^{B}\mathbf{T}_{P_L})\,{}^{P}\boldsymbol{\Lambda}_k = -m_P\,{}^{I}_{I}\boldsymbol{\Omega}^2_{B}({}^{I}_{O_B}\boldsymbol{d}^{c}_{R} + {}^{I}_{O_B}\boldsymbol{d}^{c}_{L}) + \\
&-{}^{I}_{I}\boldsymbol{\Omega}^2_{B}\,{}^{I}\mathbf{T}_{B}({}^{B}\mathbf{T}_{P_R}\,{}^{P_R}\tilde{\boldsymbol{p}}_{P_R} + {}^{B}\mathbf{T}_{P_L}\,{}^{P_L}\tilde{\boldsymbol{p}}_{P_L}) - 2\,{}^{I}_{I}\boldsymbol{\Omega}_{B} \sum_{k=1}^{{}^{P}N_M} {}^{I}\mathbf{T}_{B}({}^{P_R}\dot{A}_k\,{}^{B}\mathbf{T}_{P_R} + {}^{P_L}\dot{A}_k\,{}^{B}\mathbf{T}_{P_L})\,{}^{P}\boldsymbol{\Lambda}_k + \\
&\qquad - m_P\mu_E\left(\frac{{}^{I}_{O_I}\boldsymbol{r}_{O_{P_R}}}{|{}^{I}_{O_I}\boldsymbol{r}_{O_{P_R}}|^3} + \frac{{}^{I}_{O_I}\boldsymbol{r}_{O_{P_L}}}{|{}^{I}_{O_I}\boldsymbol{r}_{O_{P_L}}|^3}\right) - m_B\mu_E\frac{{}^{I}_{O_I}\boldsymbol{r}_{O_B}}{|{}^{I}_{O_I}\boldsymbol{r}^3_{O_B}|} \qquad (4.1)
\end{aligned}
$$

For the rotation:

$$
\begin{aligned}
&({}^{B}_{O_B}\mathbf{I}_{0_B} - {}^{B}_{O_B}\mathbf{D}^{c}_{R}\,{}^{I}\mathbf{T}^{TI}_{BO_B}\mathbf{D}^{c}_{R}\,{}^{I}\mathbf{T}_{B} m_P - {}^{B}_{O_B}\mathbf{D}^{c}_{R}\,{}^{I}\mathbf{T}^{TI}_{B}\mathbf{T}_{B}\,{}^{B}\mathbf{T}_{P_R}\,{}^{P_R}\tilde{\mathbf{P}}_{P_R}\,{}^{I}\mathbf{T}_{B} + \\
&- {}^{B}_{O_B}\mathbf{D}^{c}_{L}\,{}^{I}\mathbf{T}^{TI}_{BO_B}\mathbf{D}^{c}_{L}\,{}^{I}\mathbf{T}_{B} m_P - {}^{B}_{O_B}\mathbf{D}^{c}_{L}\,{}^{I}\mathbf{T}^{TI}_{B}\mathbf{T}_{B}\,{}^{B}\mathbf{T}_{P_L}\,{}^{P_L}\tilde{\mathbf{P}}_{P_L}\,{}^{I}\mathbf{T}_{B} + \\
&- {}^{B}\mathbf{T}_{P_R}\,{}^{P_R}\tilde{\boldsymbol{p}}_{P_R}\,{}^{B}\mathbf{T}_{P_R}\,{}^{I}\mathbf{T}^{TI}_{BO_B}\mathbf{D}^{c}_{R}\,{}^{I}\mathbf{T}_{B} + {}^{B}\mathbf{T}_{P_R}\,{}^{P_R}_{O_{P_R}}\tilde{\mathbf{I}}_{P_R}\,{}^{B}\mathbf{T}^{T}_{P_R} + \\
&- {}^{B}\mathbf{T}_{P_L}\,{}^{P_L}\tilde{\mathbf{P}}_{P_L}\,{}^{B}\mathbf{T}^{T}_{P_L}\,{}^{I}\mathbf{T}^{TI}_{BO_B}\mathbf{D}^{c}_{L}\,{}^{I}\mathbf{T}_{B} + {}^{B}\mathbf{T}_{P_L}\,{}^{P_L}_{O_{P_L}}\tilde{\mathbf{I}}_{P_L}\,{}^{B}\mathbf{T}^{T}_{P_L})\,{}^{B}_{I}\dot{\boldsymbol{\omega}}_{B} + \\
&+ [({}^{B}_{O_B}\mathbf{D}^{c}_{R} + {}^{B}_{O_B}\mathbf{D}^{c}_{L})m_P + {}^{B}\mathbf{T}_{P_R}\,{}^{P_R}\tilde{\mathbf{P}}_{P_R}\,{}^{B}\mathbf{T}^{T}_{P_R} + {}^{B}\mathbf{T}_{P_L}\,{}^{P_L}\tilde{\mathbf{P}}_{P_L}\,{}^{B}\mathbf{T}^{T}_{P_L}]\,{}^{I}\mathbf{T}^{TI}_{BO_I}\ddot{\boldsymbol{r}}_{O_B} + \\
&+ {}^{B}_{O_B}\mathbf{D}^{c}_{R}\,{}^{I}\mathbf{T}^{T}_{B}\sum_{k=1}^{{}^{P}N_M}{}^{I}\mathbf{T}_{B}\,{}^{B}\mathbf{T}_{P_R}\,{}^{P}\mathbf{\Lambda}_{k}\,{}^{P_R}\ddot{A}_k + {}^{B}_{O_B}\mathbf{D}^{c}_{L}\,{}^{I}\mathbf{T}^{T}_{B}\sum_{k=1}^{{}^{P}N_M}{}^{I}\mathbf{T}_{B}\,{}^{B}\mathbf{T}_{P_L}\,{}^{P}\mathbf{\Lambda}_{k}\,{}^{P_L}\ddot{A}_k + \\
&+ {}^{B}\mathbf{T}_{P_R}\sum_{k=1}^{{}^{P}N_M}{}^{P_R}\tilde{\mathbf{\Gamma}}_{k}\,{}^{P_R}\ddot{A}_k + {}^{B}\mathbf{T}_{P_L}\sum_{k=1}^{{}^{P}N_M}{}^{P_L}\tilde{\mathbf{\Gamma}}_{k}\,{}^{P_L}\ddot{A}_k = \\
&= -{}^{B}_{I}\mathbf{\Omega}_{B}\,{}^{B}_{O_B}\mathbf{I}_{0_B}\,{}^{B}_{I}\boldsymbol{\omega}_{B} - {}^{B}_{O_B}\mathbf{D}^{c}_{R}\,{}^{I}\mathbf{T}^{T}_{B}({}^{I}_{I}\mathbf{\Omega}^{2}_{B}\,{}^{I}_{BO_B}\boldsymbol{d}^{c}_{R} m_P + {}^{I}_{I}\mathbf{\Omega}^{2}_{B}\,{}^{I}\mathbf{T}_{B}\,{}^{B}\mathbf{T}_{P_R}\,{}^{P_R}\tilde{\boldsymbol{p}}_{P_R} + \\
&+ 2{}^{I}_{I}\mathbf{\Omega}_{B}\sum_{k=1}^{{}^{P}N_M}{}^{I}\mathbf{T}_{B}\,{}^{B}\mathbf{T}_{P_R}\,{}^{P}\mathbf{\Lambda}_{k}\,{}^{P_R}\dot{A}_k) - {}^{B}_{O_B}\mathbf{D}^{c}_{L}\,{}^{I}\mathbf{T}^{T}_{B}({}^{I}_{I}\mathbf{\Omega}^{2}_{B}\,{}^{I}_{BO_B}\boldsymbol{d}^{c}_{L} m_P + {}^{I}_{I}\mathbf{\Omega}^{2}_{B}\,{}^{I}\mathbf{T}_{B}\,{}^{B}\mathbf{T}_{P_L}\,{}^{P_L}\tilde{\boldsymbol{p}}_{P_L} + \\
&+ 2{}^{I}_{I}\mathbf{\Omega}_{B}\sum_{k=1}^{{}^{P}N_M}{}^{I}\mathbf{T}_{B}\,{}^{B}\mathbf{T}_{P_L}\,{}^{P}\mathbf{\Lambda}_{k}\,{}^{P_L}\dot{A}_k) - {}^{B}\mathbf{T}_{P_R}\Bigg[\sum_{k=1}^{{}^{P}N_M}{}^{P_R}_{O_{P_R}}\tilde{\mathbf{I}}^{k}_{1_{P_R}}\,{}^{P_R}\dot{A}_k\,{}^{B}\mathbf{T}^{T}_{P_R}\,{}^{B}_{I}\boldsymbol{\omega}_{B} + \\
&+ \sum_{k=1}^{{}^{P}N_M}\sum_{t=1}^{{}^{P}N_M}{}^{P_R}\mathbf{\Xi}^{kt}\,{}^{P_R}\dot{A}_t\,{}^{P_R}\dot{A}_k + {}^{P_R}_{I}\mathbf{\Omega}_{B}({}^{P_R}_{O_{P_R}}\tilde{\mathbf{I}}_{P_R}\,{}^{B}\mathbf{T}^{T}_{P_R}\,{}^{B}_{I}\boldsymbol{\omega}_{B} + \sum_{k=1}^{{}^{P}N_M}{}^{P_R}\tilde{\mathbf{\Gamma}}_{k}\,{}^{P_R}\dot{A}_k)\Bigg] + \\
&- {}^{B}\mathbf{T}_{P_L}\Bigg[\sum_{k=1}^{{}^{P}N_M}{}^{P_L}_{O_{P_L}}\tilde{\mathbf{I}}^{k}_{1_{P_L}}\,{}^{P_L}\dot{A}_k\,{}^{B}\mathbf{T}^{T}_{P_L}\,{}^{B}_{I}\boldsymbol{\omega}_{B} + \sum_{k=1}^{{}^{P}N_M}\sum_{t=1}^{{}^{P}N_M}{}^{P_L}\mathbf{\Xi}^{kt}\,{}^{P_L}\dot{A}_t\,{}^{P_L}\dot{A}_k + \\
&+ {}^{P_L}_{I}\mathbf{\Omega}_{B}({}^{P_L}_{O_{P_L}}\tilde{\mathbf{I}}_{P_L}\,{}^{B}\mathbf{T}^{T}_{P_L}\,{}^{B}_{I}\boldsymbol{\omega}_{B} + \sum_{k=1}^{{}^{P}N_M}{}^{P_L}\tilde{\mathbf{\Gamma}}_{k}\,{}^{P_L}\dot{A}_k)\Bigg] + \\
&- m_P\mu_E\left({}^{B}_{O_B}\mathbf{D}^{c}_{R}\frac{{}^{B}_{O_I}\boldsymbol{r}_{O_{P_R}}}{|{}^{B}_{O_I}\boldsymbol{r}_{O_{P_R}}|^3} + {}^{B}_{O_B}\mathbf{D}^{c}_{L}\frac{{}^{B}_{O_I}\boldsymbol{r}_{O_{P_L}}}{|{}^{B}_{O_I}\boldsymbol{r}_{O_{P_L}}|^3}\right) + \\
&+ {}^{B}\mathbf{T}_{P_R}\left[-\frac{\mu_E}{|{}^{P_R}_{O_I}\boldsymbol{r}_{O_{P_R}}|^2}\left({}^{P_R}\tilde{\boldsymbol{p}}_{P_R}\times\frac{{}^{P_R}_{O_I}\boldsymbol{r}_{O_{P_R}}}{|{}^{P_R}_{O_I}\boldsymbol{r}_{O_{P_R}}|}\right) + 3\frac{\mu_E}{|{}^{P_R}_{O_I}\boldsymbol{r}_{O_{P_R}}|^3}\left(\frac{{}^{P_R}_{O_I}\boldsymbol{r}_{O_{P_R}}}{|{}^{P_R}_{O_I}\boldsymbol{r}_{O_{P_R}}|}\times{}^{P_R}_{O_{P_R}}\tilde{\mathbf{I}}_{P_R}\frac{{}^{P_R}_{O_I}\boldsymbol{r}_{O_{P_R}}}{|{}^{P_R}_{O_I}\boldsymbol{r}_{O_{P_R}}|}\right)\right] + \\
&+ {}^{B}\mathbf{T}_{P_L}\left[-\frac{\mu_E}{|{}^{P_L}_{O_I}\boldsymbol{r}_{O_{P_L}}|^2}\left({}^{P_L}\tilde{\boldsymbol{p}}_{P_L}\times\frac{{}^{P_L}_{O_I}\boldsymbol{r}_{O_{P_L}}}{|{}^{P_L}_{O_I}\boldsymbol{r}_{O_{P_L}}|}\right) + 3\frac{\mu_E}{|{}^{P_L}_{O_I}\boldsymbol{r}_{O_{P_L}}|^3}\left(\frac{{}^{P_L}_{O_I}\boldsymbol{r}_{O_{P_L}}}{|{}^{P_L}_{O_I}\boldsymbol{r}_{O_{P_L}}|}\times{}^{P_L}_{O_{P_L}}\tilde{\mathbf{I}}_{P_L}\frac{{}^{P_L}_{O_I}\boldsymbol{r}_{O_{P_L}}}{|{}^{P_L}_{O_I}\boldsymbol{r}_{O_{P_L}}|}\right)\right] + \\
&- \frac{\mu_E}{|{}^{B}_{O_I}\boldsymbol{r}_{O_B}|^2}\left({}^{B}\tilde{\boldsymbol{p}}_{B}\times\frac{{}^{B}_{O_I}\boldsymbol{r}_{O_B}}{|{}^{B}_{O_I}\boldsymbol{r}_{O_B}|}\right) + 3\frac{\mu_E}{|{}^{B}_{O_I}\boldsymbol{r}_{O_B}|^3}\left(\frac{{}^{B}_{O_I}\boldsymbol{r}_{O_B}}{|{}^{B}_{O_I}\boldsymbol{r}_{O_B}|}\times{}^{B}_{O_B}\tilde{\mathbf{I}}_{B}\frac{{}^{B}_{O_I}\boldsymbol{r}_{O_B}}{|{}^{B}_{O_I}\boldsymbol{r}_{O_B}|}\right)
\end{aligned}
\tag{4.2}
$$

The k-th modal equation for the right solar panel is the following:

$$\begin{aligned}
&{}^{P_R}\ddot{A}_k + {}^{P}\mathbf{\Lambda}_k^{TB}\mathbf{T}_{P_R}^{T}\,{}^{I}\mathbf{T}_{BO_I}^{TI}\ddot{\boldsymbol{r}}_{O_B} + ({}^{P_R}\tilde{\mathbf{\Gamma}}_k^{TB}\mathbf{T}_{P_R}^{T} - {}^{P}\mathbf{\Lambda}_k^{TB}\mathbf{T}_{P_R}^{T}\,{}^{I}\mathbf{T}_{BO_B}^{TI}\mathbf{D}_R^{c}\,{}^{I}\mathbf{T}_B)_I^B\dot{\boldsymbol{\omega}}_B = \\
&\qquad = -{}^{P}\mathbf{\Lambda}_k^{TB}\mathbf{T}_{P_R}^{T}\,{}^{I}\mathbf{T}_{BI}^{TI}\mathbf{\Omega}_{BO_B}^{2\,I}\boldsymbol{d}_R^{c} - {}^{P}\omega_k^{2\,P_R}A_k - 2^{P}\zeta_k\,{}^{P}\omega_k\,{}^{P_R}\dot{A}_k + \\
&\qquad + \frac{1}{2}{}_I^{P_R}\boldsymbol{\omega}_{BO_{P_R}}^{T\,P_R}\tilde{\mathbf{I}}_{1_{P_R}}^{k}\,{}_I^{P_R}\boldsymbol{\omega}_B - 2{}_I^{P_R}\boldsymbol{\omega}_B^{T}\sum_{t=1}^{{}^{P}N_M}{}^{P_R}\mathbf{\Xi}^{kt\,P_R}\dot{A}_t, \qquad \text{for} \quad k = 1, \ldots, {}^{P}N_M
\end{aligned} \tag{4.3}$$

The modal equations for the left solar panel are structurally analogous to equations (4.3) besides changing the index R into L and are not rewritten for the sake of brevity. In the above written equations, μ_E is the Earth gravitational parameter, ${}_{O_I}^{I}\boldsymbol{r}_{O_{P_R}} = {}_{O_I}^{I}\boldsymbol{r}_{O_B} + {}_{O_B}^{I}\boldsymbol{d}_R^c$ is the position of the origin of the right panel body frame (and analogously for the left panel) and ${}^{P}N_M$ is the number of modes considered for each panel. The translational equation is expressed in the inertial frame, the rotational one in the base body frame and the elastic ones are projected along the respective modes directions.

Shifting to the robotic arms, the translational dynamics equation for the i-th link of the j-th arm (having its body frame centered at its left endpoint) is given by:

$$\begin{aligned}
&m_{ij}{}_{O_I}^{I}\ddot{\boldsymbol{r}}_{O_{ij}} - {}^{I}\tilde{\mathbf{P}}_{ij}\,{}^{I}\mathbf{T}_{ij}\,{}_I^{ij}\dot{\boldsymbol{\omega}}_{ij} + \sum_{k=1}^{{}^{L}N_M}{}^{I}\mathbf{T}_{ij}\,{}^{ij}\mathbf{\Lambda}_k\,{}^{ij}\ddot{A}_k = \\
&\qquad\qquad - {}_I^{I}\mathbf{\Omega}_{ij}^{2\,I}\tilde{\boldsymbol{p}}_{ij} - 2{}_I^{I}\mathbf{\Omega}_{ij}\sum_{k=1}^{{}^{L}N_M}{}^{I}\mathbf{T}_{ij}\,{}^{ij}\mathbf{\Lambda}_k\,{}^{ij}\dot{A}_k - m_{ij}\mu_E\frac{{}_{O_I}^{I}\boldsymbol{r}_{O_{ij}}}{|{}_{O_I}^{I}\boldsymbol{r}_{O_{ij}}|^3}
\end{aligned} \tag{4.4}$$

The link rotational dynamics equation is the following:

$$\begin{aligned}
&{}_{O_{ij}}^{ij}\tilde{\mathbf{I}}_{ij}\,{}_I^{ij}\dot{\boldsymbol{\omega}}_{ij} + {}^{ij}\tilde{\mathbf{P}}_{ij}\,{}^{I}\mathbf{T}_{ij\,O_I}^{TI}\ddot{\boldsymbol{r}}_{O_{ij}} + \sum_{k=1}^{{}^{L}N_M}{}^{ij}\tilde{\mathbf{\Gamma}}_k\,{}^{ij}\ddot{A}_k = \\
&= -\left(\sum_{k=1}^{{}^{L}N_M}{}_{O_{ij}}^{ij}\tilde{\mathbf{I}}_{1_{ij}}^{k}\,{}^{ij}\dot{A}_k + {}_I^{ij}\tilde{\mathbf{\Omega}}_{ij}\,{}_{O_{ij}}^{ij}\tilde{\mathbf{I}}_{ij}\right){}_I^{ij}\boldsymbol{\omega}_{ij} - \sum_{k=1}^{{}^{L}N_M}\sum_{t=1}^{{}^{L}N_M}{}^{ij}\mathbf{\Xi}^{kt\,ij}\dot{A}_t\,{}^{ij}\dot{A}_k - {}_I^{ij}\mathbf{\Omega}_{ij}\sum_{k=1}^{{}^{L}N_M}{}^{ij}\tilde{\mathbf{\Gamma}}_k\,{}^{ij}\dot{A}_k + \\
&\quad - \frac{\mu_E}{|{}_{O_I}^{ij}\boldsymbol{r}_{O_{ij}}|^2}\left({}^{ij}\tilde{\boldsymbol{p}}_{ij} \times \frac{{}_{O_I}^{ij}\boldsymbol{r}_{O_{ij}}}{|{}_{O_I}^{ij}\boldsymbol{r}_{O_{ij}}|}\right) + 3\frac{\mu_E}{|{}_{O_I}^{ij}\boldsymbol{r}_{O_{ij}}|^3}\left(\frac{{}_{O_I}^{ij}\boldsymbol{r}_{O_{ij}}}{|{}_{O_I}^{ij}\boldsymbol{r}_{O_{ij}}|} \times {}_{O_{ij}}^{ij}\tilde{\mathbf{I}}_{ij}\frac{{}_{O_I}^{ij}\boldsymbol{r}_{O_{ij}}}{|{}_{O_I}^{ij}\boldsymbol{r}_{O_{ij}}|}\right)
\end{aligned} \tag{4.5}$$

The k-th modal equation for the link is furthermore given by:

$$
\begin{aligned}
&{}^{ij}\ddot{A}_k + {}^{ij}\mathbf{\Lambda}_k^{TI}\mathbf{T}_{ijO_I}^{TI}\ddot{\boldsymbol{r}}_{O_{ij}} + {}^{ij}\tilde{\mathbf{\Gamma}}_{kI}^{Tij}\dot{\boldsymbol{\omega}}_{ij} = \\
&= -{}^{ij}\omega_k^{2ij}A_k - 2^{ij}\zeta_k{}^{ij}\omega_k{}^{ij}\dot{A}_k + \frac{1}{2}{}_I^{ij}\boldsymbol{\omega}_{ijO_{ij}}^{Tij}\tilde{\mathbf{I}}_{1_{ij}I}^{k\ ij}\boldsymbol{\omega}_{ij} - 2_I^{ij}\boldsymbol{\omega}_{ij}^T\sum_{t=1}^{{}^L N_M}{}^{ij}\boldsymbol{\Xi}^{kt\,ij}\dot{A}_t + F_k, \\
&\qquad\qquad\qquad\qquad\qquad\qquad\qquad\qquad\qquad\qquad \text{for} \quad k = 1, \ldots, {}^L N_M \quad (4.6)
\end{aligned}
$$

where ${}^L N_M$ is the number of modes considered for each link. Here too, the translational equation is expressed in the inertial reference frame, the rotational one in the link body frame and the flexibility ones are projected along the link modes directions. For both the solar panels and the links, the projections of the gravity actions onto the elastic modes have not been considered since their contributions are negligible with respect to the other forcing terms. In Eq. (4.6), F_k will identify the projection of the control actions onto the k-th mode of the link being examined (once control will have been introduced). It is equal to

$$
F_k = \sum_{s=1}^{n_{\text{conc}}} -\boldsymbol{T}_{\text{conc}_s}^T\boldsymbol{\Theta}_k(\bar{\boldsymbol{\xi}}_s) \tag{4.7}
$$

where n_{conc} concentrated torques $\boldsymbol{T}_{\text{conc}_s}$ (which will coincide with the joint control torques) are supposed to be acting on the link at points $\bar{\boldsymbol{\xi}}_s$ (in body coordinates); furthermore, $\boldsymbol{\Theta}_k(\bar{\boldsymbol{\xi}}_s)$ represents the vector of the k-th modal angular displacements at point $\bar{\boldsymbol{\xi}}_s$.

Equations from (4.1) to (4.6) form the overall SMS dynamics equations according to Newton's approach. Adopting Kane's method, they can be written in compact form as:

$$
\mathbf{J}^T\mathbf{M}\mathbf{J}\ddot{\boldsymbol{Q}}_{\text{m}} = -\mathbf{J}^T\mathbf{M}\dot{\mathbf{J}}\dot{\boldsymbol{Q}}_{\text{m}} + \mathbf{J}^T\boldsymbol{C} + \mathbf{J}^T\boldsymbol{F} \tag{4.8}
$$

where $\mathbf{J}$ is the Jacobian matrix, $\mathbf{M}$ is the generalized mass matrix, $\boldsymbol{C}$ is the non-linear velocity terms vector and $\boldsymbol{F}$ is the generalized forces vector. The control actions can also be introduced as follows:

$$
\mathbf{J}^T\mathbf{M}\mathbf{J}\ddot{\boldsymbol{Q}}_{\text{m}} = -\mathbf{J}^T\mathbf{M}\dot{\mathbf{J}}\dot{\boldsymbol{Q}}_{\text{m}} + \mathbf{J}^T\boldsymbol{C} + \mathbf{J}^T\boldsymbol{F} + \sum_{i=1}^{N_C}\mathbf{B}_i\boldsymbol{u}_i \tag{4.9}
$$

where N_C is the number of control vectors, $\boldsymbol{u}_i$ is the i-th control vector and $\mathbf{B}_i$ is the matrix that maps the i-th control vector onto the dynamics equations. The vector $\mathbf{B}_i\boldsymbol{u}_i$ is not pre-multiplied by the transpose Jacobian matrix $\mathbf{J}^{\text{T}}$ since the control actions are the ones already referred to the minimal variables.

Nevertheless, it is convenient (for numerical integration motivations), to write equation (4.9) in the form of a first-order system:

$$\begin{bmatrix} {}^{I}_{O_I}\dot{\boldsymbol{r}}_{O_B} \\ {}^{I}\dot{\boldsymbol{q}}_B \\ \dot{\boldsymbol{\theta}}_{J_1} \\ \dot{q}_1 \\ \dot{\boldsymbol{\theta}}_{J_2} \\ \dot{q}_2 \\ {}^{P_R}\dot{\boldsymbol{A}} \\ {}^{P_L}\dot{\boldsymbol{A}} \\ {}^{arm_1}\dot{\boldsymbol{A}} \\ {}^{arm_2}\dot{\boldsymbol{A}} \\ {}^{I}_{O_I}\ddot{\boldsymbol{r}}_{O_B} \\ {}^{B}_{I}\dot{\boldsymbol{\omega}}_B \\ \ddot{\boldsymbol{\theta}}_{J_1} \\ \ddot{q}_1 \\ \ddot{\boldsymbol{\theta}}_{J_2} \\ \ddot{q}_2 \\ {}^{P_R}\ddot{\boldsymbol{A}} \\ {}^{P_L}\ddot{\boldsymbol{A}} \\ {}^{arm_1}\ddot{\boldsymbol{A}} \\ {}^{arm_2}\ddot{\boldsymbol{A}} \end{bmatrix} = \begin{bmatrix} \mathbf{A}_{11} & \mathbf{A}_{12} \\ \mathbf{A}_{21} & \mathbf{A}_{22} \end{bmatrix} \begin{bmatrix} {}^{I}_{O_I}\boldsymbol{r}_{O_B} \\ {}^{I}\boldsymbol{q}_B \\ \boldsymbol{\theta}_{J_1} \\ q_1 \\ \boldsymbol{\theta}_{J_2} \\ q_2 \\ {}^{P_R}\boldsymbol{A} \\ {}^{P_L}\boldsymbol{A} \\ {}^{arm_1}\boldsymbol{A} \\ {}^{arm_2}\boldsymbol{A} \\ {}^{I}_{O_I}\dot{\boldsymbol{r}}_{O_B} \\ {}^{B}_{I}\boldsymbol{\omega}_B \\ \dot{\boldsymbol{\theta}}_{J_1} \\ \dot{q}_1 \\ \dot{\boldsymbol{\theta}}_{J_2} \\ \dot{q}_2 \\ {}^{P_R}\dot{\boldsymbol{A}} \\ {}^{P_L}\dot{\boldsymbol{A}} \\ {}^{arm_1}\dot{\boldsymbol{A}} \\ {}^{arm_2}\dot{\boldsymbol{A}} \end{bmatrix} + \\ + \begin{bmatrix} \mathbf{0}^{(7+2^P N_M+2(1+^L N_M)n_l)\times 1} \\ (\mathbf{J}^{\mathrm{T}}\mathbf{M}\mathbf{J})^{-1}\mathbf{J}^{\mathrm{T}}\boldsymbol{C} \end{bmatrix} + \begin{bmatrix} \mathbf{0}^{(7+2^P N_M+2(1+^L N_M)n_l)\times 1} \\ (\mathbf{J}^{\mathrm{T}}\mathbf{M}\mathbf{J})^{-1}\mathbf{J}^{\mathrm{T}}\boldsymbol{F} \end{bmatrix} + \begin{bmatrix} \mathbf{0}^{(7+2^P N_M+2(1+^L N_M)n_l)\times 1} \\ (\mathbf{J}^{\mathrm{T}}\mathbf{M}\mathbf{J})^{-1}\sum_{i=1}^{N_C}\mathbf{B}_i\boldsymbol{u}_i \end{bmatrix} \tag{4.10}$$

where $\mathbf{A}_{11}$ is entirely formed by zero elements besides the block occupying rows and columns ranging from 4 to 7 made of the ${}^{B}\mathbf{W}_B$ matrix (its meaning will be explained shortly hereafter), and

$$\mathbf{A}_{12} = \begin{bmatrix} \mathbf{A}_{12_1} & \mathbf{A}_{12_2} & \mathbf{A}_{12_3} & \mathbf{A}_{12_4} & \mathbf{A}_{12_5} & \mathbf{A}_{12_6} & \mathbf{A}_{12_7} & \mathbf{A}_{12_8} & \mathbf{A}_{12_9} & \mathbf{A}_{12_{10}} \end{bmatrix} \tag{4.11}$$

where

$$\mathbf{A}_{12_1} = \begin{bmatrix} \mathbf{I}^{3\times3} \\ \mathbf{0}^{4\times3} \\ \mathbf{0}^{(n_l-1)\times3} \\ \mathbf{0}^{1\times3} \\ \mathbf{0}^{(n_l-1)\times3} \\ \mathbf{0}^{1\times3} \\ \mathbf{0}^{^PN_M\times3} \\ \mathbf{0}^{^PN_M\times3} \\ \mathbf{0}^{^LN_Mn_l\times3} \\ \mathbf{0}^{^LN_Mn_l\times3} \end{bmatrix}, \quad \mathbf{A}_{12_2} = \begin{bmatrix} \mathbf{0}^{3\times3} \\ \mathbf{0}^{4\times3} \\ \mathbf{0}^{(n_l-1)\times3} \\ \mathbf{0}^{1\times3} \\ \mathbf{0}^{(n_l-1)\times3} \\ \mathbf{0}^{1\times3} \\ \mathbf{0}^{^PN_M\times3} \\ \mathbf{0}^{^PN_M\times3} \\ \mathbf{0}^{^LN_Mn_l\times3} \\ \mathbf{0}^{^LN_Mn_l\times3} \end{bmatrix}, \quad \mathbf{A}_{12_3} = \begin{bmatrix} \mathbf{0}^{3\times(n_l-1)} \\ \mathbf{0}^{4\times(n_l-1)} \\ \mathbf{I}^{(n_l-1)\times(n_l-1)} \\ \mathbf{0}^{1\times(n_l-1)} \\ \mathbf{0}^{(n_l-1)\times(n_l-1)} \\ \mathbf{0}^{1\times(n_l-1)} \\ \mathbf{0}^{^PN_M\times(n_l-1)} \\ \mathbf{0}^{^PN_M\times(n_l-1)} \\ \mathbf{0}^{^LN_Mn_l\times(n_l-1)} \\ \mathbf{0}^{^LN_Mn_l\times(n_l-1)} \end{bmatrix},$$

$$\mathbf{A}_{12_4} = \begin{bmatrix} \mathbf{0}^{3\times1} \\ \mathbf{0}^{4\times1} \\ \mathbf{0}^{(n_l-1)\times1} \\ 1 \\ \mathbf{0}^{(n_l-1)\times1} \\ 0 \\ \mathbf{0}^{^PN_M\times1} \\ \mathbf{0}^{^PN_M\times1} \\ \mathbf{0}^{^LN_Mn_l\times1} \\ \mathbf{0}^{^LN_Mn_l\times1} \end{bmatrix}, \quad \mathbf{A}_{12_5} = \begin{bmatrix} \mathbf{0}^{3\times(n_l-1)} \\ \mathbf{0}^{4\times(n_l-1)} \\ \mathbf{0}^{(n_l-1)\times(n_l-1)} \\ \mathbf{0}^{1\times(n_l-1)} \\ \mathbf{I}^{(n_l-1)\times(n_l-1)} \\ \mathbf{0}^{1\times(n_l-1)} \\ \mathbf{0}^{^PN_M\times(n_l-1)} \\ \mathbf{0}^{^PN_M\times(n_l-1)} \\ \mathbf{0}^{^LN_Mn_l\times(n_l-1)} \\ \mathbf{0}^{^LN_Mn_l\times(n_l-1)} \end{bmatrix}, \quad \mathbf{A}_{12_6} = \begin{bmatrix} \mathbf{0}^{3\times1} \\ \mathbf{0}^{4\times1} \\ \mathbf{0}^{(n_l-1)\times1} \\ 0 \\ \mathbf{0}^{(n_l-1)\times1} \\ 1 \\ \mathbf{0}^{^PN_M\times1} \\ \mathbf{0}^{^PN_M\times1} \\ \mathbf{0}^{^LN_Mn_l\times1} \\ \mathbf{0}^{^LN_Mn_l\times1} \end{bmatrix},$$

$$\mathbf{A}_{12_7} = \begin{bmatrix} \mathbf{0}^{3\times{}^PN_M} \\ \mathbf{0}^{4\times{}^PN_M} \\ \mathbf{0}^{(n_l-1)\times{}^PN_M} \\ \mathbf{0}^{1\times{}^PN_M} \\ \mathbf{0}^{(n_l-1)\times{}^PN_M} \\ \mathbf{0}^{1\times{}^PN_M} \\ \mathbf{I}^{^PN_M\times{}^PN_M} \\ \mathbf{0}^{^PN_M\times{}^PN_M} \\ \mathbf{0}^{^LN_Mn_l\times{}^PN_M} \\ \mathbf{0}^{^LN_Mn_l\times{}^PN_M} \end{bmatrix}, \quad \mathbf{A}_{12_8} = \begin{bmatrix} \mathbf{0}^{3\times{}^PN_M} \\ \mathbf{0}^{4\times{}^PN_M} \\ \mathbf{0}^{(n_l-1)\times{}^PN_M} \\ \mathbf{0}^{1\times{}^PN_M} \\ \mathbf{0}^{(n_l-1)\times{}^PN_M} \\ \mathbf{0}^{1\times{}^PN_M} \\ \mathbf{0}^{^PN_M\times{}^PN_M} \\ \mathbf{I}^{^PN_M\times{}^PN_M} \\ \mathbf{0}^{^LN_Mn_l\times{}^PN_M} \\ \mathbf{0}^{^LN_Mn_l\times{}^PN_M} \end{bmatrix}, \quad \mathbf{A}_{12_9} = \begin{bmatrix} \mathbf{0}^{3\times{}^LN_Mn_l} \\ \mathbf{0}^{4\times{}^LN_Mn_l} \\ \mathbf{0}^{(n_l-1)\times{}^LN_Mn_l} \\ \mathbf{0}^{1\times{}^LN_Mn_l} \\ \mathbf{0}^{(n_l-1)\times{}^LN_Mn_l} \\ \mathbf{0}^{1\times{}^LN_Mn_l} \\ \mathbf{0}^{^PN_M\times{}^LN_Mn_l} \\ \mathbf{0}^{^PN_M\times{}^LN_Mn_l} \\ \mathbf{I}^{^LN_Mn_l\times{}^LN_Mn_l} \\ \mathbf{0}^{^LN_Mn_l\times{}^LN_Mn_l} \end{bmatrix},$$

$$\mathbf{A}_{12_{10}} = \begin{bmatrix} \mathbf{0}^{3\times {}^{L}N_M n_l} \\ \mathbf{0}^{4\times {}^{L}N_M n_l} \\ \mathbf{0}^{(n_l-1)\times {}^{L}N_M n_l} \\ \mathbf{0}^{1\times {}^{L}N_M n_l} \\ \mathbf{0}^{(n_l-1)\times {}^{L}N_M n_l} \\ \mathbf{0}^{1\times {}^{L}N_M n_l} \\ \mathbf{0}^{{}^{P}N_M\times {}^{L}N_M n_l} \\ \mathbf{0}^{{}^{P}N_M\times {}^{L}N_M n_l} \\ \mathbf{0}^{{}^{L}N_M n_l\times {}^{L}N_M n_l} \\ \mathbf{I}^{{}^{L}N_M n_l\times {}^{L}N_M n_l} \end{bmatrix}$$

$$\mathbf{A}_{21} = \mathbf{0}^{(6+2^{P}N_M+2(1+{}^{L}N_M)n_l)\times(7+2^{P}N_M+2(1+{}^{L}N_M)n_l)}$$
$$\mathbf{A}_{22} = -\left(\mathbf{J}^{\mathrm{T}}\mathbf{M}\mathbf{J}\right)^{-1}\mathbf{J}^{\mathrm{T}}\mathbf{M}\dot{\mathbf{J}}$$

${}^{I}\boldsymbol{q}_B$ is the quaternions vector describing the base attitude with respect to the inertial reference frame (the first component is the scalar part and the last three form the vector portion of it) and ${}^{B}\mathbf{W}_B$ is the base angular velocity matrix used to integrate the quaternions kinematic equation, namely ${}^{I}\dot{\boldsymbol{q}}_B = {}^{B}\mathbf{W}_B {}^{I}\boldsymbol{q}_B$, where

$${}^{B}\mathbf{W}_B = \frac{1}{2}\begin{bmatrix} 0 & -\omega_1 & -\omega_2 & -\omega_3 \\ \omega_1 & 0 & \omega_3 & -\omega_2 \\ \omega_2 & -\omega_3 & 0 & \omega_1 \\ \omega_3 & \omega_2 & -\omega_1 & 0 \end{bmatrix}$$

in which the angular velocity components are expressed in the base body reference frame. Furthermore, $\boldsymbol{\theta}_{J_i}$ and q_i are respectively the joint angles vector and relative displacement of the last link translational joint for the i-th arm.

4.2 Closed-loop system modeling

The grasp condition between the manipulator end-effectors and the target is modeled imposing mechanical constraints on the chaser and target in correspondence of the relative grasping points. This is obtained by adding the appropriate compatibility equations and constraints reactions to the dynamics equations.

First of all, the equations of motion of the target object need to be added to those of the SMS. They can be formulated as follows (the target body frame origin

is located at its center of mass):

$$\mathbf{M}_{\mathrm{t}}\ddot{\boldsymbol{Q}}_{\mathrm{t}} = \boldsymbol{C}_{\mathrm{t}} + \boldsymbol{F}_{\mathrm{t}} + \mathbf{W}_{\mathrm{t}}\boldsymbol{R} \tag{4.12}$$

where $\ddot{\boldsymbol{Q}}_{\mathrm{t}} \in \mathbb{R}^{6\times 1}$ is the target acceleration vector (containing the target center of mass translational acceleration (with respect to the inertial reference frame and expressed in the same one) and the target angular acceleration about its center of mass (with respect to the inertial frame and expressed in the target body frame)), $\mathbf{M}_{\mathrm{t}} \in \mathbb{R}^{6\times 6}$, $\boldsymbol{C}_{\mathrm{t}} \in \mathbb{R}^{6\times 1}$, $\boldsymbol{F}_{\mathrm{t}} \in \mathbb{R}^{6\times 1}$ are respectively the target mass matrix, non-linear velocity terms vector and external applied forces; $\boldsymbol{R} \in \mathbb{R}^{6\times 1}$ are the grasp reaction forces, expressed with respect to the inertial frame, acting on the target (one force for each of the two grasp constraints; this is equivalent to model the constraint as a spherical joint positioned where the grasp actually takes place) and $\mathbf{W}_{\mathrm{t}} \in \mathbb{R}^{6\times 6}$ is the matrix which maps the reactions onto the target dynamics equations. The described variables have the following form:

$$\mathbf{M}_{\mathrm{t}} = \begin{bmatrix} m_{\mathrm{t}}\mathbf{I}^{3\times 3} & \mathbf{0}^{3\times 3} \\ \mathbf{0}^{3\times 3} & {}^{t}_{O_t}\mathbf{J}_t \end{bmatrix}$$

$$\mathbf{C}_{\mathrm{t}} = \begin{bmatrix} \mathbf{0}^{3\times 1} \\ -{}^{t}_{I}\boldsymbol{\Omega}_t {}^{t}_{O_t}\mathbf{J}_t {}^{t}_{I}\boldsymbol{\omega}_t \end{bmatrix}$$

Gravity actions have to be included in the $\boldsymbol{F}_{\mathrm{t}}$ vector leading to:

$$\boldsymbol{F}_{\mathrm{t}} = \begin{bmatrix} -m_{\mathrm{t}}\mu_E \frac{{}^{I}_{O_I}\boldsymbol{r}_{O_t}}{|{}^{I}_{O_I}\boldsymbol{r}_{O_t}|^3} \\ 3\frac{\mu_E}{|{}^{t}_{O_I}\boldsymbol{r}_{O_t}|^3}\left(\frac{{}^{t}_{O_I}\boldsymbol{r}_{O_t}}{|{}^{t}_{O_I}\boldsymbol{r}_{O_t}|} \times {}^{t}_{O_t}\tilde{\mathbf{I}}_t \frac{{}^{t}_{O_I}\boldsymbol{r}_{O_t}}{|{}^{t}_{O_I}\boldsymbol{r}_{O_t}|}\right) \end{bmatrix} \tag{4.13}$$

Furthermore, the $\mathbf{W}_{\mathrm{t}}$ matrix is given by

$$\mathbf{W}_{\mathrm{t}} = \begin{bmatrix} \mathbf{I}^{3\times 3} & \mathbf{I}^{3\times 3} \\ {}^{t}_{O_t}\mathbf{R}_{cm_t gp_1} {}^{I}\mathbf{T}_t^T & {}^{t}_{O_t}\mathbf{R}_{cm_t gp_2} {}^{I}\mathbf{T}_t^T \end{bmatrix} \tag{4.14}$$

where ${}^{t}_{O_t}\mathbf{R}_{cm_t gp_i}$, $i = 1, 2$ is the skew-matrix based on ${}^{t}_{O_t}\mathbf{r}_{cm_t gp_i}$ which is the vector joining the target center of mass with the i-th grasping point (expressed in the target body frame).

After having introduced the target dynamics, the SMS equations of motion are now suitably modified to take the grasp constraints into account. Indeed, they

become:

$$\mathbf{J}^T\mathbf{M}\mathbf{J}\ddot{\boldsymbol{Q}}_\mathrm{m} = -\mathbf{J}^T\mathbf{M}\dot{\mathbf{J}}\dot{\boldsymbol{Q}}_\mathrm{m} + \mathbf{J}^T\boldsymbol{C} + \mathbf{J}^T\boldsymbol{F} - \mathbf{J}^T\mathbf{W}_\mathrm{EE}\boldsymbol{R} + \mathbf{B}_\mathrm{c1}\boldsymbol{u}_\mathrm{a1} + \mathbf{B}_\mathrm{c2}\boldsymbol{u}_\mathrm{a2} + \mathbf{B}_\mathrm{cB}\boldsymbol{u}_\mathrm{B} \tag{4.15}$$

where $\mathbf{W}_\mathrm{EE} \in \mathbb{R}^{dim\,\dot{\boldsymbol{x}}\times 6}$ is the matrix mapping the constraints reactions onto the SMS dynamics equations. Since the reactions are acting on the last links of the two arms, the only non-null blocks of the latter are given by:

$$\mathbf{W}_\mathrm{EE}(1+6n_\mathrm{l} : 6+6n_\mathrm{l}, 1:6) = \begin{bmatrix} \mathbf{I}^{3\times3} & \mathbf{0}^{3\times3} \\ {}^{b_{1n_\mathrm{l}}}_{O_{1n_\mathrm{l}}}\boldsymbol{R}_{\mathrm{U}_{1n_\mathrm{l}}}\,{}^{I}\mathbf{T}^T_{\mathrm{b}_{1n_\mathrm{l}}} & \mathbf{0}^{3\times3} \end{bmatrix}$$

$$\mathbf{W}_\mathrm{EE}(1+12n_\mathrm{l} : 6+12n_\mathrm{l}, 1:6) = \begin{bmatrix} \mathbf{0}^{3\times3} & \mathbf{I}^{3\times3} \\ \mathbf{0}^{3\times3} & {}^{b_{2n_\mathrm{l}}}_{O_{2n_\mathrm{l}}}\boldsymbol{R}_{\mathrm{U}_{2n_\mathrm{l}}}\,{}^{I}\mathbf{T}^T_{\mathrm{b}_{2n_\mathrm{l}}} \end{bmatrix}$$

The system formed by equations (4.15) and (4.12) can be written as

$$\begin{bmatrix} \mathbf{J}^T\mathbf{M}\mathbf{J} & \mathbf{0} \\ \mathbf{0} & \mathbf{M}_\mathrm{t} \end{bmatrix} \begin{bmatrix} \ddot{\boldsymbol{Q}}_\mathrm{m} \\ \ddot{\boldsymbol{Q}}_\mathrm{t} \end{bmatrix} = \begin{bmatrix} -\mathbf{J}^T\mathbf{M}\dot{\mathbf{J}} & \mathbf{0} \\ \mathbf{0} & \mathbf{0} \end{bmatrix} \begin{bmatrix} \dot{\boldsymbol{Q}}_\mathrm{m} \\ \dot{\boldsymbol{Q}}_\mathrm{t} \end{bmatrix} + \begin{bmatrix} \mathbf{J}^T\boldsymbol{C} \\ \boldsymbol{C}_\mathrm{t} \end{bmatrix} + \begin{bmatrix} \mathbf{J}^T\boldsymbol{F} \\ \boldsymbol{F}_\mathrm{t} \end{bmatrix} +$$

$$+ \begin{bmatrix} -\mathbf{J}^T\mathbf{W}_\mathrm{EE} \\ \mathbf{W}_\mathrm{t} \end{bmatrix} \boldsymbol{R} + \begin{bmatrix} \boldsymbol{u} \\ \mathbf{0} \end{bmatrix} \rightarrow$$

$$\rightarrow \mathbf{M}_1^*\ddot{\boldsymbol{Q}} = \mathbf{M}_2^*\dot{\boldsymbol{Q}} + \boldsymbol{C}^* + \boldsymbol{F}^* + \mathbf{W}^*\boldsymbol{R} + \boldsymbol{u}^* \tag{4.16}$$

where $\boldsymbol{u} = \mathbf{B}_\mathrm{c1}\boldsymbol{u}_\mathrm{a1} + \mathbf{B}_\mathrm{c2}\boldsymbol{u}_\mathrm{a2} + \mathbf{B}_\mathrm{cB}\boldsymbol{u}_\mathrm{B}$. Eq. (4.16) will need to be reduced to a first order system for numerical integration purposes just as it was done for the SMS equations alone.

Kinematic compatibility conditions need to be imposed to properly represent the grasp constraints. Given the chosen equivalent spherical joint model, the compatibility equations need to impose a null relative translational motion between the SMS end-effectors and the relevant grasping points on the target body. The latter may be expressed in the following compact form:

$$\boldsymbol{\Phi} = \mathbf{0} \tag{4.17}$$

being

$$\begin{aligned}
&\boldsymbol{\Phi} = {}^{I}_{O_I}\boldsymbol{r}_{\mathrm{EE}_i} - {}^{I}_{O_I}\boldsymbol{r}_{\mathrm{gp}_i}\,, \quad i = 1,2\\
&{}^{I}_{O_I}\boldsymbol{r}_{\mathrm{EE}_i} = {}^{I}_{O_I}\boldsymbol{r}_{\mathrm{O_B}} + {}^{I}\mathbf{T}_{B}\,{}^{B}_{O_B}\boldsymbol{r}_{\mathrm{U_{B_i}}} + \sum_{i=1}^{n_\mathrm{l}} {}^{I}\mathbf{T}_{\mathrm{b}_{ij}}\left[{}^{b_{ij}}_{O_{ij}}\boldsymbol{r}_{\mathrm{U}_{ij}} + \sum_{k=1}^{{}^{L}N_M} {}^{ij}A_k\,{}^{b_{ij}}\boldsymbol{\varphi}_k(\boldsymbol{l}_{ij})\right]\\
&{}^{I}_{O_I}\boldsymbol{r}_{\mathrm{gp}_i} = {}^{I}_{O_I}\boldsymbol{r}_{\mathrm{O_t}} + {}^{I}\mathbf{T}_{t}\,{}^{t}_{O_t}\boldsymbol{r}_{cm_t gp_i}
\end{aligned}$$

where ${}^{B}_{O_B}\boldsymbol{r}_{\mathrm{U_{B_i}}}$ is the vector joining the origin of the base body frame with the attachment point of the i-th arm to the base itself, ${}^{b_{ij}}_{O_{ij}}\boldsymbol{r}_{\mathrm{U}_{ij}}$ is the vector joining the link endpoints in the non-deformed configuration and ${}^{b_{ij}}\boldsymbol{\varphi}_k(\boldsymbol{l}_{ij})$ identifies the k-th modal displacement at the link right endpoint. $\boldsymbol{\Phi}$ in Eq. (4.17) is thus a function of the state vector $\boldsymbol{Q}$.

The use of Eq. (4.17) finalized to the determination of the reaction forces could be problematic due to the high order of magnitude of some terms present in it (i.e. ${}^{I}_{O_I}\boldsymbol{r}_{\mathrm{O_B}}$ and ${}^{I}_{O_I}\boldsymbol{r}_{\mathrm{O_t}}$) with respect to the others. This issue can be overcome by expressing ${}^{I}_{O_I}\boldsymbol{r}_{\mathrm{O_t}}$ in terms of ${}^{I}_{O_I}\boldsymbol{r}_{\mathrm{O_B}}$ as

$$ {}^{I}_{O_I}\boldsymbol{r}_{\mathrm{O_t}} = {}^{I}_{O_I}\boldsymbol{r}_{\mathrm{O_B}} + {}^{I}_{O_B}\boldsymbol{r}_{\mathrm{O_t}} \tag{4.18}$$

where ${}^{I}_{O_B}\boldsymbol{r}_{\mathrm{O_t}}$ represents the vector joining the origins of the base body and target body frames. This will entail the elimination of the high order term ${}^{I}_{O_I}\boldsymbol{r}_{\mathrm{O_B}}$ in Eq. (4.17) leaving terms which display the same order of magnitude. Eq. (4.18) needs to be also used in the target dynamics equation (4.12) implying ${}^{I}_{O_B}\boldsymbol{r}_{\mathrm{O_t}}$ will take the place of ${}^{I}_{O_I}\boldsymbol{r}_{\mathrm{O_t}}$ in the $\boldsymbol{Q}_\mathrm{t}$ vector. This procedure leads to the modification of the $\mathbf{M}_1^*$ matrix in Eq. (4.16) which now becomes

$$ \mathbf{M}_1^* = \begin{bmatrix} \mathbf{J}^T\mathbf{M}\mathbf{J} & \mathbf{0} \\ \mathbf{M}_\mathrm{tm} & \mathbf{M}_\mathrm{t} \end{bmatrix} \tag{4.19}$$

where $\mathbf{M}_\mathrm{tm} \in \mathbb{R}^{6\times dim_{\ddot{\boldsymbol{q}}_\mathrm{m}}}$ and its only non-null block is given by $\mathbf{M}_\mathrm{tm}(1:3,1:3) = m_\mathrm{t}\mathbf{I}^{3\times 3}$.

The system formed by equations (4.16) and (4.17) constitutes a Differential-Algebraic Equations (DAE) system; from the solution standpoint, it would be more convenient to deal with a fully differential system. In order to achieve so, equation (4.17) is derived twice with respect to time to obtain $\ddot{\boldsymbol{\Phi}} = \mathbf{0}$. This is equivalent to imposing compatibility conditions on accelerations instead of positions; it is thus extremely important to have initial conditions (positions and velocities) which are

kinematically compatible, otherwise the grasp constraint will be violated regardless of the fact the accelerations compatibility relations are satisfied. This would result in a separation of the target object from the manipulator end-effectors. Nevertheless, even if the initial kinematic conditions are properly assigned, the resolution of the equations of motion is still highly prone to constraints violation. It is then desirable to implement a methodology capable of eliminating the constraints violations both at the position and velocity levels. The basic idea of this approach is to add corrective terms to the position and velocity vectors with the intent to satisfy the corresponding kinematic constraint equations. The adopted strategy is the Baumgarte Stabilization Method (BSM) [80]; the latter allows the constraints to be slightly violated before corrective actions take place. BSM introduces two feedback terms in the (differential) constraint equation leading to:

$$\ddot{\boldsymbol{\Phi}} + 2\alpha\dot{\boldsymbol{\Phi}} + \beta^2\boldsymbol{\Phi} = \mathbf{0} \tag{4.20}$$

where α and β are chosen as positive constants (their values are small and need to be properly tuned for the specific case under examination). Given the dependency of $\boldsymbol{\Phi}$ on $\boldsymbol{Q}$, Eq. (4.20) can be rewritten as

$$\mathbf{A}_{\text{cr}}\ddot{\boldsymbol{Q}} = \boldsymbol{B}_{\text{cr}} \tag{4.21}$$

where $\mathbf{A}_{\text{cr}} \in \mathbb{R}^{6\times dim_{\ddot{\boldsymbol{Q}}}}$ and $\boldsymbol{B}_{\text{cr}} \in \mathbb{R}^{6\times 1}$.

As a matter of fact, the constraints reactions represent an additional unknown of the problem. Equations (4.16) and (4.21) can be used to determine the $\boldsymbol{R}$ vector. From (4.16), one gets:

$$\ddot{\boldsymbol{Q}} = \mathbf{M}_1^{*-1}[\mathbf{M}_2^*\dot{\boldsymbol{Q}} + \boldsymbol{C}^* + \boldsymbol{F}^* + \mathbf{W}^*\boldsymbol{R} + \boldsymbol{u}^*] \tag{4.22}$$

Substituting equation (4.22) into (4.21), it is possible to calculate the constraints reactions:

$$\boldsymbol{R} = [\mathbf{A}_{\text{cr}}\mathbf{M}_1^{*-1}\mathbf{W}^*]^{-1}[\boldsymbol{B}_{\text{cr}} - \mathbf{A}_{\text{cr}}\mathbf{M}_1^{*-1}(\mathbf{M}_2^*\dot{\boldsymbol{Q}} + \boldsymbol{C}^* + \boldsymbol{F}^* + \boldsymbol{u}^*)] \tag{4.23}$$

Equation (4.23) is substituted back into Equation (4.16) which can now be integrated to compute the dynamics of the closed-loop system formed by the SMS and grasped target object.

4.2.1 Space Manipulator System and target object description

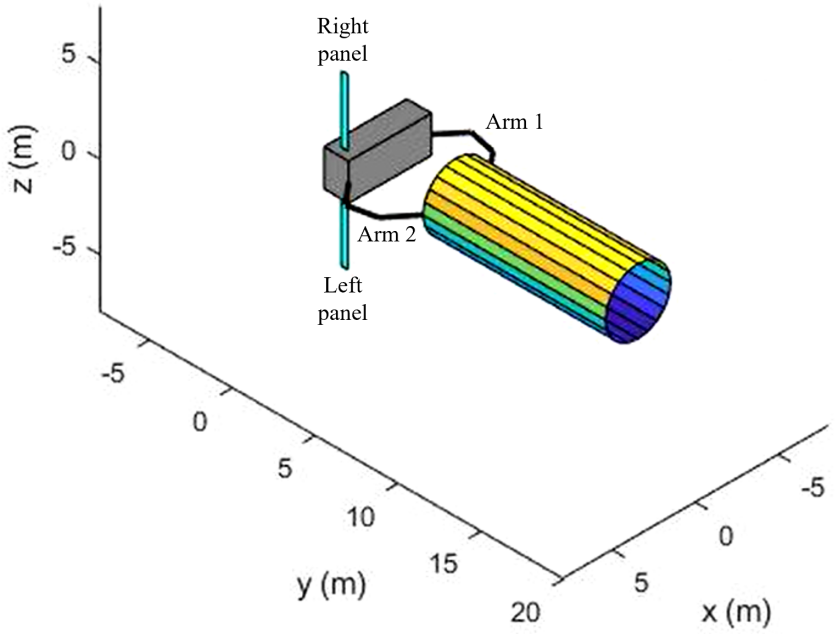

Figure 4.2. Schematic of the multi-body space manipulator and target object.

The schematic of the two-arm space manipulator (on the left) and the target object (on the right) is reported in Fig. 4.2. The former is constituted of a prismatic-shaped base platform having dimensions $5 \times 1.5 \times 2.2\,\mathrm{m}$, a mass of $m_B = 2550\,\mathrm{kg}$ and principal moments of inertia (with respect to its center of mass) equal to ${}^{B}_{O_B}I_{B_{xx}} = 632\,\mathrm{kg\,m^2}$, ${}^{B}_{O_B}I_{B_{yy}} = 4890\,\mathrm{kg\,m^2}$ and ${}^{B}_{O_B}I_{B_{zz}} = 4695\,\mathrm{kg\,m^2}$. Furthermore, the base is equipped with two 7-dof robotic arms. More specifically, each of them consists of seven links: the first six are connected by means of revolute joints (with each rotation axis oriented at 90° with respect to the previous one) and the last two use a prismatic joint (nevertheless, this joint will be blocked in the manipulation task being examined in the following). A rotational motor is present at each revolute joint. All the links are characterized by distributed structural flexibility features. Two elastic solar panels are also clamped to the base platform. Tables from 4.1 to 4.4 report the geometric, inertial and structural dynamics frequencies of the SMS links and solar panels. The first four vibration modes have been considered for both the links and solar panels and a modal damping factor of 0.01 has been set for all modes. The modes being considered are those of a cantilever plate for the solar panels and the ones of a free-free beam for the arms links. Shifting to the target object, this has a cylindrical shape of diameter 4 m and height 11 m. Furthermore,

Table 4.1. Manipulator links geometric and inertial properties.

Link n.	Length (m)	Mass (kg)
1	1.5	20
2	0.2	6
3	1.5	20
4	0.2	6
5	1.5	20
6	0.2	6
7	0.2	6

Table 4.2. Manipulator links natural frequencies.

Frequency n.	Value (Hz)	
	Long links	Short links
1	2.39	867.50
2	2.39	867.50
3	5.73	867.50
4	5.73	867.50

Table 4.3. Solar panels geometric and inertial properties.

Length	4 m
Height	0.4 m
Thickness	5×10^{-3} m
Mass	18.64 kg

Table 4.4. Solar panels natural frequencies.

Frequency n.	Value (Hz)
1	0.35
2	2.21
3	6.18
4	6.52

its mass is equal to $m_t = 2154\,\mathrm{kg}$ and principal moments of inertia (with respect to its center of mass) equal to ${}^{t}_{O_t}I_{t_{xx}} = 3 \times 10^3\,\mathrm{kg\,m^2}$, ${}^{t}_{O_t}I_{t_{yy}} = 2.8 \times 10^4\,\mathrm{kg\,m^2}$ and ${}^{t}_{O_t}I_{t_{zz}} = 2.8 \times 10^4\,\mathrm{kg\,m^2}$.

4.3 Adopted control strategy description

Two separate control strategies have been adopted to operate the manipulator robotic arms and the base platform. For what concerns the former, a Jacobian Transpose Control (JTC) has been chosen. Given a reference desired trajectory for the k-th arm end-effector defined with respect to the connection point between the base and the k-th arm itself, the consequent joint torques are given by

$$\boldsymbol{u}_{a_k} = -\mathbf{U}_{p_{EE}}\mathbf{J}^T_{EE_k}\boldsymbol{e}_{EE_k} - \mathbf{U}_{d_{EE}}\dot{\boldsymbol{\theta}}_{J_k}\,, \quad k = 1, 2 \tag{4.24}$$

where $\mathbf{U}_{p_{EE}}$ and $\mathbf{U}_{d_{EE}}$ are respectively a (diagonal) proportional and derivative gain matrix, $\mathbf{J}_{EE_k}$ is the end-effector Jacobian matrix (which allows to express the end-effector linear velocity in terms of the arm joint rates), $\boldsymbol{e}_{EE_k}$ is the deviation of the end-effector position from the desired one and $\dot{\boldsymbol{\theta}}_{J_k}$ are the arm joint rates. With respect to the reference trajectory, it has been chosen as a fourth order polynomial in time and its coefficients determined by imposing the desired initial position and velocity and final position, velocity and acceleration conditions for the end-effector (the desired initial conditions coincide with the actual initial ones while the final ones are set as the desired final location with null velocity and acceleration). Shifting to the base, a Proportional-Derivative Control (PDC) has been implemented for keeping the base linear and angular coordinates (and their time rates) at some desired values. The base PDC is given by

$$\boldsymbol{u}_B = -\mathbf{K}_{p_B}\boldsymbol{e}_B - \mathbf{K}_{d_B}\dot{\boldsymbol{e}}_B \tag{4.25}$$

Some further insight should be given to the attitude portion of the base control. The proportional part is formulated using quaternions in the following way: first, a quaternion ${}^{I}\boldsymbol{q}^{\mathrm{des}}_B$ corresponding to the desired attitude is defined; then, the following matrix built on it is created:

$${}^{I}\mathbf{Q}^{\mathrm{des}}_B = \begin{bmatrix} {}^{I}\boldsymbol{q}^{\mathrm{des}}_B(1) & {}^{I}\boldsymbol{q}^{\mathrm{des}}_B(2) & {}^{I}\boldsymbol{q}^{\mathrm{des}}_B(3) & {}^{I}\boldsymbol{q}^{\mathrm{des}}_B(4) \\ -{}^{I}\boldsymbol{q}^{\mathrm{des}}_B(2) & {}^{I}\boldsymbol{q}^{\mathrm{des}}_B(1) & {}^{I}\boldsymbol{q}^{\mathrm{des}}_B(4) & -{}^{I}\boldsymbol{q}^{\mathrm{des}}_B(3) \\ -{}^{I}\boldsymbol{q}^{\mathrm{des}}_B(3) & -{}^{I}\boldsymbol{q}^{\mathrm{des}}_B(4) & {}^{I}\boldsymbol{q}^{\mathrm{des}}_B(1) & {}^{I}\boldsymbol{q}^{\mathrm{des}}_B(2) \\ -{}^{I}\boldsymbol{q}^{\mathrm{des}}_B(4) & {}^{I}\boldsymbol{q}^{\mathrm{des}}_B(3) & -{}^{I}\boldsymbol{q}^{\mathrm{des}}_B(2) & {}^{I}\boldsymbol{q}^{\mathrm{des}}_B(1) \end{bmatrix} \tag{4.26}$$

Then, the vector ${}^I\tilde{\boldsymbol{q}}_B = {}^I\mathbf{Q}_B^{\text{des}\,I}\boldsymbol{q}_B$ is defined and, finally, $\boldsymbol{e}_B(4:6) = \text{sign}({}^I\boldsymbol{q}_B(1)){}^I\tilde{\boldsymbol{q}}_B(2:4)$. For what concerns the derivative portion, $\dot{\boldsymbol{e}}_B(4:6) = {}^B_I\boldsymbol{\omega}_B - {}^B_I\boldsymbol{\omega}_B^{\text{des}}$ where ${}^B_I\boldsymbol{\omega}_B^{\text{des}}$ is the desired base angular velocity.

Eqs.(4.24) and (4.25) need to be substituted into Eq. (4.16) together with the appropriate mapping matrices $\mathbf{B}_i$.

4.4 Case study and numerical results

4.4.1 Case study description

The case study being here analyzed concerns the docking maneuver of the target object described above onto the SMS base platform. As initial condition, the robotic arms are deployed and the grasp of the target on its external surface has been performed. Both manipulator and target are initially at rest with respect to the inertial frame. Different dynamics models for the SMS and controls will be tested and compared, namely:

- Rigid model with JTC and full PDC;
- Flexible model with JTC and full PDC;
- Flexible model with JTC and PDC only on the base attitude;
- Flexible model with JTC and no PDC.

It has to be underlined the JTC will be synthesized considering a rigid model for the SMS in all the cited cases. A maneuver duration of 20 minutes has been considered.

4.4.2 Numerical results

It has been earlier stated an ECI inertial reference frame has been assumed within the general dynamics model development. Nevertheless, an inertial system which has its origin at the position of the SMS base center of mass at $t = 0$ has been considered in the following simulations. Rigorously speaking, this should be an orbital reference frame (relative, for example, to the orbit on which the base center of mass is moving before the beginning of the considered maneuver) which is not inertial; nevertheless, in the case study here presented, the orbital angular velocity is assumed to be negligible with respect to the maneuver time scale and this justifies neglecting the orbital curvature and to consider the orbital motion

as uniform rectilinear thus allowing one to classify the reference frame as inertial. Furthermore, the gravitational actions are coherently excluded as well.

In the following, the desired position for the two end-effectors is located 0.5 m above the corresponding arm connection point with the base platform (also referred to as the arm shoulder). Furthermore, the base is controlled in order to maintain its initial position and attitude with respect to the inertial reference frame (i.e. its center of mass has to remain in the origin of the inertial frame and its body-axes parallel to the inertial ones). Going into more detail, for what concerns the JTC, a trajectory tracking duration of 10 minutes has been chosen; after that, a set-point JTC intervenes (by that meaning the tracking final desired conditions are kept fixed as desired ones for the rest of the maneuver). Shifting to the PDC, a set-point control embedding the above-cited desired conditions has been adopted. Furthermore, the initial joint angles configuration and desired final end-effectors locations are such that the docking maneuver is ideally planar.

Figures from 4.3 to 4.9 show significant quantities being compared for the rigid

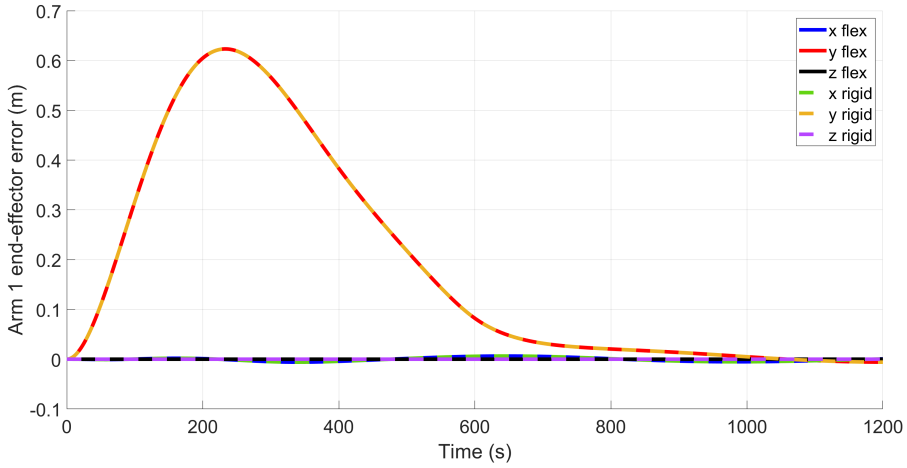

Figure 4.3. Arm 1 end-effector error (rigid vs. flexible model).

and flexible models when JTC and full PDC are implemented. It can be noticed how there's a practically complete overlapping between all the curves relating to the rigid case and the corresponding flexible ones. Comparing the two end-effector errors (Figs. 4.3,4.4), some differences in the y coordinate curves can be observed. Nevertheless, both end-effectors converge to their respective desired positions. It should also be remarked the initial error is zero since the initial desired condition for the end-effectors has been imposed to be equal to the actual one in the polynomial trajectory coefficients calculation. Fig. 4.5 shows the base platform center of mass

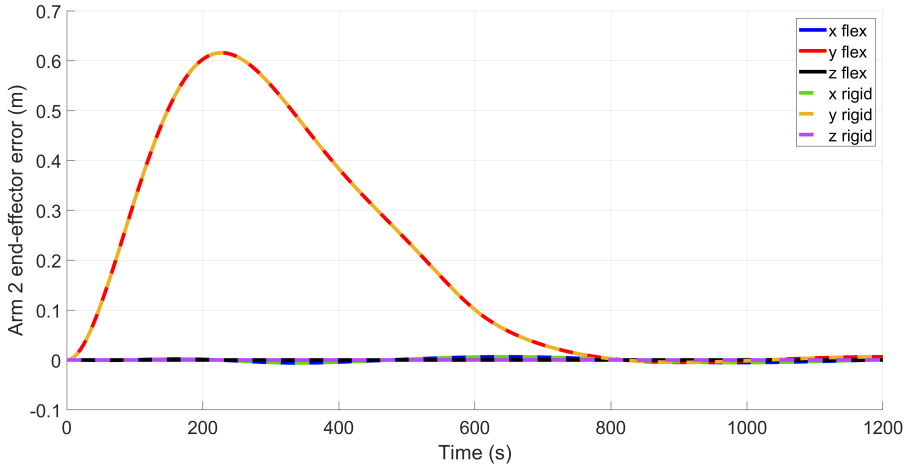

Figure 4.4. Arm 2 end-effector error (rigid vs. flexible model).

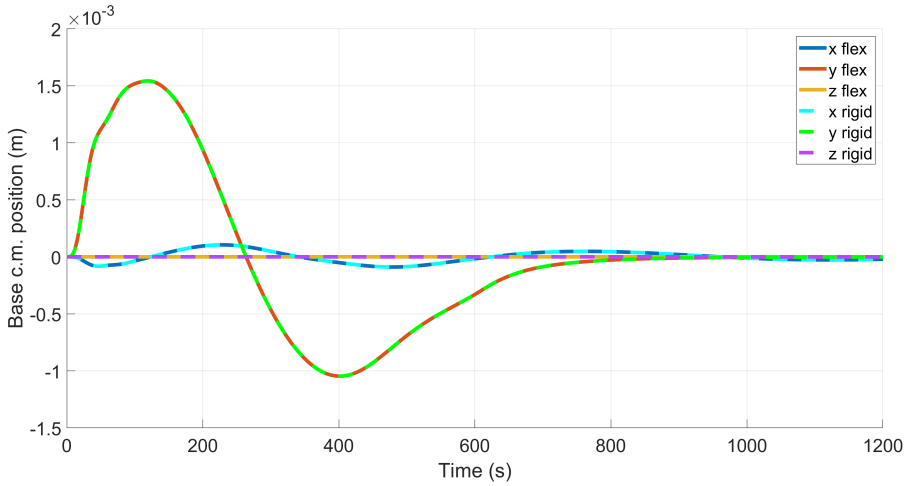

Figure 4.5. Base center of mass position (rigid vs. flexible model).

displacement components are of the order of millimeters with a dominant component along the y inertial axis (as it was to be expected given the SMS configuration and the maneuver being performed). Fig. 4.6 displays the base Euler yaw angle being extremely limited in variation (less than a 0.5° peak-to-peak variation). The pitch and roll angles haven't been reported as their values were negligible. Figs. 4.7,4.8 show the arms joint torques and how they converge to zero as the end-effectors gradually reach the desired locations. The torque values required to the motors are totally compatible with the available hardware for space use. Fig. 4.9 displays the z body component of the base control torque (the other two are once again omitted as their values were not significant). Here too the required actions are compatible with available attitude control systems hardware (e.g. reaction wheels and control

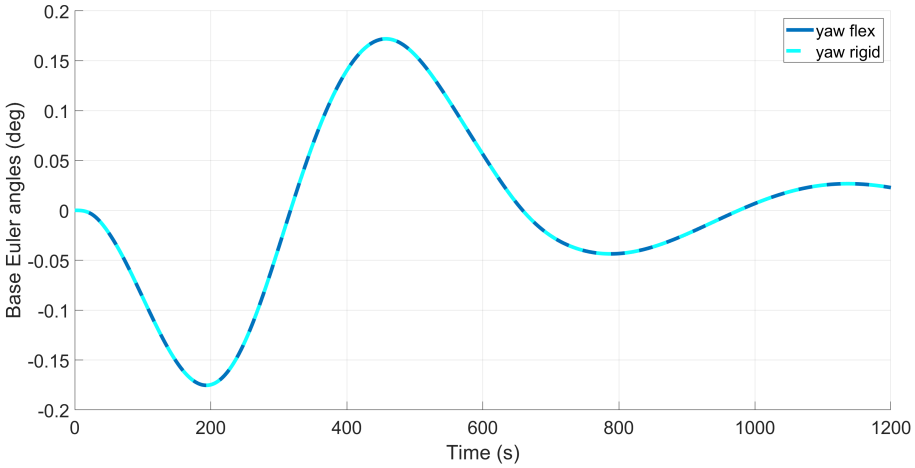

Figure 4.6. Base attitude with respect to the inertial frame (rigid vs. flexible model).

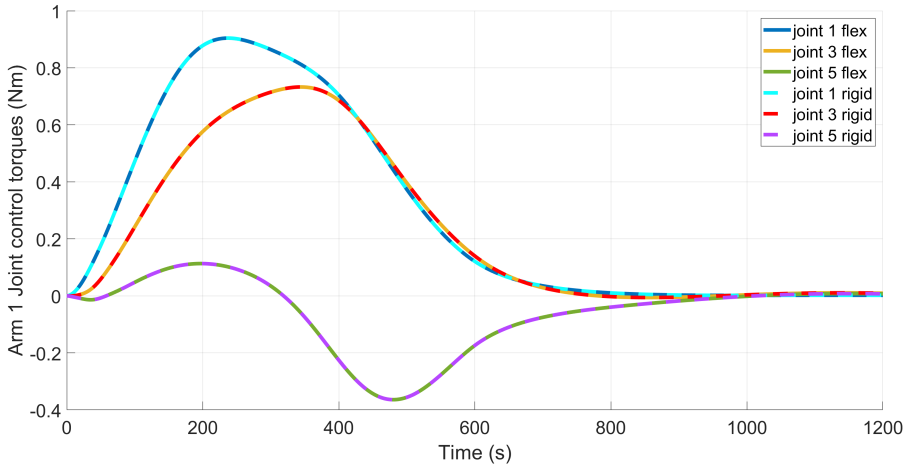

Figure 4.7. Arm 1 control torques (rigid vs. flexible model).

moment gyros). We now proceed to compare results only considering the flexible model and analyzing the performance obtained by using the different PDC variants described above. Figs. 4.11 and 4.12 (respectively referring to only attitude PDC and no PDC) substantially exhibit the same qualitative and quantitative behavior; on the other hand, Fig. 4.10 (which is the one related to the full PDC) shows a slightly different trend for the x component of the error and the peak value for the y component is considerably smaller with respect to the other two cases. With this said, all three plots show convergence of the error to a zero value. The corresponding graphs for the second arm display the same results typology and are not reported for the sake of brevity. For what concerns the base attitude variation, all three PDC variants lead to angles which are below 2 deg (see Figs. 4.13-4.15). Focusing the

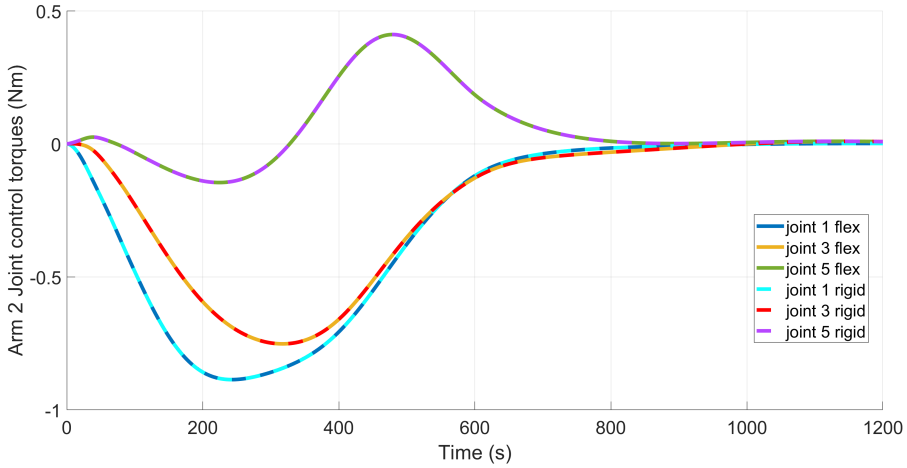

Figure 4.8. Arm 2 control torques (rigid vs. flexible model).

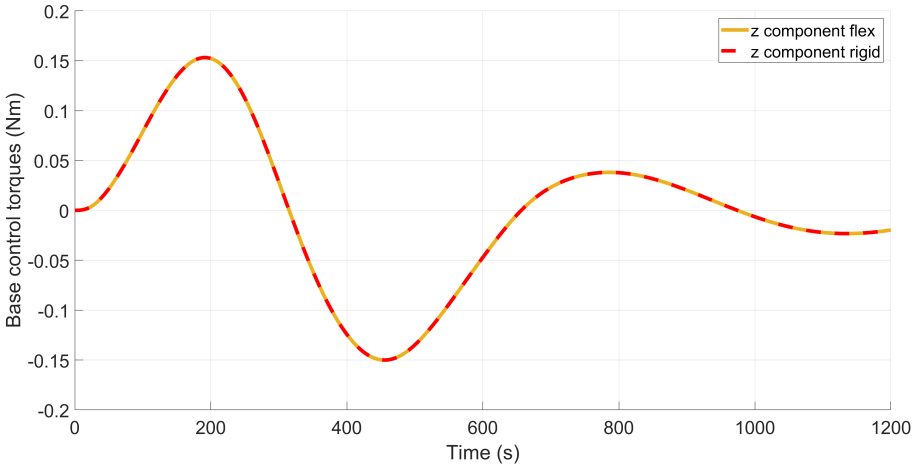

Figure 4.9. Base control torques (rigid vs. flexible model).

attention on the yaw angle (which is the only one characterized by non-negligible values), its behavior is quite different in the three analyzed cases; it can be observed how, in the first part of the maneuver, the full and attitude-only PDC display the same qualitative behavior (although the second one leads to values which are one order of magnitude smaller than those of the first one), while, in the second part, the former is not able to totally damp out the oscillations, but the second one is. In the case of no PDC, the base yaw angle has a monotone trend stabilizing itself on a value of about 1.5 deg, which is the highest among the three cases (as it was to be expected). Figures from 4.16 to 4.18 report the base center of mass position coordinates. The full PDC is capable of maintaining the displacement components at the order of millimeters, while in the other two cases they are of the

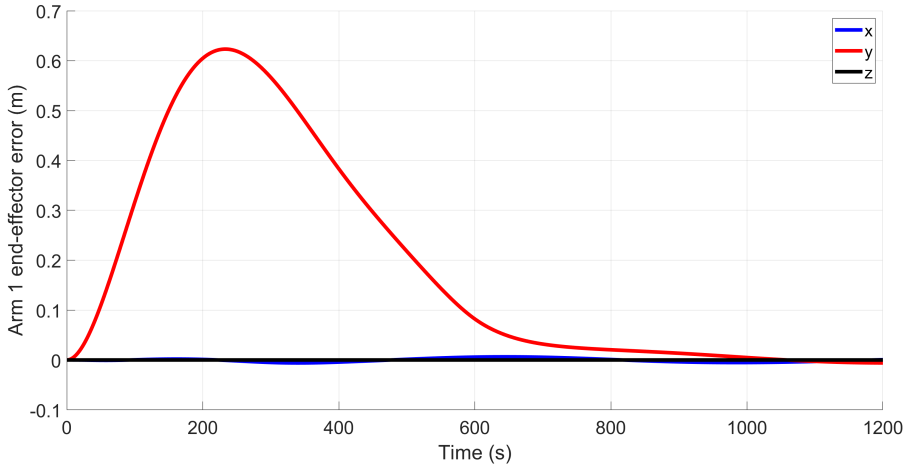

Figure 4.10. Arm 1 end-effector error (flexible model and full base control).

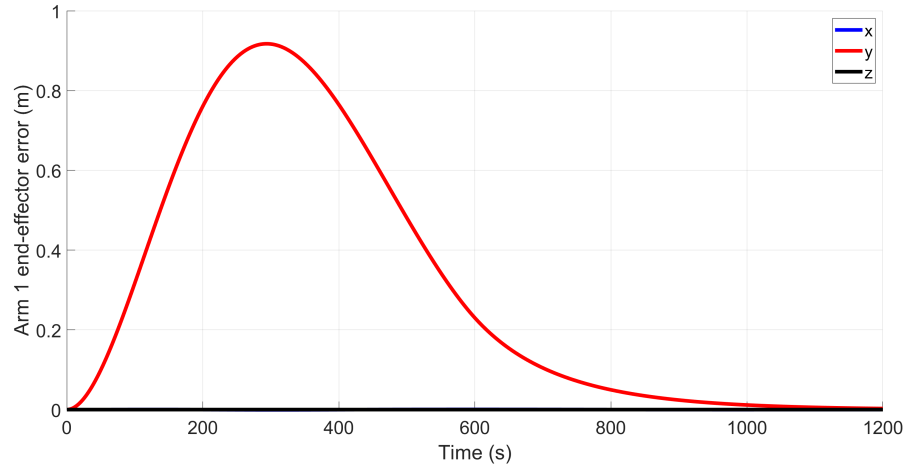

Figure 4.11. Arm 1 end-effector error (flexible model and base attitude control).

order of the meter. This situation is once again to be expected as the full PDC is the only variant out of the three in which the base position is controlled. The case of attitude-only and no PDC display almost the same y displacement component, but there's a noticeable difference on the x component being practically zero for the former and roughly 8 cm for the latter. It has to be underlined that, in the first case, the manipulator arms control is required to exert the entire effort in order to bring the target towards the base since the latter is controlled to remain fixed at its initial position; on the contrary, in the second and third cases, given the base translation motion is not impeded, there can be a reciprocal approach between the base and target. Figures from 4.19 to 4.21 show the left solar panel modal amplitudes. The order of magnitude is the same in all three cases; nevertheless, the trends are quite

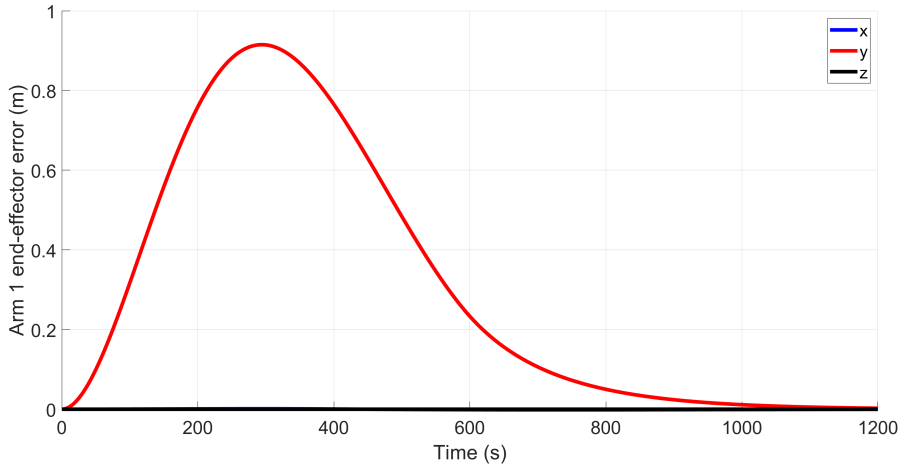

Figure 4.12. Arm 1 end-effector error (flexible model and no base control).

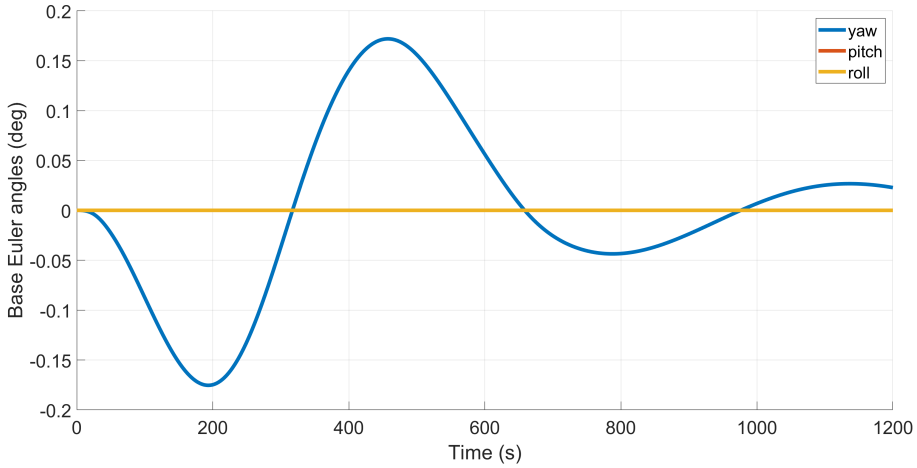

Figure 4.13. Base attitude with respect to the inertial frame (flexible model and full base control).

different, namely the peak value tends to increase and the oscillations are damped more slowly as the base is less controlled. Furthermore, it can be noticed how the mode being mainly excited is the first one for all cases. The graphs concerning the right solar panel give the same typology of information and are not reported for the sake of brevity. In order to give a visual representation to the evolution of the system when the different control strategies are implemented, Figs. 4.22 and 4.23 respectively show what happens when JTC+Full PDC and the only JTC are applied to the SMS confirming what has been described throughout the present section. The figures also display how the relative attitude between the SMS base platform and target is maintained fixed throughout the maneuver; this is a relevant

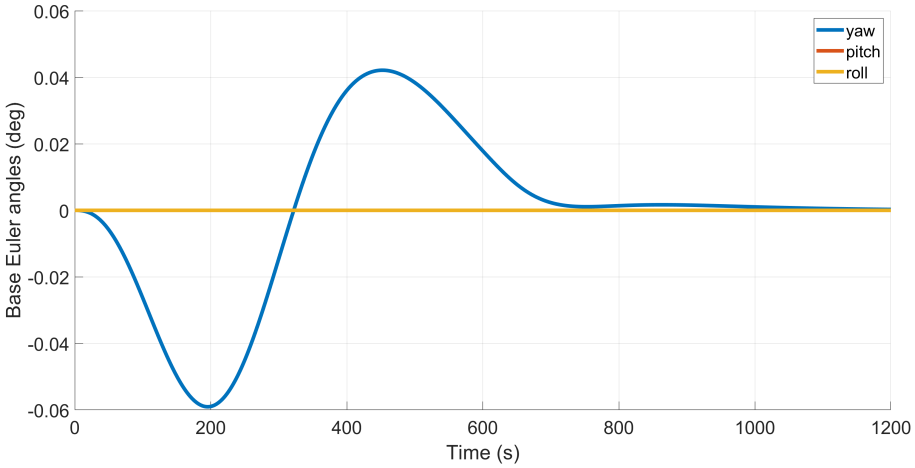

Figure 4.14. Base attitude with respect to the inertial frame (flexible model and base attitude control).

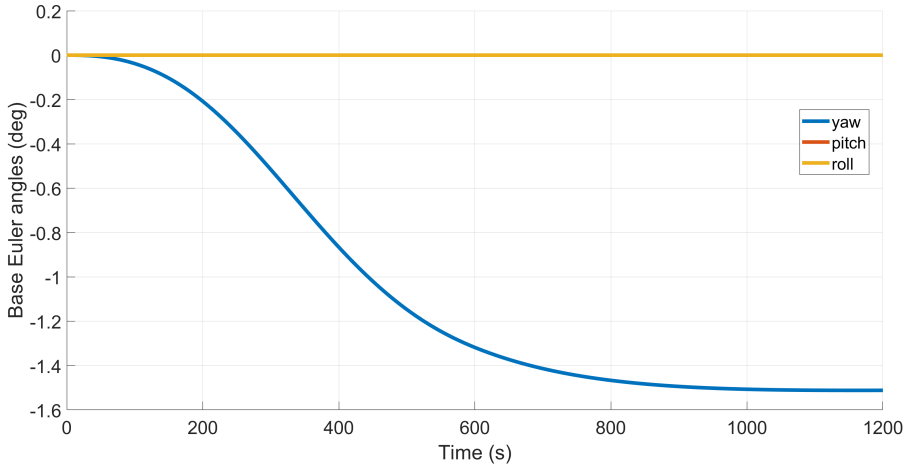

Figure 4.15. Base attitude with respect to the inertial frame (flexible model and no base control).

aspect as well given the stringent mechanical tolerances which may characterize the docking interfaces present on both SMS and target.

Now a second scenario is taken into consideration where the initial state and final desired conditions for the closed-loop system are the same as the previous case except for the fact the arms initial configuration does not allow for the docking maneuver to be planar. As a consequence, the relative attitude between the SMS base and target is not kept fixed at the initial state (which is the one desired for the docking maneuver to take place) on a general basis. In order to overcome this issue, a modified version of the above adopted control strategy has been formulated and will now be described. The major difference concerns the base control; indeed,

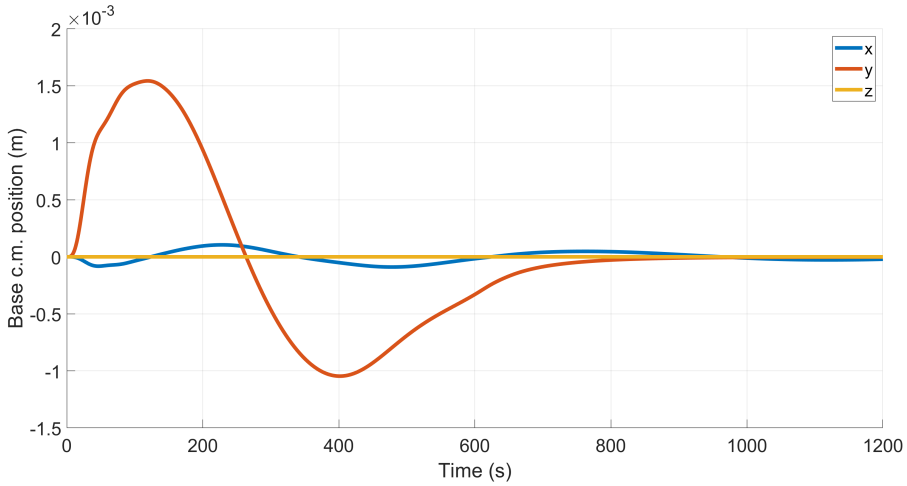

Figure 4.16. Base center of mass position (flexible model and full base control).

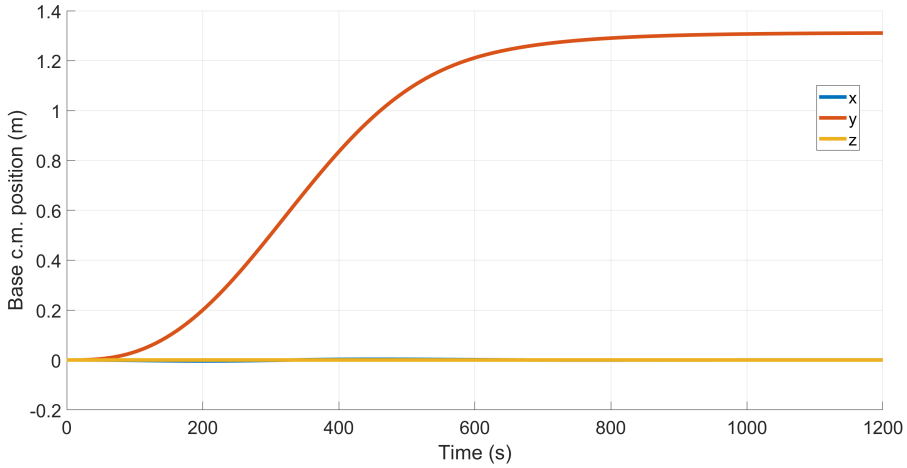

Figure 4.17. Base center of mass position (flexible model and base attitude control).

in the effort of trying to maintain the relative attitude between the SMS base and target, the former is controlled in order for it to be synchronous to the latter as far as the rotational motion is concerned. From the mathematical standpoint, a matrix ${}^{I}\mathbf{Q}_{t0}$ is first defined:

$$
{}^{I}\mathbf{Q}_{t0} = \begin{bmatrix} {}^{I}\boldsymbol{q}_{t0}(1) & {}^{I}\boldsymbol{q}_{t0}(2) & {}^{I}\boldsymbol{q}_{t0}(3) & {}^{I}\boldsymbol{q}_{t0}(4) \\ -{}^{I}\boldsymbol{q}_{t0}(2) & {}^{I}\boldsymbol{q}_{t0}(1) & {}^{I}\boldsymbol{q}_{t0}(4) & -{}^{I}\boldsymbol{q}_{t0}(3) \\ -{}^{I}\boldsymbol{q}_{t0}(3) & -{}^{I}\boldsymbol{q}_{t0}(4) & {}^{I}\boldsymbol{q}_{t0}(1) & {}^{I}\boldsymbol{q}_{t0}(2) \\ -{}^{I}\boldsymbol{q}_{t0}(4) & {}^{I}\boldsymbol{q}_{t0}(3) & -{}^{I}\boldsymbol{q}_{t0}(2) & {}^{I}\boldsymbol{q}_{t0}(1) \end{bmatrix} \tag{4.27}
$$

where ${}^{I}\boldsymbol{q}_{t0}$ is the initial target quaternions vector. Then, the vector ${}^{I}\tilde{\boldsymbol{q}}_{tB0} = {}^{I}\mathbf{Q}_{t0}\boldsymbol{q}_{B0}$

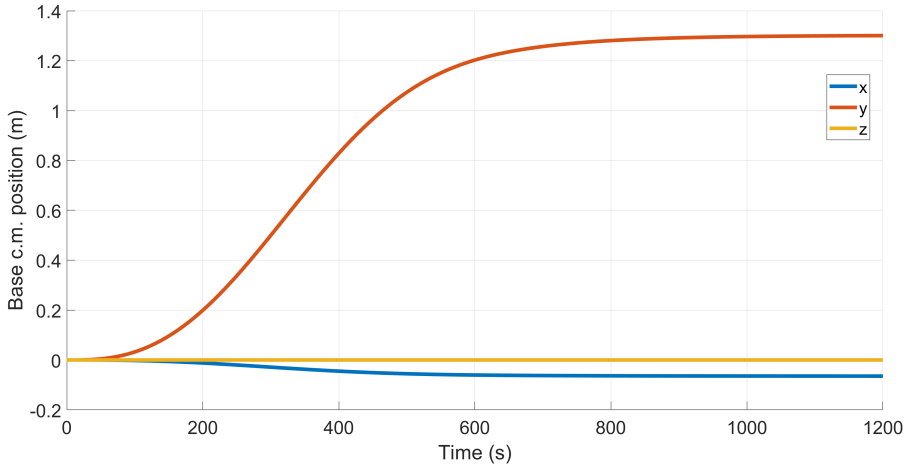

Figure 4.18. Base center of mass position (flexible model and no base control).

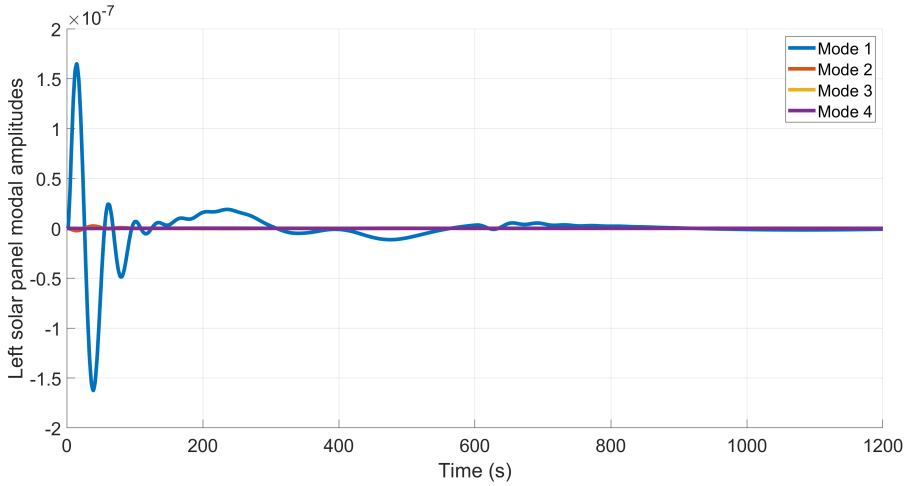

Figure 4.19. Left solar panel modal amplitudes (flexible model and full base control).

(where ${}^{I}\boldsymbol{q}_{B0}$ is the initial SMS base quaternions vector) is introduced representing the initial relative attitude (in terms of quaternions) between target and base platform which will be the desired one. Furthermore, ${}^{I}\tilde{\boldsymbol{q}}_{tB}$ is the same quantity varying with time. Also, the desired angular velocity for the base is set to be equal to that of the target (expressed in the base body frame). The base translational control is set to be null, while the attitude part is equal to

$$\boldsymbol{u}_{B_{\text{att}}} = -k_{p_{B_{\text{r}}}}({}^{I}\tilde{\boldsymbol{q}}_{tB}(2:4) - {}^{I}\tilde{\boldsymbol{q}}_{tB0}(2:4)) - k_{d_{B_{\text{r}}}}({}^{B}_{I}\boldsymbol{\omega}_{B} - {}^{B}_{I}\boldsymbol{\omega}^{\text{des}}_{B}) \tag{4.28}$$

where ${}^{B}_{I}\boldsymbol{\omega}^{\text{des}}_{B} = {}^{I}\mathbf{T}^{TI}_{B}\mathbf{T}^{t}_{tI}\boldsymbol{\omega}_{t}$. The arms Jacobian Transpose Control is the same as the previous case.

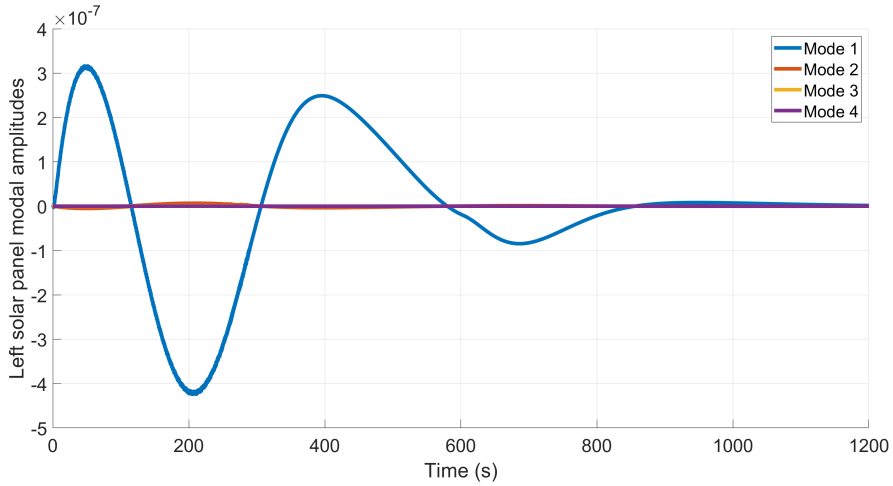

Figure 4.20. Left solar panel modal amplitudes (flexible model and base attitude control).

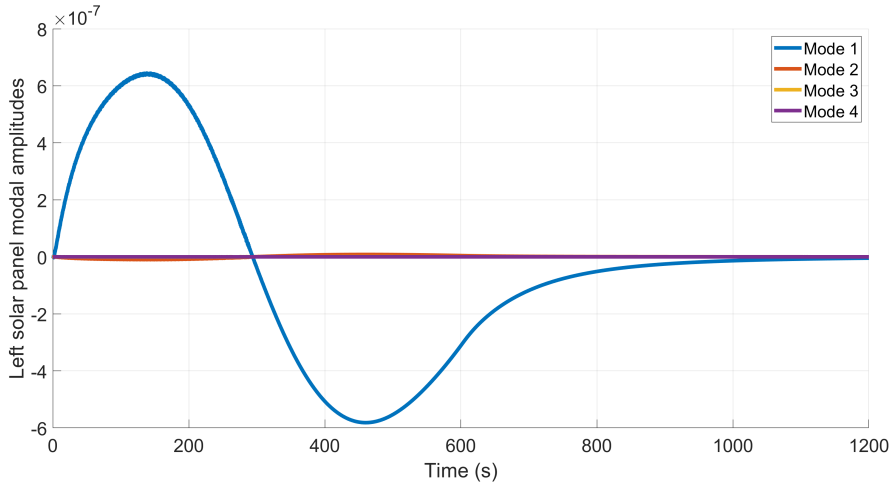

Figure 4.21. Left solar panel modal amplitudes (flexible model and no base control).

Nevertheless, adopting this type of control strategy entails that, on a general basis, the system formed by the SMS and target object will be spinning throughout the docking maneuver while, on the contrary, it could be helpful to have a null angular velocity of the closed-loop chain with respect to the inertial frame while keeping the desired relative attitude before mechanically joining the target to the SMS. To achieve this goal, an overall maneuver duration of 40 minutes has been considered. The de-spinning maneuver, performed by applying a purely derivative de-spinning control torque to the SMS base, will begin for $t > 10\,\text{min}$ (which is the JTC trajectory tracking time duration as earlier defined) whenever the norm of the error in position for both end-effectors goes below a user-defined small value (in the following, this tolerance has been set equal to 10 cm) for the first time. The torque

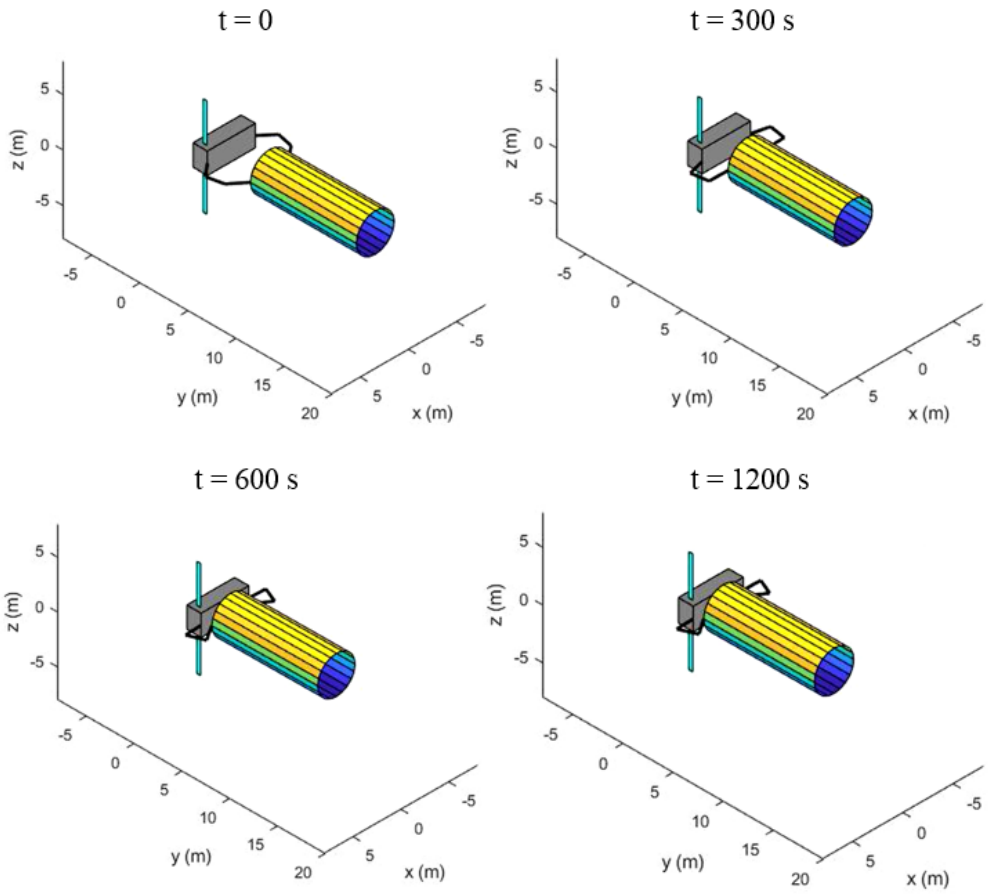

Figure 4.22. Evolution of the system when JTC and full PDC are applied.

has the following form:

$$\boldsymbol{u}_{B_{\text{att}}} = -k_{d_{B_{\text{r}}}} {}^{B}_{I}\boldsymbol{\omega}_{B} \tag{4.29}$$

The JTC will keep being active for the entire maneuver duration. Figs. 4.24 and 4.25 show how the base platform is synchronized to the target rotational motion from $t = 0$ until $t = 1721\,\text{s}$ when the de-spinning maneuver begins and how the reduction of the angular velocities of both bodies to practically zero is quite fast given the chosen control gains. Figs. 4.26 and 4.27 show the end-effectors position error; both of them are converging towards a zero error condition which would have been completely reached by further increasing the maneuver time duration. Fig. 4.28 reports the control torques required to the SMS base attitude control system clearly showing (by means of the sharp variation) the time instant in which the de-spinning maneuver begins. The required values fall within acceptable ranges. Figs. 4.29 and 4.30 show the arms joint torques: both plots indicate how the required control

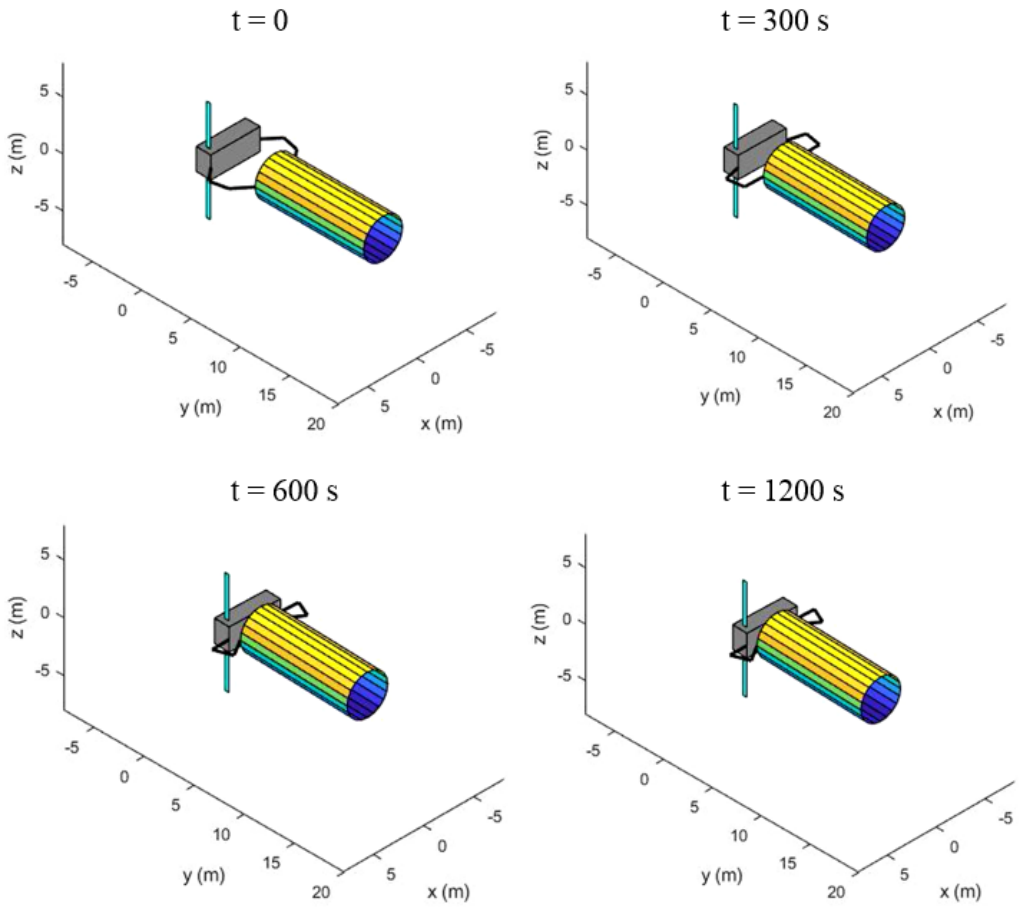

Figure 4.23. Evolution of the system when JTC and no PDC are applied.

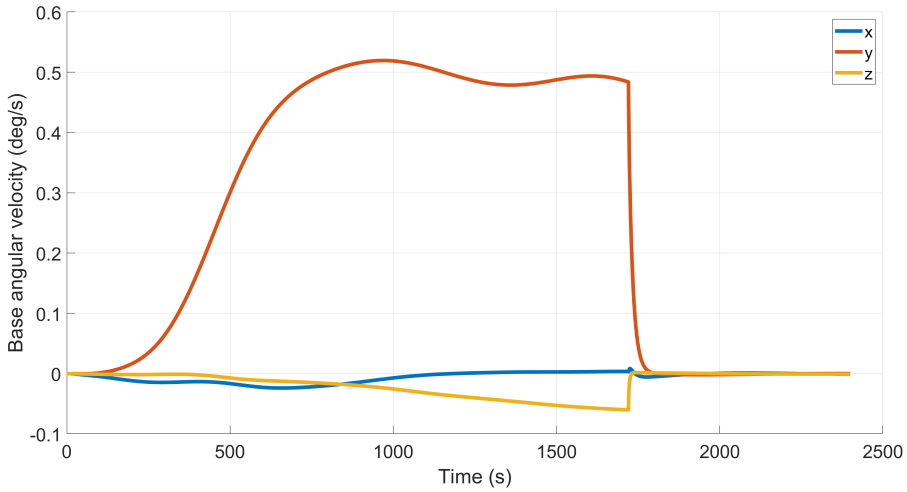

Figure 4.24. Base angular velocity with respect to the inertial frame and expressed in the same one (flexible model and de-spinning maneuver).

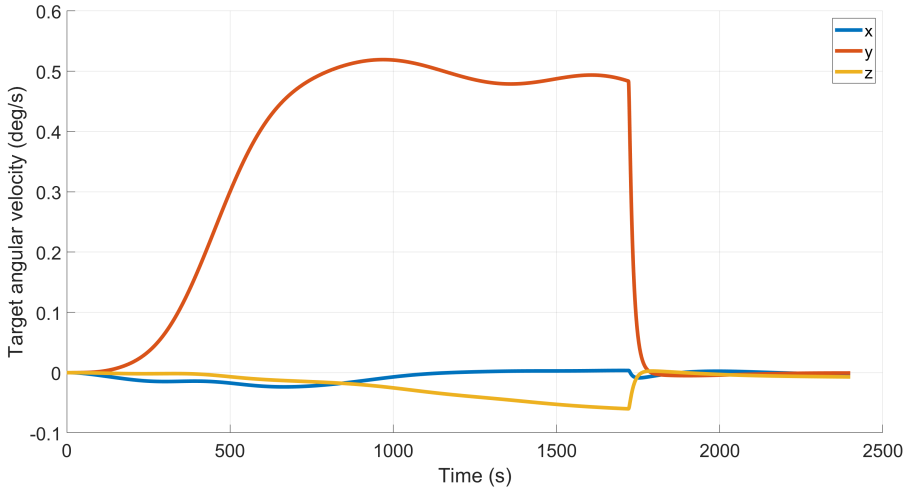

Figure 4.25. Target angular velocity with respect to the inertial frame and expressed in the same one (flexible model and de-spinning maneuver).

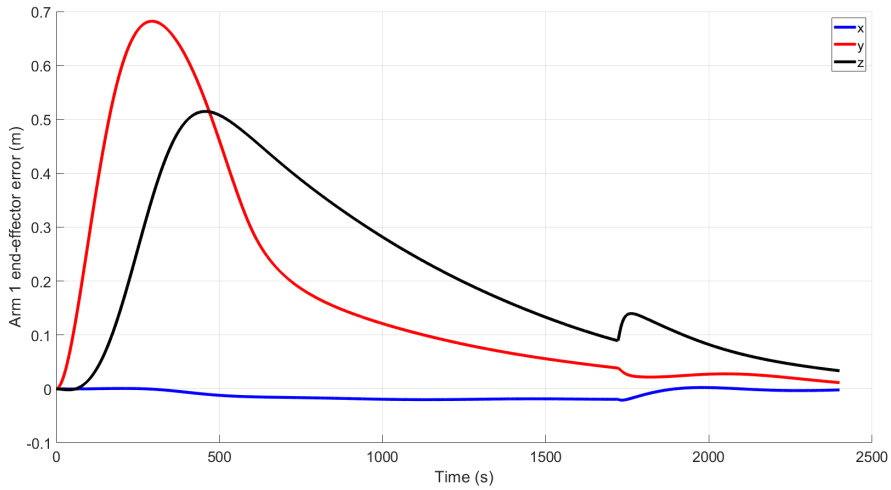

Figure 4.26. Arm 1 end-effector error (flexible model and de-spinning maneuver).

converges to zero values as the end-effectors position errors converge to zero. Once again, the spikes in the curves are an index of the change in the base control typology.

Figs. 4.31 and 4.32 imply elastic displacements (obtained considering both modal amplitudes calculated through the elastic equations integration and modes derived from MSC Nastran) for the solar panels which are four orders of magnitude higher with respect to those seen in the previous case, but still of the order of millimeters (thus being acceptable for the structure). The mode being mainly excited is again the first one as before. Figures from 4.33 to 4.38 show the arms long links modal amplitudes. The corresponding elastic displacements are of the sub-millimeter

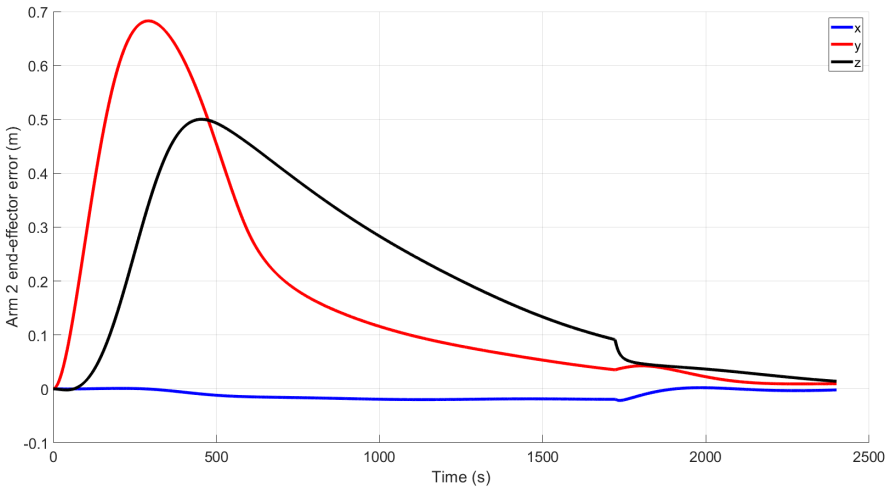

Figure 4.27. Arm 2 end-effector error (flexible model and de-spinning maneuver).

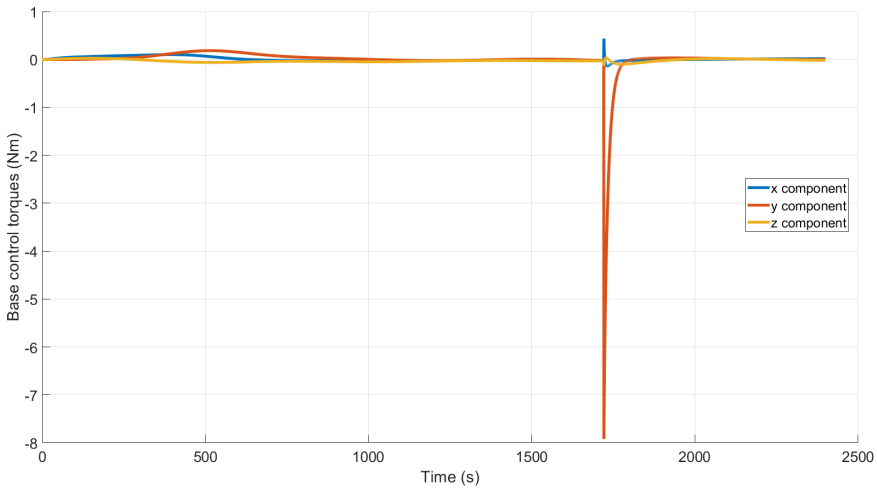

Figure 4.28. Base control torques expressed in the base body frame (flexible model and de-spinning maneuver).

order. The short links elastic displacements have been checked to be of the same order as well. Figs. 4.39 and 4.40 graphically visualize the evolution of the system confirming how the de-spinning maneuver is effective while maintaining the desired relative attitude between the SMS base and target object.

4.5 Conclusions

In the present chapter the dynamics model of a closed-loop multi-body system formed by a space manipulator and a target object has been presented and developed.

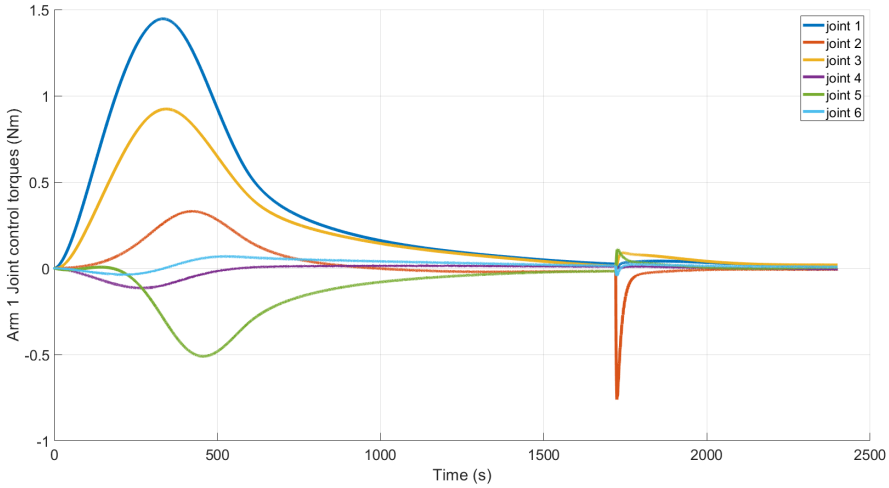

Figure 4.29. Arm 1 control torques (flexible model and de-spinning maneuver).

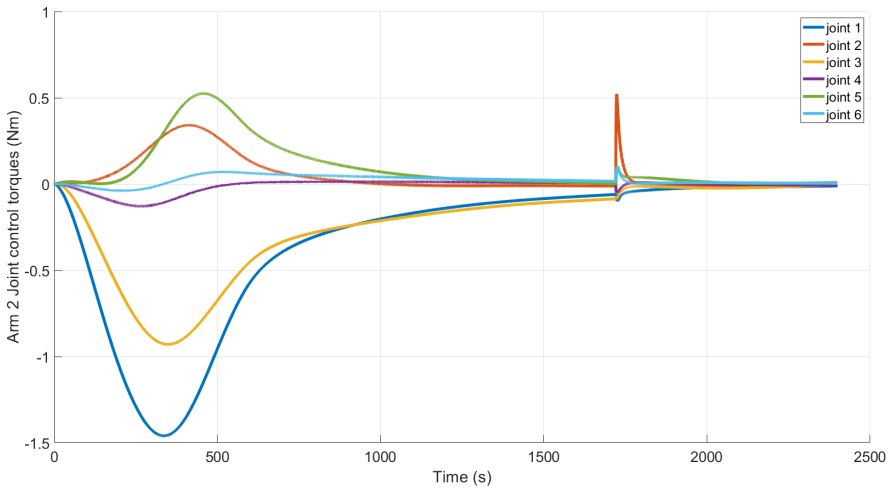

Figure 4.30. Arm 2 control torques (flexible model and de-spinning maneuver).

Both rigid and fully flexible models have been considered and implemented. The attention has been focused on the accomplishment of an autonomous docking maneuver to be performed by the space manipulator on the target object. A suitable control strategy combining Jacobian Transpose and Proportional-Derivative Controls (including different possible variants) for mission accomplishment has been studied and synthesized and its effectiveness positively evaluated comparing the results obtained for different dynamic models and initial system configurations.

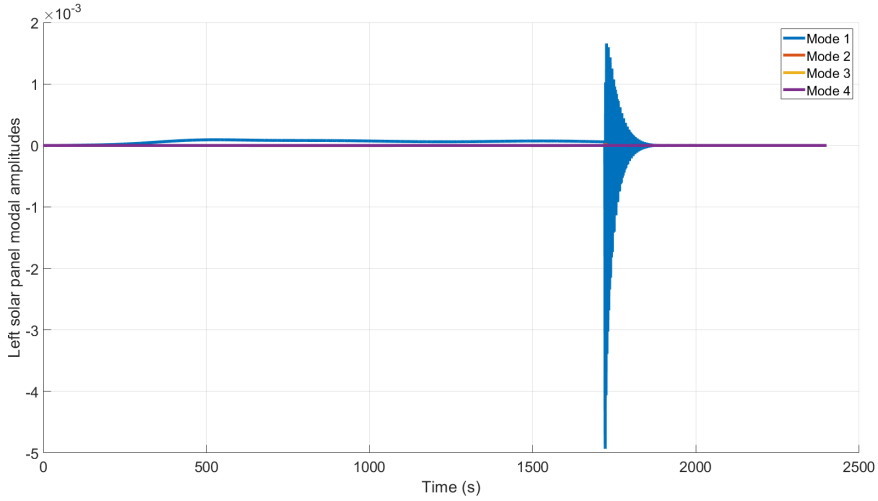

Figure 4.31. Left solar panel modal amplitudes (flexible model and de-spinning maneuver).

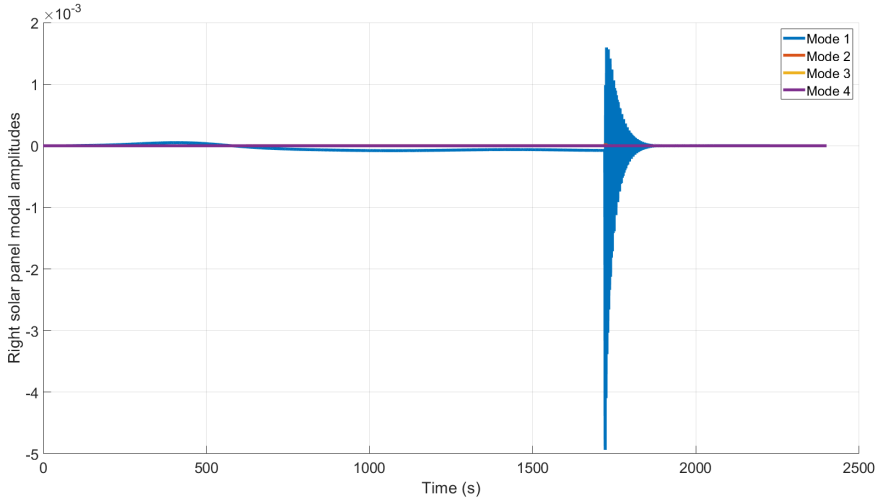

Figure 4.32. Right solar panel modal amplitudes (flexible model and de-spinning maneuver).

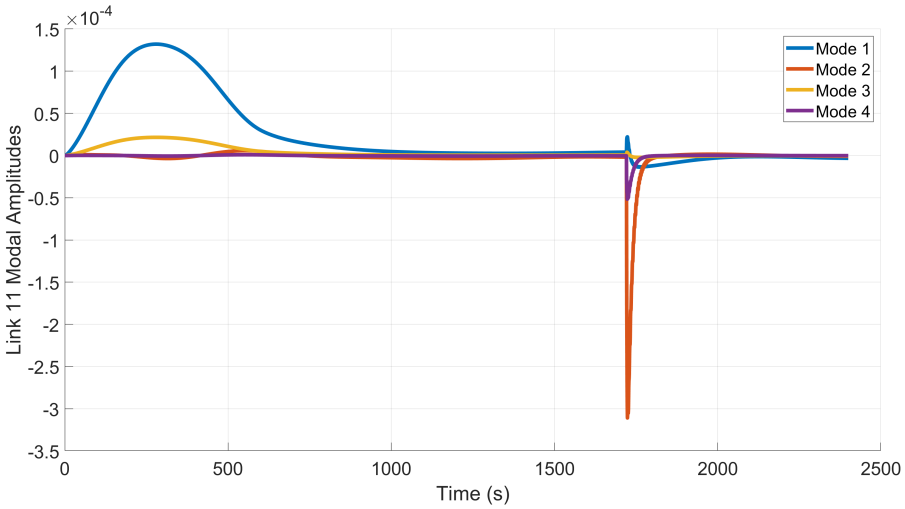

Figure 4.33. Link 11 modal amplitudes (flexible model and de-spinning maneuver).

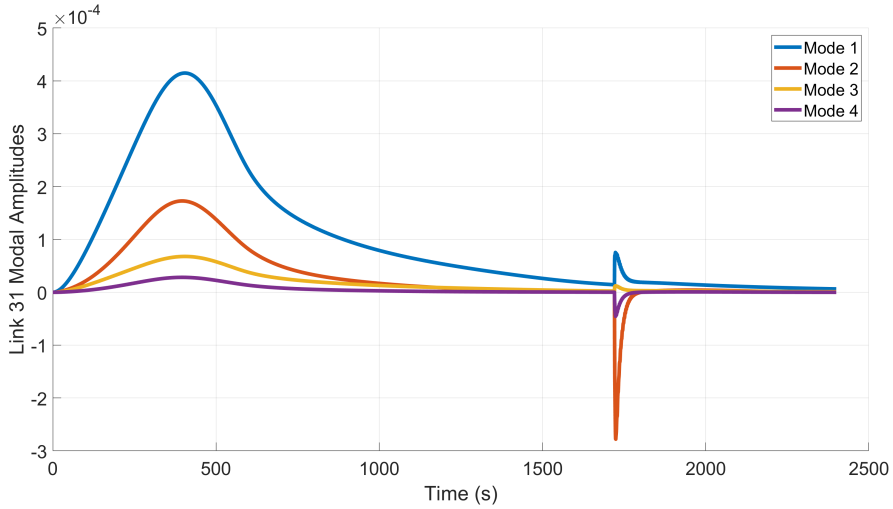

Figure 4.34. Link 31 modal amplitudes (flexible model and de-spinning maneuver).

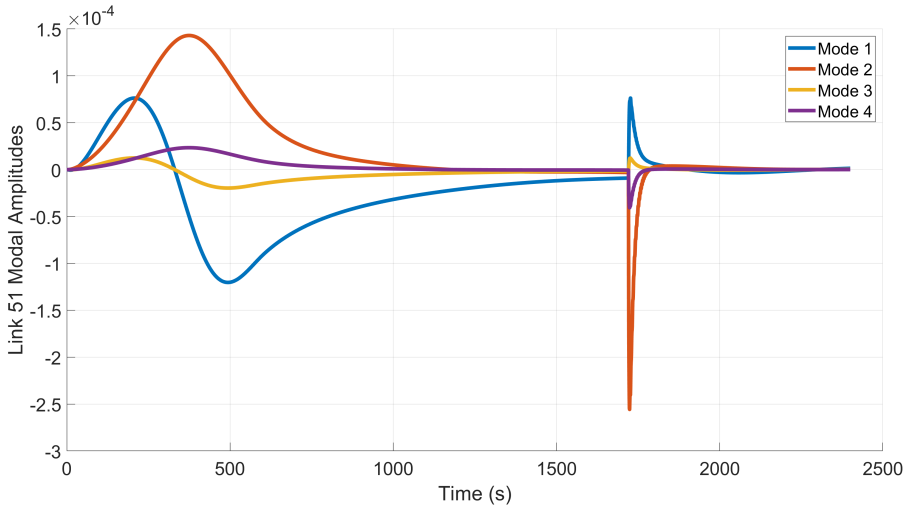

Figure 4.35. Link 51 modal amplitudes (flexible model and de-spinning maneuver).

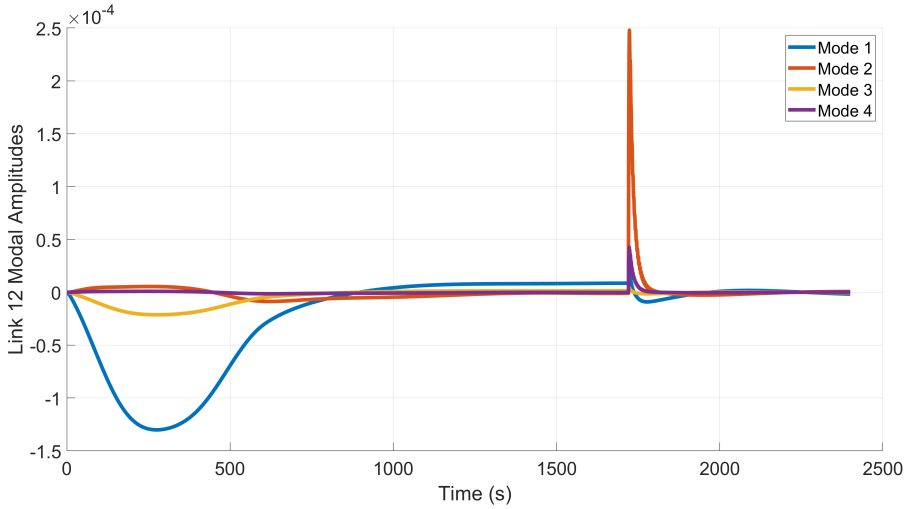

Figure 4.36. Link 12 modal amplitudes (flexible model and de-spinning maneuver).

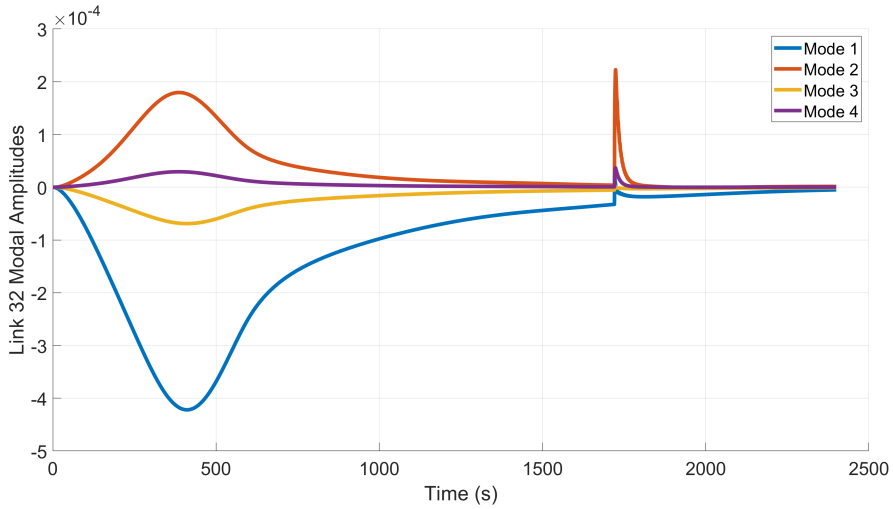

Figure 4.37. Link 32 modal amplitudes (flexible model and de-spinning maneuver).

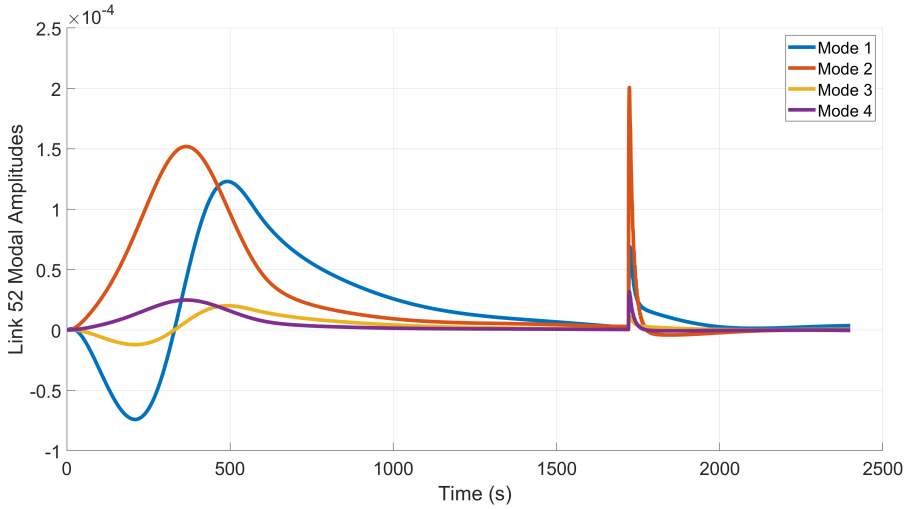

Figure 4.38. Link 52 modal amplitudes (flexible model and de-spinning maneuver).

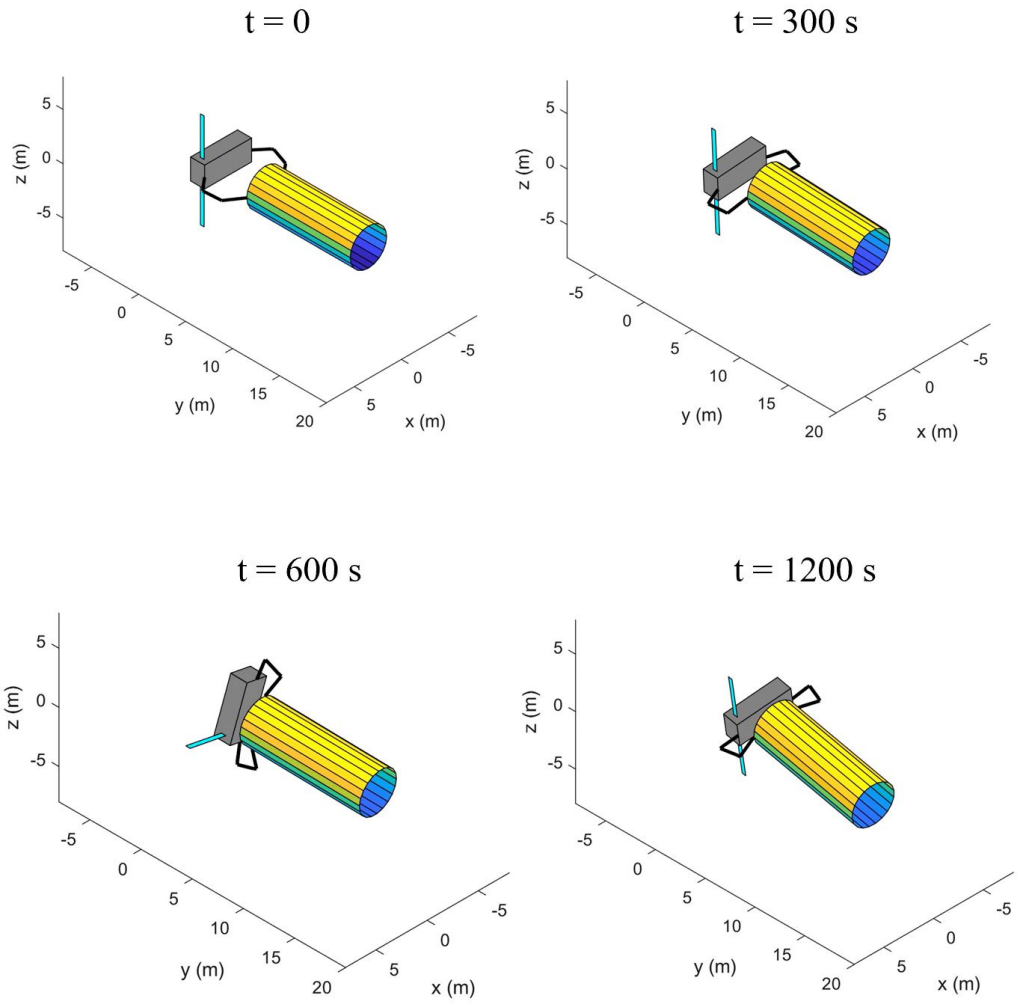

Figure 4.39. Evolution of the system when performing the de-spinning maneuver.

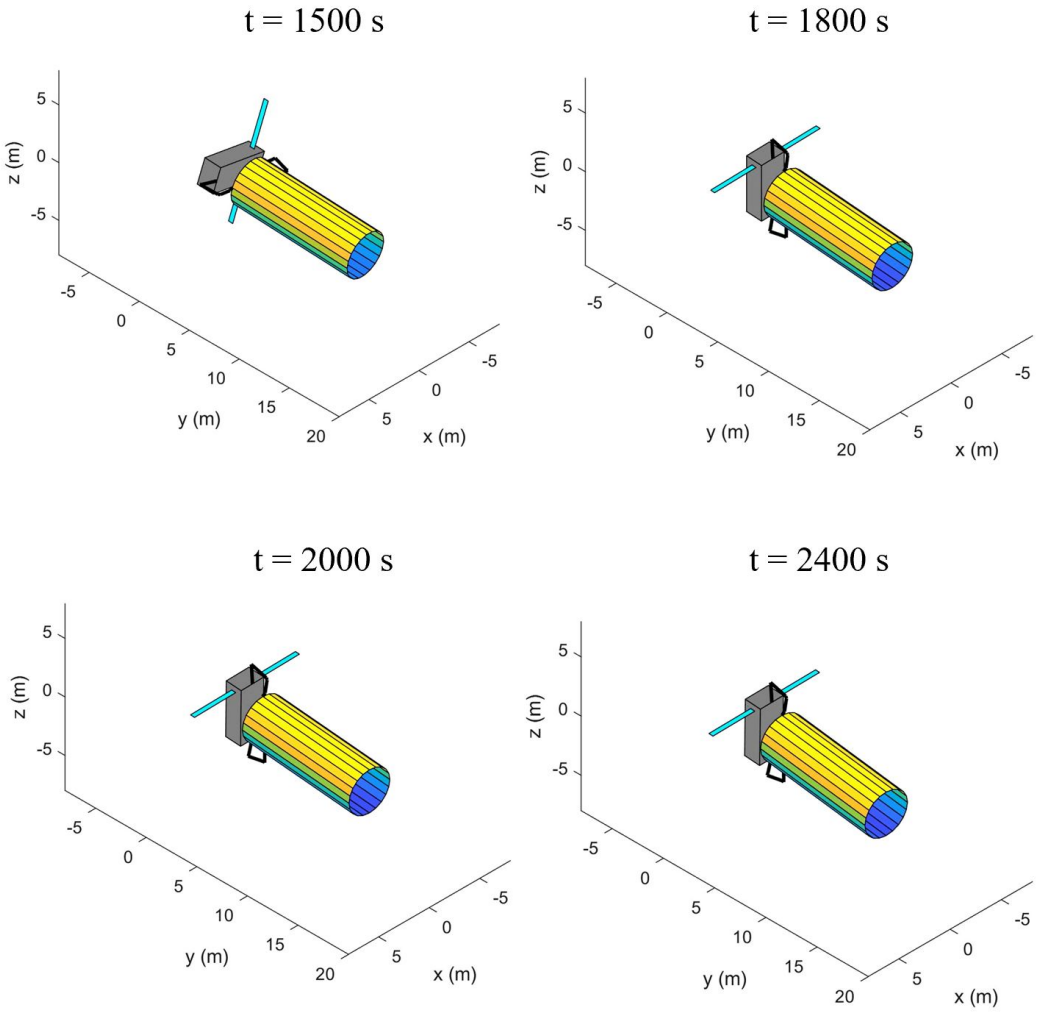

Figure 4.40. Evolution of the system when performing the de-spinning maneuver (continuation from Fig. 4.39).

Conclusions

This thesis project has been developed in the framework of multi-body systems dynamics and it has been dedicated to the development of comprehensive simulation platforms for modeling and efficient control of space manipulator systems. The work dealt with the non-linear dynamic analysis of complex robotic systems by exploiting advanced modeling and control tools such as Kane's equations, Neural Networks, optimal and classical control. In order to meet the challenges and complexities associated to the highly non-linear nature of the dynamic phenomena being considered, multi-constraint optimization restrictions and spacecraft operational constraints, advanced software packages and simulation environments as Matlab, Simulink, MSC Adams, MSC Patran-Nastran have been utilized. The attention has been focused on the deployment, pre-grasping and post-grasping operations to be performed by a Space Manipulator on a non-cooperative target object in the framework of future autonomous on-orbit missions which are presently being studied by the scientific and industrial community worldwide in order to improve space assets operational capabilities and propose a solution to the issue of orbital debris removal which will gain increasing relevance as more subjects are (and will continue) manifesting their interest in accessing the space environment. Future work will entail the addition of further complex mechanical features to the developed models of manipulator systems and target objects, the synthesis of different control strategies for the mission tasks to be accomplished and the consideration of diversified operational scenarios as well.

Bibliography

[1] T.M. Wasfy, A.K. Noor, *Computational strategies for flexible multibody systems*, Appl. Mech. Rev., Volume 56(6), 2003, Pages 553-613.

[2] H.G. Lemu, *Advances in numerical computation based mechanical system design and simulation*, Adv. Manuf., Volume 3(2), 2015, Pages 130-138.

[3] Q. Tian, L. Cheng, L. Pei et Al., *Advances and challenges in dynamics of flexible multibody systems*, Journal of Dynamics and Control, Volume 15(5), 2017, Pages 385-405.

[4] Q. Wang, F.F. Zhuang, Y.Y. Guo et Al., *Advances in the research on numerical methods for non-smooth dynamics of multibody systems*, Adv., Mech. 43(1), 2013, Pages 101-111.

[5] J.J. Laflin, K.S. Anderson, I.M. Khan et Al, *Advances in the application of the divide-and-conquer algorithm to multibody system dynamics*, J. Comput. Nonlinear Dyn., Volume 9(4), 2014.

[6] W. Schiehlen, *Computational dynamics: theory and applications of multibody systems*, Eur. J. Mech. A. Solids, Volume 25, 2006, Pages 566-594.

[7] W. Schiehlen, *Multibody system dynamics: roots and perspectives*, Multibody Sys. Dyn., Volume 1(2), 1997, Pages 149-188.

[8] A.A. Shabana, *Flexible multibody dynamics: review of past and recent developments*, Multibody Syst. Dyn., Volume 1(2), 1997, Pages 189-222.

[9] P. Eberhard, W. Schiehlen, *Computational dynamics of multibody systems: history, formalisms and applications*, J. Comput. Nonlinear Dyn., Volume 1(1), 2006, Pages 3-12.

[10] O.A. Bauchau, A. Laulusa, *Review of contemporary approaches for constraint enforcement in multibody systems*, J. Comput. Nonlinear Dyn., Volume 3(1), 2008.

[11] A. Laulusa, O.A. Bauchau, *Review of classical approaches for constraint enforcement in multibody systems*, J. Comput. Nonlinear Dyn., Volume 3(1), 2008.

[12] P. Masarati, *Adding kinematic constraints to purely differential dynamics*, Comput. Mech., Volume 47(2), 2011, Pages 187-203.

[13] P. Masarati, *Constraint stabilization of mechanical systems in ordinary differential equations form*, Proc. IMechE Part K: Multi- body Dyn., Volume 225(1), 2011, Pages 12-31.

[14] M. Arnold, B. Burgermeister, C. Führer et Al., *Numerical methods in vehicle system dynamics: state of the art and current developments*, Veh. Syst. Dyn., Volume 49(7), 2011, Pages 1159-1207.

[15] A. Flores-Abad, O. Ma, K. Pham, S. Ulrich, *A review of space robotics technologies for on-orbit servicing*, Progress Aerosp. Sci., Volume 68, 2014, Pages 1-26.

[16] C. Bonnal, J.M. Ruault, M.C. Desjean, *Active debris removal: Recent progress and current trends*, Acta Astronautica, Volume 85, Apr.-May 2013, Pages 51-60.

[17] M.M. Castronuovo, *Active space debris removal - a preliminary mission analysis and design*, Acta Astronautica, Volume 69(9-10), 2011, Pages 848-859.

[18] E.M. Botta, I. Sharf, A.K. Misra, *Simulation of tether-nets for capture of space debris and small asteroids*, Acta Astronautica, Volume 155, 2019, Pages 448-461.

[19] Y.N. Razoumny, S.A. Kupreev, A.K. Misra, *Method of tethered system control for deorbiting objects using Earth's atmosphere*, 3rd IAA Conference on Dynamics and Control of Space Systems, June 2017, Moscow, Russia.

[20] R. Kumar, R. Hayes, *System requirements and design features of Space Station Remote Manipulator System Mechanism*, Proceedings of the JPL 25th Aerospace Mechanism Symposium, 1991, Pages 15-30.

[21] R. Boumans, C. Heemskerk, *The European Robotic Arm for the International Space Station*, Robot. Autom. Syst., Volume 23, 1998, Pages 17-27.

[22] L. Patten, E. Lindsay, O. Layi, O. Marius, K. Nara, L. Aris, T. Ed, *International Space Station Robotics: A comparative study of ERA, JEMRMS and RMSS*, Proceedings of ASTRA 2002, Noordwijk, 2002.

[23] P. Gasbarri, A. Pisculli, *Dynamic/control interactions between flexible orbiting space-robot during grasping, docking and post-docking maneuvers*, Acta Astronautica, Volume 110, May-June 2015, Pages 225-238.

[24] P. Gasbarri, M. Sabatini, G.B. Palmerini, *Ground tests for vision based determination and control of formation flying spacecraft trajectories*, Acta Astronautica, Volume 102, 2014, Pages 378-391.

[25] R. Opromolla, G. Fasano, G. Rufino, M. Grassi, *Spaceborn LIDAR-based system for pose determination of uncooperative targets*, Proceedings of 2014 IEEE Metrology Aerospace (MetroAeroSpace), 2014, Pages 265-270.

[26] F. Aghili, K. Parsa, *Adaptive motion estimation of a tumbling satellite using laser-vision data with unknown noise characteristics*, Proceedings of IROS 2007 IEEE/RSJ International Conference on Intelligent Robots and Systems, 2007, Pages. 839-846.

[27] D. Akin, N. Limparis, K. McBryan, *Enabling Dexterous Manipulation and Servicing by SmallSats*, Proceedings of the 25th Annual USU/AIAA Small Satellite Conference, Logan, 2012.

[28] D. Reintsema, B. Sommer, T. Wolf, J. Thaeter, A. Radthke, W. Naummann, P. Rank, J. Sommer, *DEOS - The In-flight Technology Demonstration of Germany's Robotics Approach to Dispose Malfunctioned Satellites*, Proceedings of the 11th Symposium on Advanced Space Technologies in Robotics and Automation - ASTRA 2011, Noordwijk, 2011.

[29] M. Chalon, A. Wedler, A. Baumann, W. Bertleff, A. Beyer, J. Butterfass, M. Grebenstein, R. Gruber, F. Hacker, E. Kraemer, K. Landzettel, M. Maier, H.J. Sedlmayr, N. Seitz, F. Wappler, B. Willberg, T. Wimboeck, G. Hirzinger, F. Didot, *Dexhand: a Space qualified multi-fingered robotic hand*, Proceedings of IEEE International Conference on Robotics and Automation, Shanghai, 2011.

[30] M. Luo, W. Lu, B. Sun, T. Mei, *Autonomous Grasping of a Space Robot Multisensory Gripper*, Proceedings of 2006 IEEE/RSJ International Conference on Intelligent Robots and Systems, 2006, Pages 1014-1019.

[31] A. Pisculli, L. Felicetti, P. Gasbarri, G.B. Palmerini, M. Sabatini, *Deployment analysis and control strategies of flexible space manipulators*, Proceedings of the International Astronautical Congress (IAC) 2013, Beijing, Volume 7, 2013, Pages 572-577.

[32] C. Toglia, M. Sabatini, P. Gasbarri, G.B. Palmerini, *Optimal target grasping of a flexible space manipulator for a class of objectives*, Acta Astronautica, Volume 68(7-8), 2011, Pages 1031-1041.

[33] Y. Jia, A.K. Misra, *Robust trajectory tracking control of a dual-arm space robot actuated by control moment gyroscopes*, Acta Astronautica, Volume 137, 2017, Pages 287-301.

[34] X. Cyril, S. Kim, M. Ingham, A.K. Misra, G. Jaar, *Post-impact dynamics of to multi-body systems attempting docking/berthing*, Acta Astronautica, Volume 40(11), 1997, Pages 759-769.

[35] P. Santini, P. Gasbarri, *Dynamics of multibody systems in space environment; Lagrangian vs. Eulerian approach*, Acta Astronautica, Volume 54(1), January 2004, Pages 1-24.

[36] T. Kane, D. Levinson, *The use of Kane's dynamical equations in robotics*, International Journal of Robotics Research, Volume 2(3), 1983, Pages 3-21.

[37] D. King, *Space Servicing: Past, Present and Future*, Proceedings of the 6th International Symposium on Artificial Intelligence and Robotics & Automation in Space, Montréal, Canada, 2001.

[38] G. Chiandussi, M. Codegone, S. Ferrero, F.E. Varesio, *Comparison of multi-objective optimization methodologies for engineering applications*, Computers & Mathematics with Applications, Volume 63, Issue 5, 2012, Pages 912-942.

[39] F. Capitanescu, A. Ahmadi, E. Benetto, A. Marvuglia, L. Tiruta-Barna, *Some efficient approaches for multi-objective constrained optimization of computationally expensive black-box model problems*, Computers & Chemical Engineering, Volume 82, 2015, Pages 228-239.

[40] A. Zhou et Al., *Multiobjective evolutionary algorithms: A survey of the state of the art*, Swarm and Evolutionary Computation, Volume 1, Issue 1, 2011, Pages 32-49.

[41] P. Gasbarri, L.D. Chiwiacowsky, H.F. De Campos, *A hybrid multilevel approach for aeroelastic optimization of composite wing-box*, Structural and Multidisciplinary Optimization, Volume 39, Issue 6, 2009, Pages 607-624.

[42] S. Suresh, P.B. Sujit, A.K. Rao, *Particle swarm optimization approach for multi-objective composite box-beam design*, Composite Structures, Volume 81(4), 2007, Pages 598-605.

[43] N. Srinivas, K. Deb, *Multi-objective function optimization using non-dominated sorting genetic algorithms*, Evolutionary Computation, Volume 2, 1995, Pages 221-248.

[44] K. Price, R. Storn, *Differential Evolution - A simple evolution strategy for fat optimization*, Dr. Dobb's Journal, Volume 22(4), 1997, Pages 18-24 and 78.

[45] B.V. Babu, R. Angira, *A differential evolution approach for global optimization of MINLP problems*, Proceedings of 4th Asia-Pacific Conference on Simulated Evolution and Learning, Singapore, 2002, Pages 880-884.

[46] M. Dorigo, G. Di Caro, *The Ant Colony Optimization Meta-Heuristic*, New Ideas in Optimization, McGraw-Hill, 1999.

[47] J. Kennedy, R. Eberhart, Y. Shi, *Swarm Intelligence*, Morgan Kaufmann Publisher, San Francisco, 2001.

[48] K.E. Parsopoulos, M.N. Vrahatis, *Recent Approaches to Global Optimization Problems Through Particle Swarm Optimization*, Natural Computing, Volume 1, 2002, Pages 235-306.

[49] M. Reyes-Sierra, C.A.C. Coello, *Multi-Objective Particle Swarm Optimizers: A Survey of the State-of-the-Art*, International Journal of Computational Intelligence Research, Volume 2, 2006, Pages 287-308.

[50] L. D Li, X. Yu, X. Li, W. Guo, *A Modified PSO Algorithm for Constrained Multi-Objective Optimization*, 2009 Third International Conference on Network and System Security.

[51] K. Deb, *Multi-Objective Optimization using Evolutionary Algorithms*, John Wiley & Sons, 2001.

[52] F. Marini, B. Walczak, *Particle swarm optimization (PSO). A tutorial*, Chemometrics and Intelligent Laboratory Systems, Volume 149, 2015, Pages 153-165.

[53] S. Hochreiter, Y. Bengio, P. Frasconi, J. Schmidhuber, *Gradient flow in recurrent nets: the difficulty of learning long-term dependencies*, A Field Guide to Dynamical Recurrent Neural Networks, 2003.

[54] H. Olsson, K.J. Aström, C. Canudas de Wit, M. Gäfvert, P. Lischinsky, *Friction Models and Friction Compensation*, European Journal of Control, 1998.

[55] S. Hochreiter, J. Schmidhuber, *Long short-term memory*, Neural computation, Volume 9(8), 1997, Pages 1735-1780.

[56] A. Rosato, M. Panella, R. Araneo, A. Andreotti, *A Neural Network-based Prediction System of Distributed Generation for the Management of Microgrids*, IEEE Transactions on Industry Applications, 2019.

[57] A. Rosato, R. Altilio, R. Araneo, M. Panella, *Prediction in photovoltaic power by neural networks*, Energies, Volume 10(7), 2017, Pages 1003-1028.

[58] D. Kingma, J. Ba, *Adam: A method for stochastic optimization*, Proceedings of the 3rd International Conference on Learning Representations (ICLR), San Diego, CA, USA, 2015.

[59] H. Nakanishi, K. Yoshida, *Impedance control for free-flying space robots - basic equations and applications*, IEEE/RSJ International Conference on Intelligent Robots and Systems, Beijing, China, 2006, Pages 3137-3142.

[60] P.M. Pathak, A. Mukherjee, A. Dasgupta, *Interaction torque control by impedance control of space robots*, Simulation, Volume 85(7), 2009, Pages 451-459.

[61] N. Uyama, H. Nakanishi, K. Nagaoka, K. Yoshida, *Impedance-based contact control of a free-flying space robot with a compliant wrist for non-cooperative satellite capture*, 2012 IEEE/RSJ International Conference on Intelligent Robots and Systems, Vilamoura, Algarve, Portugal, October 7-12, 2012.

[62] D.N. Nenchev, K. Yoshida, *Impact analysis and post-impact motion control issues of a free-floating space robot subject to a force impulse*, IEEE Transactions on Robotics and Automation, Volume 15(3), June 1999.

[63] O. Ma, A. Flores-Abad, K. Pham, *Control of a space robot for capturing a tumbling object*, International Symposium on Artificial Intelligence, Robotics and Automation in Space, Turin, Italy, 2012.

[64] A. Flores-Abad, Z. Wei, O. Ma, K. Pham, *Optimal control of space robots for capturing a tumbling object with uncertainties*, Journal of Guidance, Control and Dynamics, Volume 37(6), 2014, Pages 2014-2017.

[65] N. Uyama, T. Narumi, *Hybrid Impedance/Position Control of a Free-flying Space Robot for Detumbling a Noncooperative Satellite*, IFAC-PapersOnLine 49-17, 2016, Pages 230-235.

[66] C. Chuanzhi, N. Hong, C. Jinbao, W. Xiaotao, *A velocity-based impedance control system for a low impact docking mechanism (LIDM)*, Sensors, Volume 14, 2014, Pages 22998-23016.

[67] M. Raibert, J. Craig, *Hybrid position force control of manipulators*, ASME Journal of Dynamic Systems, Measurement and Control, Volume 102(2), 1981, Pages 126-133.

[68] S. Arimoto, H. Han, C.C. Cheah, S. Kawamura, *Extension of impedance matching to nonlinear dynamics of robotic tasks*, Syst. Control Lett., Volume 36(2), 1999, Pages 109-119.

[69] K. Yoshida, H. Nakanishi, N. Inab, H. Ueno, M. Oda, *Contact Dynamics and Control Strategy Based on Impedance Matching for Robotic Capture of a Non-cooperative Satellite*, ROMANSY-2004, Montréal, Canada, June 14-18, 2004.

[70] R. Ozawa, H. Kobayashi, *A new impedance control concept for elastic joint robots*, Proceedings of the IEEE International Conference on Robotics and Automation, 2003, Pages 3126-3131.

[71] S.A. Schneider, R.H. Cannon Jr., *Object impedance control for cooperative manipulation: theory and experimental results*, IEEE Transactions on Robotics and Automation, Volume 8(3), 1992, Pages 383-394.

[72] S.A.A. Moosavian, R. Rastegari, E. Papadopoulos, *Multiple impedance control for space free-flying robots*, Journal of Guidance, Control and Dynamics, Volume 28(5), September-October 2005.

[73] A. Stolfi, P. Gasbarri, M. Sabatini, *A combined impedance-PD approach for controlling a dual-arm space manipulator in the capture of a non-cooperative target*, Acta Astronautica, Volume 139, 2017, Pages 243-253.

[74] P.M. Trivailo, L. Wang, *Capture, ejection and handling of space payloads, using robotic systems with super-flexible manipulator arms*, Proceedings of the International Astronautical Congress (IAC), Volume 6, 2013, Pages 4627-4635.

[75] N. Uyama, D. Hirano, H. Nakanishi, K. Nagaoka, K. Yoshida, *Impedance-based contact control of a free-flying space robot with respect to coefficient of restitution*, IEEE/SICE International Symposium on System Integration (SII), Kyoto, 2011, Pages 1196-1201.

[76] L.M. da Fonseca, O. Saotome, M.N. Pontuschka, G.L.B. Lima, H.V. de Figueiredo, N. Seito, *Interaction between motions of robotic manipulator arms and the non-fixed base in on-orbit operations*, Journal of Aerospace Technology and Management, Volume 7(4), 2015, Pages 443-453.

[77] L. Felicetti, P. Gasbarri, A. Pisculli, M. Sabatini, G.B. Palmerini, *Design of robotic manipulators for orbit removal of spent launchers' stages*, Acta Astronautica, Volume 119, February-March 2016, Pages 118-130.

[78] G. Hirzinger, K. Landzettel, D. Reintsema, C. Preusche, A. Albu-Schäffer, B. Rebele, M. Turk, *Rokviss - robotics component verification on ISS*, Proceedings of the 8th International Symposium on Artificial Intelligence, Robotics and Automation in Space (ISAIRAS), 2005, Session 2B.

[79] P. Gasbarri, R. Monti, M. Sabatini, *Very large space structures: Non-linear control and robustness to structural uncertainties*, Acta Astronautica, Volume 93, 2014, Pages 252-265.

[80] J. Baumgarte, *Stabilization of constraints and integrals of motion in dynamical systems*, Computer Methods in Applied Mechanics and Engineering, Volume 1(1), June 1972, Pages 1-16.